Tampere University

XIAOLONG ZHANG

Towards IMU-based Full-body Motion Estimation of Rough Terrain Mobile Manipulators

Tampere University Dissertations 705

Tampere University Dissertations 705

XIAOLONG ZHANG

Towards IMU-based Full-body Motion Estimation of Rough Terrain Mobile Manipulators

ACADEMIC DISSERTATION
To be presented, with the permission of
the Faculty of Science and Engineering
of Tampere University,
for public discussion in the auditorium Pieni sali 1
of the Festia building, Korkeakoulunkatu 8, Tampere,
on 16 December, at 12 o’clock.

ACADEMIC DISSERTATION
Tampere University, Faculty of Engineering and Natural Sciences
Finland

Responsible supervisor and Custos	Professor Jouni Mattila Tampere University Finland	
Pre-examiners	Docent Huapeng Wu LUT University Finland	Professor Mileta M. Tomovic Old Dominion University USA
Opponents	Professor Arto Visala Aalto University Finland	Program Manager Arto Peltomaa DIMECC Oy Finland

The originality of this thesis has been checked using the Turnitin Originality Check service.

Cover design: Roihu Inc.

ISBN 978-952-03-2650-0 (print)
ISBN 978-952-03-2651-7 (pdf)
ISSN 2489-9860 (print)
ISSN 2490-0028 (pdf)
http://urn.fi/URN:ISBN:978-952-03-2651-7

HIILINEUTRAALI PAINOTUOTE
ClimateCalc CC-000025/FI
PunaMusta Printing

Carbon dioxide emissions from printing Tampere University dissertations have been compensated.

PunaMusta Oy – Yliopistopaino
Joensuu 2022

PREFACE

I am grateful to my supervisor, Professor Jouni Mattila, for his supervision, guidance, and encouragement, especially for his generous participation in providing guidance, constructive feedback, kind support, and advice during my PhD.

This work was funded by the Doctoral School of Industry Innovations (DSII) at Tampere University (TAU) and in-part by Forum of Intelligent Machines (FIMA), this funding is greatly appreciated.

Very special thanks to my teammate Mr. Eelis Peltola, for his detailed feedback in writing this thesis and his cooperation in setting up the test environments for the research.

I am grateful to my parents whose constant love and support keep me motivated and confident. My accomplishments and success are because they believed in me.

ABSTRACT

For navigation or pose estimation, strap-down Micro-Electro-Mechanical System (MEMS) Inertial Measurement Units (IMU) are widely used in all types of mobile devices and applications, from mobile phones to cars and heavy-duty Mobile Working Machines (MWM). This thesis is a summary of work focus on the utilization of IMUs for state estimation of MWM. Inertial sensor-based technology offers an alternative to the traditional solution, since it can significantly decrease the system cost and improve its robustness.

For covering the research topic of whole-body estimation with IMUs, five publications focus on the development of novel algorithms, which use sensor fusion or rotary IMU theory to estimate or calculate the states of MWM. The test-platforms are also described in detail.

First, we used low-cost IMUs installed on the surface of a hydraulic arm to estimate the joint state. These robotic arms are installed on a floating base, and the joints of the arms rotate in a two-dimensional (2D) plane. The novel algorithm uses an Extended Kalman Filter (EKF) to fuse the output of the gyroscopes and the accelerometers, with gravity as the reference. Second, a rotary gyroscope is mounted on a grasper of a crane, and the rotary gyroscope theory is implemented to decrease the drift of the angular velocity measurement. Third, low-cost IMUs are attached to the wheels and the bogie test bed, and the realization of IMU-based wheel odometry is investigated. Additionally, the rotary gyroscope provides information about the roll and yaw attitude for the test bed. Finally, we used an industry grade IMU fuse with the output of wheel odometry to estimate the position and attitude of the base for an MWM moving on slippery ground.

One of the main aims of this research study is to estimate the states of an MWM only using IMU sensors. The research achievements indicate this approach is promising. However, the observability of IMU in the yaw direction of the navigation frame is limited so it is difficult to estimate the yaw angle of the rotation plane for the

robotic arm when only using IMUs, to ensure the long-term reliable yaw angle and position of the vehicle base, external information might also be needed. When applying the rotary IMU theory, minimization of the power supply for the rotation device is still a challenge.

This research study demonstrates that IMUs can be low-cost and reliable replacements for traditional sensors in joint angle measurement and in the wheel rotation angle for vehicles, among other applications. An IMU can also provide a robust state for a vehicle base in a challenging environment. These achievements will benefit future developments of MWMs in remote control and autonomous operations.

CONTENTS

List of Figures

List of Tables

ABBREVIATIONS

ADC	Analog to Digital Converter
CF	Complementary Filter
CR	Continuous Rotation
DOF	Degree Of Freedom
DSII	Doctoral School of Industry Innovations
EKF	Extended Kalman Filter
ESKF	Error State Kalman Filter
FIMA	Forum of Intelligent Machines
GFIMU	Gyroscope-Free IMU
GNSS	Globe Navigation Satellite System
HACV	Heavy-Duty Autonomous Construction Vehicle
IMU	Inertial Measurement Unit
INS	Inertial Navigation System
KF	Kalman Filter
LiDAR	Light Detection and Ranging
LR	Limited Rotation
MEKF	Multiplicative Extended Kalman Filter
MEMS	Micro-Electro-Mechanical System
MWM	Mobile Working Machine
NASA	National Aeronautics and Space Administration
OEM	Original Equipment Manufacturer

RMM	Rough Terrain Mobile Manipulator
RMS	Root Mean Square
RTK-GPS	Real Time Kinematic-Global Positioning System
TAU	Tampere University
TCP	Tool Center Point
UWB	Ultra-Wideband
WD	Wheel Drive

ORIGINAL PUBLICATIONS

Publication I	Xiaolong Zhang, Eelis Peltola, and Jouni Mattila. "Joint angle estimation for floating base robots utilizing MEMS IMUs". In: *2017 IEEE International Conference on Cybernetics and Intelligent Systems (CIS) and IEEE Conference on Robotics, Automation and Mechatronics (RAM)*. 2017, pp. 282–287. DOI: 10.1109/ICCIS.2017.8274788.
Publication II	Xiaolong Zhang, Eelis Peltola, and Jouni Mattila. "Angle estimation for robotic arms on floating base using low-cost IMUs". In: *2018 IEEE International Conference on Robotics and Automation (ICRA)*. 2018, pp. 1458–1465. DOI: 10.1109/ICRA.2018.8462898.
Publication III	Xiaolong Zhang, Teemu Mononen, Jouni Mattila, and Mohammad M Aref. "Mobile robotic spatial odometry by low-cost imus". In: *2018 14th IEEE/ASME International Conference on Mechatronic and Embedded Systems and Applications (MESA)*. 2018, pp. 1–6. DOI: 10.1109/MESA.2018.8449209.
Publication IV	Xiaolong Zhang, Pauli Mustalahti, Eelis Peltola, and Jouni Mattila. "3D Attitude Calculation for the Grasper of a Crane System with a Rotary Gyroscope". In: *2018 Ninth International Conference on Intelligent Control and Information Processing (ICICIP)*. 2018, pp. 229–235. DOI: 10.1109/ICICIP.2018.8606668.
Publication V	Xiaolong Zhang, Henri Liikanen, Eelis Peltola, Mohammad M. Aref, and Jouni Mattila. "Localization of a Heavy-Duty Omnidirectional Vehicle Using IMU and Wheel Odometry". In: *15th European Workshop on Advanced Control and Diagnosis (ACD*

2019). Ed. by Elena Zattoni, Silvio Simani, and Giuseppe Conte. Cham: Springer International Publishing, 2022, pp. 1155–1172. ISBN: 978-3-030-85318-1. DOI: https://doi.org/10.1007/978-3-030-85318-1_67.

Author's contribution

This section clarifies the author's contribution to the manuscript.

Publication I — The author wrote the manuscript and developed the approach for joint angle estimation for floating base robots utilizing Micro-Electro-Mechanical System (MEMS) Inertial Measurement Unit (IMUs). Eelis Peltola helped with the test system by building the test environment, wrote the part about the test hardware, and reviewed the manuscript. Professor Jouni Mattila, the academic supervisor, suggested the research direction and reviewed the manuscript, suggesting major improvements.

Publication II — The author wrote the manuscript and developed the approach for angle estimation for robotic arms on floating bases using low-cost IMUs. Eelis Peltola helped to build the test environment and wrote several paragraphs about the test hardware. Professor Jouni Mattila, the academic supervisor, reviewed the manuscript and suggested the research direction and major revisions.

Publication III — The author wrote the manuscript and developed the odometry of mobile robots approach using low-cost IMUs. Teemu Mononen helped with the test environment and reviewed the manuscript; Mohammad Mohammadi Aref reviewed the manuscript and wrote one paragraph of the introduction section. Professor Jouni Mattila, the academic supervisor, reviewed the manuscript and suggested the research direction and major revisions.

Publication IV — The author wrote the manuscript and developed the approach for 3D attitude calculation for the grasper of a crane system with a rotary gyroscope. Pauli Mustalahti helped build the test environment and reviewed the manuscript; Eelis Peltola reviewed the manuscript; Professor Jouni Mattila, the academic supervisor, reviewed the manuscript and suggested the research direction and major revisions.

Publication V — The author wrote the manuscript and developed the approach for localization of a heavy-duty omnidirectional vehicle using IMU and wheel odometry. Henri Liikanen and Eelis Peltola helped build the test environment and analyzed the test data; Mohammad Mohammadi Aref reviewed the manuscript; Professor Jouni Mattila, the academic supervisor, reviewed the manuscript and suggested the research direction and major revisions.

1 INTRODUCTION

Original Equipment Manufacturers (OEMs) of heavy-duty Mobile Working Machines (MWMs), such as those used in construction, forestry, and mining, as well as material handling machines, are part of a huge global industry. In the working machine industry, global construction equipment dominates the market with an estimated revenue of USD 129.6 billion in 2020, which is expected it increase to USD 162.4 billion by 2027, with Asia dominating the market [7].

Currently, these machines are mostly limited to open-loop individually controlled actuators, and skilled operators are needed to achieve the required production rate. Due to current needs to increase productivity, lower operating costs, and improve safety, in the future, these machines will become autonomous field-robotic systems. In robotics terms, these mobile robot platforms with on-board robotic manipulators are commonly called mobile manipulators. These MWMs operate outdoors in off-road conditions; thus, we call them Rough Terrain Mobile Manipulators (RMMs). In conventional factory automation applications, robots used are often bolted on the floor, so they have a stationary base. In contrast, robotic manipulators that are mounted on rough terrain wheel-platforms are described as robots on a floating base. A floating base means the manipulator is mounted on a mobile platform that can experience the full six Degrees of Freedom (DOF) motion. Therefore, the development of autonomous RMMs operating in harsh conditions requires new advanced sensory systems and methods ensuring their whole-body motion estimation and control. In addition to the common requirement of high precision motion estimation, many Finland-based RMM OEMs have relatively low annual production volumes with many machine configuration variants. Therefore, an easy to install and low-cost sensory system for harsh off-road conditions is an essential requirement. Micro-Electro-Mechanical System (MEMS) technology is one potentially lower cost, easy to deploy and smaller sensor system. These MEMS Inertial Measurement Units (IMUs) can replace conventional joint angle sensors. However, IMU-based acceleration measurement utilizing a low pass filter for inclinometer operation often lacks the required static and dynamic accuracy in robotic applications.

Moreover, in remote worksite environments, the Global Navigation Satellite System (GNSS) signal quality-of-service can be low, and deployment of external radio references is difficult to implement. The using of IMU sensor systems can improve the robustness of RMM operations.

The most well-known RMMs are the Mars rovers used by the National Aeronautics and Space Administration (NASA), called Curiosity and Perseverance [42, 41], that have an on-board robotic arm and six wheels connected in two rocker-bogie arrangements, as seen in the image of Perseverance shown in the left side of Figure 1.1. RMMs are also used in forest harvesting and log loading; in this application, they typically have a total of four-wheel pairs in four separate bogies, as shown in the middle and right sections of Figure 1.1.

Figure 1.1 NASA Mars Rover Perseverance (left) [41], Ponsse forest harvester (middle), and Ponsse forest forwarder (right) [46].

Forest RMMs have three main parts: a vehicle wheeled base platform, an on-board hydraulic manipulator, and a manipulator material handing tool, which is a harvesting head or a log grasper. Forest machines are used here as an example of an RMM machine due to their overall complexity and impressive rough terrain maneuverability. However, similar RMMs are available for other applications, such as construction and mining. Nowadays, these RMMs are powered by a diesel engine that drives three or more hydraulic pumps. The first pump is for wheeled platform hydrostatic transmissions and the second one is for the manipulator and its grasper. The third pump can be used for accessory systems, such as brakes and oil cooling fans. Remarkably, the on-board diesel engine is a source of high frequency structural vibrations that also need to be considered in IMU-based RMM whole-body motion estimation and control. Since the wheel odometry is also of interest in the present study, it is worth mentioning that, in forest machines, the hydrostatic transmissions pump is typically connected into a single hydraulic motor that the drives mechanical differential transmission system for the eight-wheel system. It is well known that when one RMM's wheel loses contact with the ground, the dangerous situation of tipping-over may occur. In future autonomous operations, tipping-over should be prevented; thus, an advanced RMM whole-body motion estimation system is needed.

In summary, the forest RMM used as an example research platform, is composed of an on-board multi-DOF robotic manipulator, its manipulator tooling, an articulated RMM platform rear, and front bodies with a total of four bogies and four-wheel pairs that makes it a highly complex system. Therefore, to ensure effective RMM autonomous operations in the future, a high-performance whole-body motion estimation and control system that is low-cost and easy to install must be developed.

1.1 Motivation

For future autonomous operations to be successful, RMMs need to be equipped with a whole-body motion estimation sensory system that would enable the use of navigation and an on-board manipulator in floating base robotic manipulation and object grasping scenarios. In addition to these robotic operations, various safety-related systems are required, such as on-line RMM tipping-over stability monitoring, a prevention system, and wheel anti-slip controllers. As an example, in these RMMs applications, at least one of the wheels can easily lose its contact with the ground causing the wheels to spin or the more dangerous situation of tipping-over. This in turn is vital information for the whole-body motion controller and RMM stability monitoring.

Therefore, this thesis focuses on whole-body motion estimation developments for complex RMMs that would be modular enabling their adaptation into RMMs with different steering configurations ranging from skid-steered vehicles to car-like vehicles. The case study used in this thesis is the articulated steering RMM that is commonly used in forest applications.

1.2 Research Problems (RPs)

As previously mentioned, in general, RMMs have three main subsystems: a vehicle wheeled platform, an on-board robotic manipulator, and a manipulator grasper.

Therefore, the research problem of RMM whole-body motion estimation is approached with these main subsystems in mind, based on the following RPs:

RP1: Can on-board floating base serial link robotic manipulator motions be estimated accurately utilizing multiple low-cost IMUs attached to the surface of the links?

RP2: Can the continuously rotating motion state of RMM wheels that are attached to the bogie suspension arrangements be estimated? Can algorithms be developed to estimate the attitude of RMM wheels on bogies based on low-cost IMU measurements?

RP3: Based on low-cost and continuously rotating IMUs, can the rotation of the RMM wheels be used for low drift estimation of the wheel yaw and roll angles?

RP4: Based on the theory of continuous rotation, can IMUs be used to calculate the attitude of the grasper to ensure anti-sway control?

RP5: Can we estimate the position and attitude for the base of RMM with IMU, by fusing it with the wheel odometry on slippery ground?

1.3 Requirements and Scope of the Research

For a comparison, the industrial robot kinematic structures equipped with embedded high accuracy joint sensors can be rigorously calibrated to provide an accurate robot Tool Center Point (TCP) three degrees-of-freedom (3DOF) position in Cartesian coordinates. Currently, many industrial robot OEMs, such as those manufactured by ABB, provide this as a digital service. For example, the ABB IRB 1400 6DOF robot with 5 kg payload and 1.44 m reach can be purchased with the impressive submillimeter absolute TCP position accuracy of ±0.45 mm [1]. The key enabler for this is highly accurate angle sensors with 20-bit accuracy and bulky robot link structures that can be considered to be ideal rigid bodies.

Consequently, these industrial robots typically have a payload-to-own-weight ratio of less than 0.1. However, the state of the art for a digital service offering for RMMs is very far from this. First, a high payload-to-own-weight ratio close to 1 is needed to ensure high reachability and rough terrain mobility. This results in the structural link flexibilities being an order of one or two higher. Second, due to lower cost considerations, high manufacturing tolerances are used. Third, the annual production volumes of RMMs are relatively low, while the number of product variants is still high, which calls for easy to install and scalable sensory systems.

Therefore, our aim is to revisit this highly complex RMM problem from an interdisciplinary real-world robotics perspective with three novel aspects mentioned above. Toward that end, strap-down low-cost IMUs are set up as a dense sensor network and novel algorithms for motion estimation are developed.

This project was conducted at the Doctoral School of Industry Innovations (DSII) [11] at Tampere University (TAU) and was, in part, funded by the Forum of Intelligent Machines (FIMA) consortium [17]. Many of the FIMA member companies were active in defining a set of requirements for the MWM whole-body motion estimation system. This resulted in the selection of the main requirements for this new sensor system, as follows:

- High measurement accuracy with
  - A static accuracy of ± 0.01 *deg* (16-bit) for each joint angle in generic 6DOF link motion
  - A dynamic accuracy of ± 1 *deg* for each joint angle at rotation velocities below 90 *deg/s*
- Robustness to harsh outdoors operation environment in forestry, material handling, mining, and construction applications at the International Protection Code IP-67 level and an operating temperature range between -40 °C to +125 °C
- Easy-to-install sensor system with a minimal cost-to-precision ratio
- Sensor system that is easy to calibrate and configure in-factory and on-site
- Scalability of the sensor system to the full OEM product range

As previously mentioned, a highly complex forest forwarder that is available at TAU is used as a case study for this thesis. The list of motion DOFs presented in Table 1.1 is used to describe the complexity of this whole-body motion estimation problem and the associated measurements that are required. Special attention is paid to DOFs with a continuous axle rotation that would require a slip-ring type of rotating connector solution for sensor power and measurement signals or battery-driven wireless data transmission.

RMM subsystems have eight wheels connected as pairs into four bogie suspension arrangements, forming eight Continuous Rotation (CR) wheel states and four bogies with Limited Rotation (LR) states. The two RMM body motions are constrained by a 2DOf articulated steering joint with both rear and front bodies capable of 3DOF rotation; thus, there are eight LRs on the base platform. While various sensor installation configurations can be used to recover the full motion state for this particular RMM, the optimization of this sensor system is left for future studies. However, for various special future autonomous RMM base platform functions, such as condition monitoring and tip-over prevention control, the bogies and 2DOF steering joint angles most likely need to be estimated. In this case, the on-board manipulator has three LRs in the vertical plane, commonly called shoulder, elbow, and telescope joints in robotics. A grasper tool connected to the tip of the manipulator has a vertical and horizontal plane passive LR joints followed by a CR joint for tool rotation in the yaw direction. This potentially in-part redundant list of angle measurements that are needed for RMM whole-body motion estimation is given in 1.1.

Table 1.1 Degree of freedom for whole body estimation

Function	Number of axles/sensors	Continuous rotation (CR)/ Limited rotation (LR)
Wheels	8, 1 DOF	CR
Rocker-bogie	4, 1 DOF	LR
Vehicle bodies	6, 2 DOF	LR
Articulated steering joint	2, 2 DOF	LR
On-board manipulator	4, 1 DOF	LR
Grasper tool	3, 1 DOF	1 CR and 2 LR
Total	27, 8 DOF	9 CR and 18 LR

The state of the art work in [61] for state estimation of joint angles on a floating base used industrial-grade IMUs, ADIS16485, for each link, which cost more than 1000 Euros each. Our much cheaper solution uses four IBM160 consumer-grade IMUs for each link, and the cost of one IBMI160 is about 2 Euros. In Table 1.2 presents a summary of several of the key differences between these two types of IMUs. Every industrial-grade ADIS16485 has a factory calibration, so it has A much better performance than the IBM160 consumer-grade IMU, especially its nonlinearity is several times smaller than that of the IBM160.

Table 1.2 IMU comparison

	Grade	Internal ADC resolution	Nonlinearity	Factory calibrated
ADIS16485	Industry	32 bits	gyro 0.01%FS acc 0.1%FS	sensitivity, bias, and axial alignment
BMI160	Consumer	16 bits	gyro 0.1%FS acc 0.5%FS	No

1.4 Methods and Restrictions

In this thesis, the research focus is limited to the use of MEMS strap-down IMUs sensors with gravity as a reference or assistance to estimate the attitude states of the RMM. For the localization of the RMM base platform, we fused the IMUs with the wheel odometry.

The RMM subsystem-based motion estimation methods are designed for two main reasons. First, as previously mentioned, the RMMs are manufactured with various configuration architectures; thus, modularity in whole-body motion estimation is highly desirable. Second, from a practical perspective, due to the relevance and availability of the used complexity RMM research platform, the cost of a full-scale sensor network with 27 IMU nodes is beyond the scope of this thesis.

In general, the state estimation of joint angles for robotic arms is a broad field. For fixed-based manipulators, traditionally a forward kinematic model with data flow from previous links has been used for state estimation [62, 61], or a highly accurate IMU has been used as a reference [49]. The forward kinematic model will propagate an imperfect estimation for the state from previous links or base to the end of the links; it also increases the complexity of the algorithm. This is why, in publications of P-I and P-II, the forward kinematic model is removed.

We attached four low-cost IMUs onto the surface of each link in suitable positions. Using filters, we fused the outputs from the IMUs' accelerometers and gyroscopes and we estimated the 1DOF joint angle between each link with the aid of a gravity reference. Based on the Gyro-Free Inertial Measurement Unit (GFIMU) theory, the specific force of the joint center, the quadratic form of the angular velocity, and the angular acceleration can be expressed in the body-fixed frames only using the information from accelerometers. Using the Extended Kalman Filter (EKF), we fused these outputs from GFIMU with the outputs from the gyroscopes to correct the biases and installation errors of the accelerometers.

Without external information, the yaw angle in the navigation frame is unobservable for the strap-down IMUs used to estimate orientation, and the yaw angle's integration error cannot be eliminated. Additionally, it is difficult to build a dynamic model for the attitude of the grasper of the RMM in our scenario. We applied rotary IMU theory in two cases for the angle calculation. A rotary gyroscope box is attached to the grasper of a crane and the attitude of the grasper is calculated based on the output from the gyroscope, which rotates with a constant speed with respect to the body-fixed frame of the grasper. To provide yaw and roll angle information for the RMM's base, a gyroscope is installed in the center of one of the RMM's wheels.

1.5 Thesis Contributions

The main contribution of this thesis can be summarized as follows:

- P-I An algorithm for joint angle estimation of a floating-base platform with low-cost IMUs is developed. The validation is carried out on a hydraulic crane with three links and two 1DOF joints. The algorithm utilizes the GFIMU theory to calculate the specific force of the joint center, the angular acceleration, and the quadratic form of the angular rate for each link using four triad-axis accelerometers. With an extended EKF, using gravity as a reference, the result is fused with the gyroscope measurements to correct for the biases and installation errors of the accelerometers. The final step of the algorithm employs a complementary filter for fusing the outputs of each accelerometer and gyroscope pair to obtain the joint angles. IMU boxes are designed and built, each of them consisting of one low-cost IMU, a microcontroller, and communication components. The lift joint is moved arbitrarily during validation of the algorithm to simulate a floating base, and the 1DOF tilt joint's angle is the estimated angle; a quadrature encoder's measurement is used as a ground-truth reference.
- P-II The algorithm in P-I is validated on a forest MWM. The vehicle has a 6DOF

wheeled platform acting as a floating base for a crane. Its diesel engine was running during the test procedure. During the test, the vehicle moved on a rough slope made of rubble, and the engine introduces disturbance in the form of oscillation. Since the performance of the estimation results are very sensitive to the positions of the IMUs on the links, in this paper we use an empirical criterion to choose the position of the IMUs that are attached on the links. By introducing simulated bias and drift into the raw data of the IMUs' output, this paper investigates how the configuration of multiple IMUs on one link can improve the estimation performance and the system's robustness.

P-III The paper demonstrates the use of MEMS low-cost IMUs to obtain odometry information for a mobile RMM. An estimation method for the pitch angle of an RMM bogie was also provided. A test bed was built that simulates the RMM's wheel and bogie.

P-IV By applying rotary gyroscope theory to a tactical-grade gyroscope, which is attached to a grasper, the long-term drift of the gyroscope is decreased. The attitude calculation of the grasper became more accurate.

P-V Using ESKF to fuse the output of the IMU measurements and wheel odometry, it is possible to estimate the position and altitude of a MWM moving on a slippery surface. The strategy of tuning the ESKF parameters was also investigated.

1.6 Outline of the Thesis

This thesis is comprised of five chapters. The first chapter introduces the research background, the motivation of the research, the research problems, and the contributions of the articles in this thesis. The following chapters are structured as follows: Chapter 2 introduces the state of the art, focusing on a literature review, comparing the work presented in previous studies, and analyzing the limitations and advantages of each solution. Chapter 3 describes the proposed solutions of our works and presents the results. Chapter 4 presents the research conclusions, discusses the design decisions of the algorithms used, and discusses the possible research direction for further development. Chapter 5 summarizes the main points of the five publications. The five relevant publications follow the last chapter.

2 STATE OF THE ART

This chapter briefly summarizes the state of the art in the field of the thesis. The topics covered are the joint angle estimation, theory of continuously rotating IMU, RMM position and orientation estimation, and sensor fusion, with a focus on the implementation of IMUs for these tasks on MWMs.

2.1 Joint Angle Estimation on a Floating Base

Traditionally, a state estimation for robotic manipulators is done with the manipulator on a stationary base, which means the base has no movement during the operation. Normally, the system utilizes a forward kinematic model with data flow propagation from the base to the last link [30, 62].

In [63], the kinematics model is used to decouple the angle estimation from the state of the RMM's floating base, with each link employing an industry-grade IMU. Since the IMU cannot be installed exactly at the joint rotation center, the angular acceleration is derived from the time derivative of angular velocity to establish the acceleration of the IMU with respect to the joint center. However, the algorithm does not include an estimation of accelerometer bias, and this assumption clearly limits the use of this approach to high-quality IMUs that have low accelerometer bias and low gyroscope noise.

The IMU-based state estimation of a humanoid robot is developed in [67], where an expensive and accurate fiber-optic IMU is used as a reference point for other lower-cost MEMS gyros. The work in [49] uses analog potentiometers, which are traditional joint position sensors, to design a joint acceleration estimation system. The sensor network we endeavored to develop should be low-cost and easy to install. It is difficult to install or fix a traditional angle measurement sensor inside the joint rotational center for machines designed for rough terrain environments, and since the consideration of cost, the use of high-end IMUs are not within the scope of this thesis.

The IMU-based estimation of human gait is studied in [8, 51]. Since the coordinates of IMUs and human body segments cannot be coincident, and the surface of the human body is not rigid, usually the angle measurement accuracy of is only within several degrees. The assumption used is that gravity is the dominant force while moving, but this assumption is not suitable for our scenario as the links of the manipulator on a MWM may have a high rotation speed, resulting in moving accelerations for the IMUs that cannot be ignored.

2.2 Rotary Inertial Navigation System (INS)

A rotating IMU with constant angular rate can eliminate the effect of constant bias on the navigation solution [12]. The drift of a gyroscope's measurement converted into the navigation frame can be written as:

$$\begin{aligned} C_b^n \partial\varepsilon^b &= \begin{bmatrix} 1 & 0 & 0 \\ 0 & \cos\omega t & -\sin\omega t \\ 0 & \sin\omega t & \cos\omega t \end{bmatrix} \begin{bmatrix} \varepsilon_x \\ \varepsilon_y \\ \varepsilon_z \end{bmatrix} \\ &= \begin{bmatrix} \varepsilon_x \\ \varepsilon_y \cos\omega t - \varepsilon_z \sin\omega t \\ \varepsilon_y \sin\omega t + \varepsilon_z \cos\omega t \end{bmatrix} \end{aligned} \tag{2.1}$$

where ω is the IMU rotation rate; $\partial\varepsilon^b = \left[\varepsilon_x \ \varepsilon_y \ \varepsilon_z\right]^T$ are the constant biases of the gyroscope in three axis, and C_b^n is the conversion matrix from the body frame to the navigation frame. If the gyroscope rotates around the x-axis with a constant rate, integrating the equation 2.1, gives another equation 2.2,

$$\int_T C_b^n \partial\varepsilon^b = \begin{bmatrix} \int_T \varepsilon_x \\ \int_T \left(\varepsilon_y \cos\omega t - \varepsilon_z \sin\omega t\right) \\ \int_T \left(\varepsilon_y \sin\omega t + \varepsilon_z \cos\omega t\right) \end{bmatrix} \approx \begin{bmatrix} \int_T \varepsilon_x \\ 0 \\ 0 \end{bmatrix} \tag{2.2}$$

where T is the IMU rotation period. Equation 2.2 shows that the angle errors in the non-rotating axis will be eliminated after the integration of one rotation period, since the constant errors of a rotary sensor are modulated into sine waves in the navigation frame. This property of rotating IMUs is applied in Publication III and Publication IV.

2.2.1 IMU-Based Wheel Odometry

In [6, 43], a MEMS IMU is installed in the center of an RMM wheel to form a rotary IMU. The navigation performance improved significantly, especially with respect to the position drift on the horizontal plane and in the estimation of the RMM heading angle.

Du et al. propose rotating IMUs to improve the INS observability [13]. Weak system observability would lead to inaccurate estimation, eventually degrading the performance of the navigation solution. In [14], the methods for mitigating sensor errors utilizing rotating IMU are investigated.

2.2.2 Anti-Sway of Grasper on a Crane System

Anti-sway control of the grasper for a crane system is essential for its safe operation. The lack of information of the position and sway angle of the grasper induces risks in operation, which could lead to collisions and decrease the crane's operation efficiency. In [29, 40], crane anti-sway controllers were developed to limit swaying of their graspers. The proposed solution in [29] used an inclinometer and kinematic model to estimate the sway angle. Whereas in [40], the sway angle was directly measured with high-accuracy incremental encoders and a full kinematic model was applied to recover other states of the grasper.

The works in [15, 25, 26, 47] applied a strap-down IMU to measure the load orientation, and a dynamic model converted the measurement into position and trajectory information of the load.

Several papers [22, 23, 24] investigated the vision-based sway angle estimation. In [23], the crane rope's sway angle was estimated in two directions using a smart camera tracking a marker. In [24], a vision sensor was used to measure the marker positions; the sensor was attached to a hook to estimate the swing angle. This technique was based on a template matching method. Paper [22] focused on implementation with an infrared vision sensor in a low-light application condition that was insufficient for normal cameras.

For some scenarios, the dynamic or kinematic model for filter design is difficult to build, and [48] proposed a strategy without using state-space models; however, their lift wire length and the position of their base were known, which makes the estimation easier.

2.3 Localization of a Vehicle Based on IMU

Positioning and attitude information is essential for autonomous RMMs [32]. As the MEMS technology has developed, the MEMS strap-down IMU has become low-cost and more reliable, and their weight and power consumption has continually decrease [27], making MEMS IMUs popular choices for navigation solutions

Although inertial navigation is self-contained, the sensor error, the drift of the gyroscopes, and the bias of the accelerometers will lead to accumulating navigation errors [44, 57]. INSs need an external sensor or other information to correct the IMUs' bias and the errors in the navigation solution's estimation. The extra information for aiding IMU navigation could be from an external radio source, such as GNSS [28, 50, 65]. In an indoor environment, the external information could be from an Ultra-Wideband (UWB)radio [2, 16, 64].

Adding vision-based aiding to RMM navigation with IMU was proposed in [5, 56]. Huang presents a contemporary literature review for fusing vision with an IMU in [21], and the equations of a kinematic model of an IMU were described there in detail.

In poor lighting conditions, LiDARs may be applied as the aiding sensors [37, 68, 69]. In comparison to LiDARs and vision sensors, radar has performance advantages in different weather and light conditions [31, 34].

Strap-down IMU fusing with wheel odometry has been investigated intensively for decades, such as in [9, 66]. Wei et al. in [45] used adaptive models to fuse a tactical-grade IMU with wheel odometry; the average accuracy of the position was smaller than 20 m for field tests, which lasted about 7 hours with a total traveled distance of about 490 km.

In [4], Matin et al. applied recurrent deep neural networks to detect motion states for a wheeled RMM, such as a stationary position, zero velocity in the lateral direction, etc. The corresponding pseudo-measurements are formed according to different motion dynamics and they are fed to the observation models of an EKF.

Using only a moderate-cost IMU whose gyroscopes' stability is 10 deg/h as a sensor, the estimates of the final position fall within 20 m of a reference of ground truth at the end of the 73-minute test sequence. Only employing a solo IMU, [3] used a deep neural network to dynamically adapt the noise parameters of the filter and achieve, on average, a 1.10% translational error.

The key points of the work in [3, 4, 45] are similar on some level, as they used different observation models or adaptive noise parameters for filters to deal with several kinds of movement of a wheeled RMMs. For example, when the RMM remains stationary, the biases of its IMU and the attitude of the RMM in the roll and pitch axes can be easily estimated with a reference from gravity. When the RMM moves on a roughly flat road, the non-holonomic constraint [10, 66, 53] is applied to form extra measurements for filtering. This constraint simply assumes that the velocity in the vertical or lateral direction in the body-fixed frame is close to 0 with some Gaussian noise. Traditionally, it is difficult for a filter with only an IMU to recognize different moving patterns, such as keeping an RMM stationary or moving one with constant speed. That means that applying an adaptive noise parameter for filter or switching to a different model to match the motion pattern will not always be done at the right moment. Additionally, when introducing other sensors than IMUs, for example wheel odometry, if wheel slip or side slip cannot be recognized, it will apply the wrong observations to the filter, which fuses the velocity information with the IMU. This will deteriorate the estimation results.

The work in [3, 4] is based on a moderate-cost IMU, and the results can compete with the tests that use a high-cost IMU aided by LiDARs or vision cameras. This implies that, nowadays, a moderate-cost IMU is accurate enough for long-term localization for a wheeled RMM without additional sensors. IMUs could be the core element of localization systems, with other sensors only needed to update the states that have weak or no observability for an IMU, such as position and yaw angle. Alternatively, other sensors could be used to determine the RMM's motion pattern, such as being stationary or moving in a straight line, and the IMU-based filter could then switch to a different model or tune its parameters accordingly.

Low-cost strap-down IMUs are normally aided by GPS or cameras. In [20, 55], the observability for a GPS-based INS was investigated extensively. The work in [55] is based on a non-linear model from a global view, which means that the estimation is done for the entire time span. In [20], a general linear time-varying model is used to investigate the observability properties. The results were similar; translational motions, i.e., acceleration changes, can enhance the observability of the attitude and sensor bias, and angular motions can enhance the observability of the lever arm. Here, the lever arm is the coordinate of the GPS antenna in a body-fixed frame. In [19, 39], the authors investigated the observability for a vision-aided INS system.

2.4 Sensor Fusion

To estimate the system states, several filtering methods have been introduced. In several studies, such as [30, 38, 60, 62], a complementary filter (CF) was designed to fuse the gyroscope and accelerometer measurements. CF is relatively simple, computationally light, and it has the capability to utilize the advantages of both IMU sensor elements. It is well known that the angular estimation using a gyroscope has better accuracy at high frequencies, while the accelerometer has better performance at low frequencies [38].

In Publication I and Publication II, we used a CF to fuse the outputs from GFIMU and the gyroscopes. The angle information from the GFIMU is relatively noisy; however, it has less bias than the gyroscope. In contrast, the angle integrated from the gyroscope measurement has less noise, but the angular speed measurement normally has an offset with respect to the true value. A CF can take advantage of the strengths of each sensor to smooth the estimation and decrease the bias of the sensor.

The Multiplicative Extended Kalman Filter (MEKF) appeared in an estimator of attitude that used a gyroscope and a star tracker in the late 1960s at NASA [58]. In [33, 36], MEKF was introduced and discussed in detail. After more than 50 years of evolution, the full theory behind MEKF was developed and validated in the most challenging conditions. To this day, it is still considered to be one of the most attractive filters for IMU-based attitude estimation. In robotics, this filter is better known as an ESKF [54] or an Indirect Kalman Filter(IEKF) in [59].

The work in Publication V follows the conventions from [54], and the name of the filter is inherited here as ESKF. The ESKF has several advantages, but we are mainly concerned with two implementations aspects as follows. First, the error dynamic is slow, and this allows us to apply Kalman Filter (KF) correction at a lower rate. For example, the RTK-GPS provides either 20 Hz or 50 Hz position observations for updating the error states, but the filter can run at a prediction rate of several hundreds of Hertz. In other applications, vision information, such as from a camera or LiDAR, can provide updates roughly from at 10 Hz to 20 Hz, and the ESKF corrects this rate but can run at a much higher prediction rate.

Second, in [54], the authors pointed out: "the error state is far from possible parameter singularities, gimbal lock issues, providing a guarantee that the linearization validity holds at all times."

For example, a Euler angle-based EKF for estimation of attitude suffers from singularity issues when the pitch angle is close to ± 90 *deg* [18]. In Publication III, we assumed that the rotation or oscillation plane is roughly parallel to the gravity; thus, the EKF has no singularity issue; however, the linearization for the EKF does not seem to hold the same accuracy at all intervals, and in some points the estimation error increases significantly.

3 SOLUTIONS AND RESULTS

3.1 Angle Estimation for Robotic Arms on Floating Base

The works in Publications P-I and P-II have aimed to develop and validate an algorithm using low-cost IMUs for the state estimation of robotic arms mounted on a floating base. The proposed algorithm for estimating the link angles used IMUs with a 3-DOF gyroscope and 3-DOF accelerometer that cost less than 2 euros, such as the Bosch BMI160 [52], which was used in the current thesis. We attached four strap-down IMUs on each link's surface to form a single virtual IMU whose body-fixed frame's origin was located at the center of the joint's rotation axis, as shown in Figure 3.1.

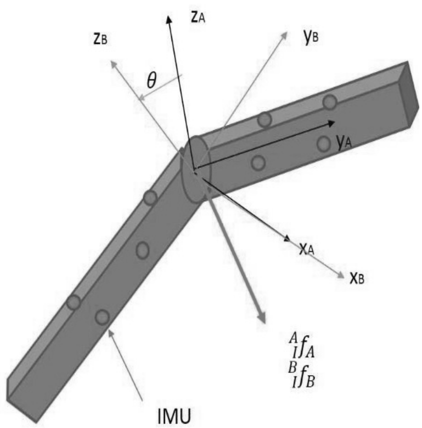

Figure 3.1 IMUs attached on the links' surface to form virtual IMU

Body-fixed frames $\{A\}$ and $\{B\}$ are located at the origin of the center of the two links' joint. The specific force of the joint center is expressed in the two frames.

Our design is based on GFIMU theory, which uses multiple accelerometer outputs for calculating the angular rate and angular acceleration for each link, as well as the specific force of the coordinate origin. An EKF is designed for fusing the output of GFIMU and the measurement of the three-axis gyroscope to estimate the angular rate, the drift of the gyros, and the bias of the accelerometers.

We show that the same specific force added to the joint center can be expressed in these two body-fixed frames $\{A\}$ and $\{B\}$. Through algebraic manipulation of the specific force elements that are the outputs from the two fixed frames, we can determine the relative angle of the two links, as shown in equation 3.1.

$$\theta = \arctan 2\left(f_{Ay}f_{Bz} - f_{Ay}f_{Az}\,,\, f_{By}f_{Ay} + f_{Az}f_{Bz}\right) \tag{3.1}$$

where $\arctan 2\,(\cdot\,,\cdot)$ is the function that returns the four-quadrant inverse tangent function of its two inputs, θ is the joint angle between the two links, f_{Ay}, f_{Az} are the elements of specific force in the y-z plane expressed in frame A, and f_{By}, f_{Bz} are the elements in the B frame.

The angle calculated from equation 3.1 has high noise, and the bias of the gyroscopes cannot always be estimated accurately.Therefore, we designed CF for drift estimation in the gyroscopes and in the joint angle. The scheme of the algorithm is shown in Figure 3.2.

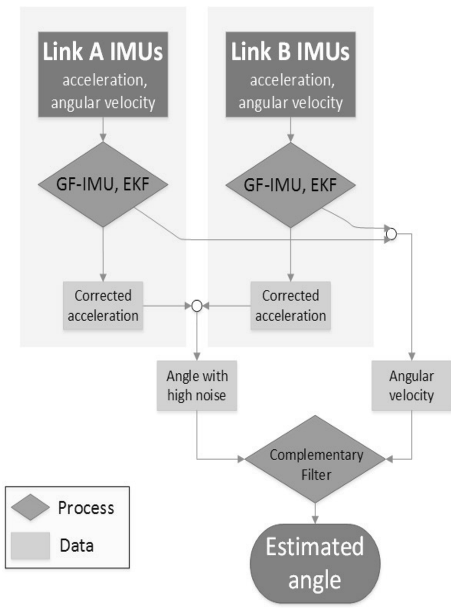

Figure 3.2 Flowchart of processing for the joint angle estimation

In P-I, we initially tested our algorithm using low-cost IMUs on a vertical plane hydraulic arm, where the first joint was moved to generate a motion disturbance to the second joint angle we tried to estimate. The test-platform is shown in Figure 3.3. A root mean square (RMS) error of 0.202 *deg*s was observed in the estimated angle. However, the disturbance motion only had one DOF, and no diesel engine–induced vibrations disturbances were present.

In P-II, we validated the proposed algorithm with a real-scale MWM. The angle of the swing joint connecting the robotic arm's vertical plane joints and the machine's base was not estimated. The MWM was a floating-base 6-DOF wheeled test-platform and had a running diesel engine for the full-scale test scenario, as shown in Figure 3.4. The measured results showed that our theory was valid, with the accuracy of the joint angle estimation being better than 1 *deg* in a RMS error.

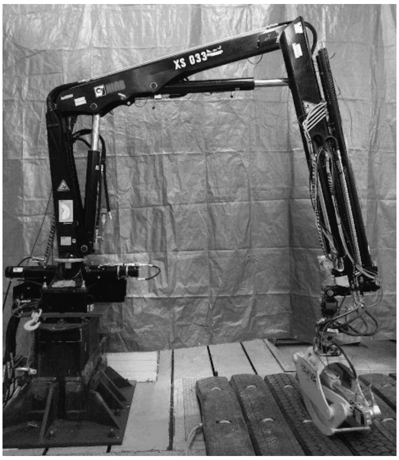

Figure 3.3 Hiab platform

Figure 3.4 Ponsse platform

3.1.1 Gyroscope-Free IMUs

There were two main reasons we why our design was based on GFIMU. First, we needed to measure the specific force in the joint rotation axis center, but in practice, it would be quite hard or nearly impossible to install the IMUs exactly into the joint rotation center. Second, we aimed to use an IMU array to form one virtual IMU for improving the angle estimation performance, whereas a single low-cost IMU can have limited performance.

The performance of the GFIMUs were sensitive to IMU placements on the links. Improper choice of the IMUs' placement on each link will enlarge the noise of the

GFIMU's output. However, in practice, the IMU placements cannot be chosen freely because hydraulic manipulator links have uneven surfaces and hydraulic pipes and hoses that can block the mounting. Therefore, the IMUs' positions in the experiments were not optimal, but still, as the results showed, the GFIMU implementations had acceptable noise ratios.

3.1.2 Results of Joint Angle Estimation Test

Table 3.1 below summarizes the joint angle estimation errors with and without the accelerometer bias correction in P-I. With the CF based bias correction, the accuracy of the estimation improved significantly in our low-cost IMU array experiments with the test platform shown in Figure 3.3. The data presented are statistics from the EKF steady state.

In the second Table 3.2, we summarize the P-II test results with our algorithm on the platform shown in Figure 3.4. The joint angle encoders were available for use as the ground-truth references to verify our algorithm performance. During these tests, all three joints of the platform links were rotated arbitrarily in a plane by a human operator using open-loop control. In addition, for the floating-base robotic arm experiment, the MWM was driven several times from an even ground to a slope made of rubble and then back, as shown inFigure 3.4. This formed a moving 6-DOF base platform experienced by the robotic arm links. Because the MWM diesel engine was running, additional structural high frequency vibrations were transferred to the links. The test results are presented in terms of standard deviation, mean of absolute error, and maximum of absolute errors. Table 3.1 shows that our results with low-cost IMUs on floating base with bias correction were at the same level as the results obtained in [62, 63] with high-end IMUs.

Table 3.1 Test results I

	peak abs. error	mean abs. error	RMS error
With correction of accelerometers bias (deg)	0.887	0.154	0.202
Without correction of accelerometers bias (deg)	3.019	0.624	0.874

Table 3.2 Test results II

	standard deviation	mean abs. error	maximum error
tilt(deg)	0.947	0.612	4.49
lift(deg)	0.638	0.480	1.952

3.2 Mobile Robotic Spatial Odometry by Low-Cost IMUs

Figure 3.5 shows the test bed used for developing low-cost, IMU-based spatial absolute odometry for wheels attached on MWM's oscillating bogies. The test bed simulated the movement of a RMM bogie and wheel rotation with two actuated motors. One strap-down IMU was installed on the bogie with a range of motion of about ± 20 *deg*, and the second one had a continuously rotating wheel close to its rotation axis. We used gravity as a reference, and an EKF was designed to fuse the output of the gyroscopes and accelerometers to provide the oscillation angle of the bogie and the absolute rotation angle of the wheel. Additionally, one IMU was installed on the rotation center of the wheel to provide the information of the roll and yaw angles of the RMM with the theory of rotary IMU.

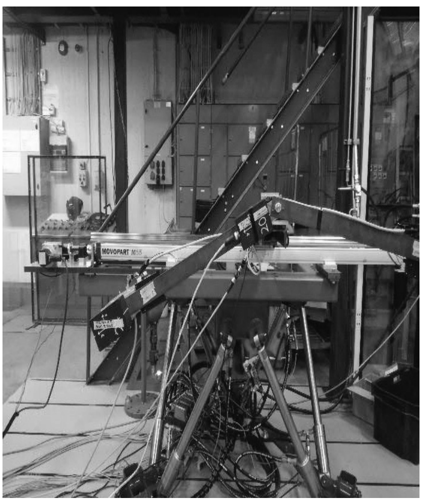

Figure 3.5 Test bed for bogie and wheel odometry with IMUs

3.2.1 Angle Estimation of Bogie and Wheel Rotation with EKF

The EKF has been designed with three states as its input: the rotation angle θ, angular velocity $\dot{\theta}$, and bias of gyroscope in its rotation direction b_g, as in equation 3.2.

$$x[k] = \begin{bmatrix} \theta[k] \\ \dot{\theta}[k] \\ b_g[k] \end{bmatrix} \tag{3.2}$$

The process model is $x[k+1] = Ax[k] + w[k]$, where the state transition matrix is

$$A = \begin{bmatrix} 1 & T & 0 \\ 0 & 1 & 0 \\ 0 & 0 & 1 \end{bmatrix} \tag{3.3}$$

, $w[k]$ is the process noise, and T is the sampling interval.

The two accelerometers measurements in the rotation plane and measurement of a gyroscope along the rotation direction were used as observations. The observation model is as follows:

$$h = \begin{bmatrix} 9.81cos\theta + a_z \\ -9.81sin\theta + a_x \\ \dot{\theta} + b_g \end{bmatrix} + \begin{bmatrix} n_z \\ n_x \\ n_\theta \end{bmatrix} \tag{3.4}$$

where n_z, n_x, and n_θ are Gaussian noise of the above sensors. The constant of 9.81 is the gravity reference. a_z and a_x are the motion acceleration in the two directions, and we regard these two items as noise when linearizing the model in equation 3.4.

With one BMI160 IMU mounted on the bogie's surface, the joint was rotated by an electric motor to simulate the bogie's pitch angle in a test lasting about 12minutes. The amplitude of the bogie's oscillation was about 8 *deg* and its period 20 seconds. The RMS error for the estimation of the bogie pitch angle of the bogie was 0.673 *deg*.

Another BMI160 IMU was mounted on wheel axle, and the wheel was rotated by an electric motor for motion simulation, where the rotation speed switched between 100 *deg/s* and 170 *deg/s* every 20 seconds. With the bogie motion mentioned above, the resulting wheel rotation angle estimation RMS error was 1.886 *deg*.

3.2.2 Calculation of the Yaw and Roll Angles of the Bogie

Applying the rotary IMU theory presented in Chapter 2.2, the yaw and roll angles of the test bed were set to zero. Because the bogie's oscillation introduced some extra angular velocity, the assumption that the rotation speed would be constant could not hold. We designed a gyroscope's error model given in equation 3.5.

$$\begin{bmatrix} \delta\omega_x \\ \delta\omega_y \\ \delta\omega_z \end{bmatrix} = \begin{bmatrix} k_{xy} + d_x \\ S_y\omega + d_y \\ k_{zy} + d_z \end{bmatrix} \tag{3.5}$$

where $[\delta\omega_x, \delta\omega_y, \delta\omega_z]^T$ is the gyroscope sensor's error, k_{xy} and k_{zy} are the factors of the installation error for the rotation axis projected into the x-axis and y-axis. The derivatives d_x, d_y, and d_z are the gyroscope's bias. After the correction of gyroscope with the model of equation 3.5, we applied the rotary IMU theory with equations 2.1 and 2.2 to integrate the yaw and roll angles.

In an 11-minute test where the wheel rotation speed was 170 deg/s and the bogie oscillated with an angular speed below 12 deg/s, the results showed that the yaw angle drift was less than 5 deg, and the roll angle drift was within ± 1 deg, as shown in Figure 3.6.

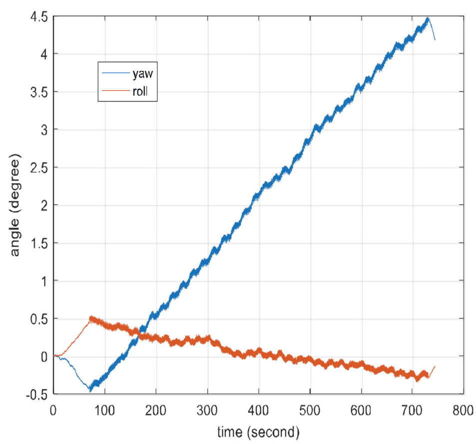

Figure 3.6 The drift in the integration of yaw and roll angle.

3.3 Attitude Calculation for the Grasper of a Crane

In this work, we have investigated an approach for the attitude calculation of a grasper attached to a crane. The grasper had a 3-DOF joint structure connected to a Hiab033 crane, as shown in Figure 3.7. The two passive joints (Joint 1 and Joint 2) in the series were connected to the grasper's continuous rotating (CR) motor joint (Joint3); this model is illustrated in Figure 3.8. Our design was based on rotary IMU theory. We used an industry-grade IMUs gyroscope rotated by a motor with a constant speed with respect to the body-fixed frame of the grasper.

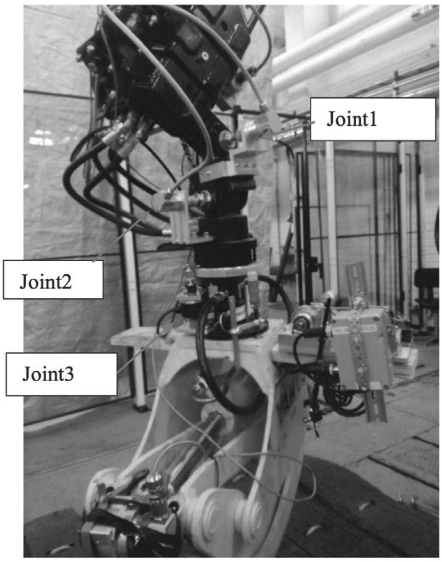

Figure 3.7 Hiab platform's grasper

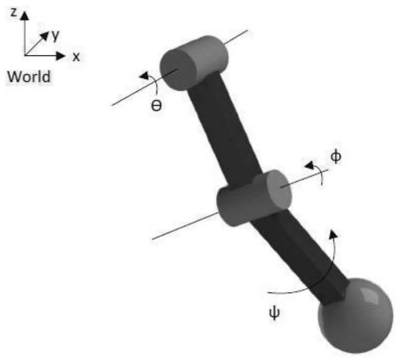

Figure 3.8 3D model of the grasper

We set the IMU to rotate at a speed of 250 deg/s. By subtracting this constant value from the output of the gyroscope, we obtained the rotation speed of the grasper in the pitch direction, here as expressed in the body-fixed frame. Utilizing a Euler angle matrix, we transformed the angular speed in the other axes from being expressed in the rotation frame to being expressed in the body-fixed frame.

During the test, at first, we kept both the grasper and rotary IMU stationary for about 30 seconds, and then, we compared the mean value of its gyroscopes' outputs with zero for obtaining the bias of the gyros. Then, keeping the grasper stationary, we rotated the IMU for about 30 seconds. After this, by utilizing the error model of rotary IMUs described in equation 3.5, we obtained the installation error factors

k_{xy}, k_{zy} and the scale factor S_y.

The attitude integration in quaternion form is as follows:

$$q_{k+1} = q_k + \dot{q}_k \triangle t \tag{3.6}$$

where $\triangle t$ is the sample time. Then, the time derivative of quaternion is the following:

$$\dot{q}_k = \frac{1}{2} q_k \otimes \begin{bmatrix} 0 \\ \omega_k \end{bmatrix} = \frac{1}{2} \Omega(\omega_k) q_k \tag{3.7}$$

and $\Omega(\omega_k)$ has the form

$$\Omega(\omega_k) = \begin{bmatrix} 0 & -\omega_x & -\omega_y & -\omega_z \\ \omega_x & 0 & \omega_z & -\omega_y \\ \omega_y & -\omega_z & 0 & \omega_x \\ \omega_z & \omega_y & -\omega_x & 0 \end{bmatrix} \tag{3.8}$$

The quaternion form of attitude represented as q_k was transferred into Euler angle form and then was compared with the output of the encoder installed on each joint. In our 3-minute test, the Hiab033 crane's grasper was operator driven. This test results showed that the maximum oscillation amplitudes were about 50 *deg* in the pitch and yaw direction and about 8 *deg* in roll direction. In this test, the estimation RMS error was 0.831 *deg* in the pitch angle. After about 100 seconds of angle integration, the RMS error in the yaw direction was 1.43 *deg*, and the maximum error in roll was less than 2 *deg*.

3.4 Localization of a Heavy-Duty Omnidirectional Vehicle Using IMU and Wheel Odometry

In the current research, we developed positioning algorithms using sensor fusion of an industry-grade MEMS IMU and wheel odometry on a 4-Wheel Drive (WD) heavy RMM. A Real Time Kinematic-Global Positioning System (RTK-GPS) was used to provide a ground-truth reference for the estimated RMM position and yaw angle.

3.4.1 RTK-GPS for Ground-Truth Reference

Two GPS antennas were located 2.6 *m* apart on the chassis of our Heavy-Duty Autonomous Construction Vehicle (HACV). One antenna received the position, and the other one was used to form the heading vector for the HACV yaw angle in combination with the first antenna. A RTK-GPS base station was used for giving reference point for correction. With this correction, the accuracy for the horizontal position was ± 0.02 *m*, and the accuracy for the yaw angle was ±0.09 *deg*, which served as the ground-truth measurement. This GNSS receiver had a data rate of 50 *Hz*. We propagated the states from filter to the time of the RTK-GPS output.

3.4.2 Observation of ESKF

Two observation models have been designed for ESKF development. In the first case, while the RMM was kept stationary, the equation 3.9 was used as the observation model for system initialization phase. The three velocity elements in the navigation frame were set to zero, and the yaw angle, which was also set to zero during the initialization phase, was chosen as the fourth element. The four-element vector formed the observations after subtracting the corresponding filter-estimated states. Because the navigation frame would rotate as the earth rotates, we directly modified the yaw angle observation accordingly, adding an offset in the yaw axis for the bias of gyro.

$$z_{k+1} = \begin{bmatrix} 0 \\ 0 \\ 0 \\ \psi_{fix} - \omega_{earth} sin(La) t_{k+1} \end{bmatrix} - \begin{bmatrix} \hat{v}_x \\ \hat{v}_y \\ \hat{v}_z \\ \hat{\psi} \end{bmatrix} \tag{3.9}$$

where ψ_{fix} is the fixed value for the yaw angle; ω_{earth} is the earth's rotation speed; and *La* is the latitude of test location. The RMM was kept stationary for about 10 to 20 seconds. The IMU's biases and roll and pitch angle were then estimated.

After the initialization phase, while in the moving phase, the model is described in equation 3.10,

$$z_{k+1} = fC_o^I \begin{bmatrix} v_{bx} \\ v_{by} \\ 0 \end{bmatrix} - V_b \tag{3.10}$$

where v_{bx} and v_{by} are the velocities from wheel odometry in the body-fixed frame. f indicates the efficiency of the wheel odometer, and V_b is the estimated velocity transferred into the body-fixed frame. C_o^I is the matrix denoting the misalignment between the wheel odometer and the body-fixed frame. In the tests, we kept itas an identical matrix because estimating it online would need a relatively long movement distance for the RMM. However, we compensated for this in the yaw axis of the gyroscope in dynamic equations, where the angular velocity could be modified to be the following:

$$\omega = \begin{bmatrix} \omega_{mx} & \omega_{my} & (1-k)\omega_{mz} \end{bmatrix}^T - \omega_b \tag{3.11}$$

where k is a factor and $(1-k)\omega_{mz}$ indicates the gyroscope's measurement in yaw axis projected onto the body-fixed frame. Of course, because of the installation errors, the yaw axis of gyroscope output also projected a tiny error into the roll and pitch directions in the body-fixed frame, but the accumulated angle errors were easy to correct or limit with a gravity-aiding design.

3.4.3 Results of Vehicle Localization Test

Two test cases have been included: one trajectory was roughly a triangle shape, and the other was roughly a square shape, here represented as black lines in Figure 3.9 and Figure 3.10. The estimated positions from the KF were transferred to the frame that the wheel odometry used, here represented as a black line. Similarly, the position outputs from RTK-GPS were also transferred to the wheel center and used as a ground truth, here represented as a red line. In the figure, the blue line is the HACV's position trajectory calculated only by using wheel odometry.

The triangle movement was about 255 sseconds, where the initializing stationary phase was from 0 to 15 seconds. For the square shape movement, which took 185 seconds to drive, the initial 18 seconds were stationary.

There was no mechanism in our algorithm to determinate which observation

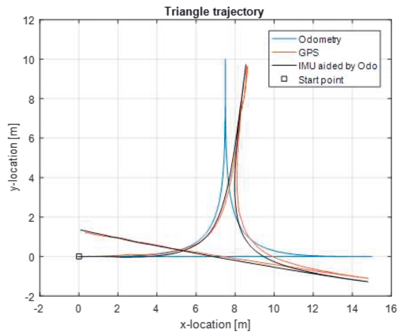

Figure 3.9 Trajectories of the triangle test

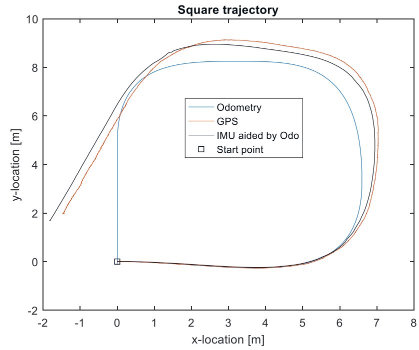

Figure 3.10 Trajectories of the square test

model to use, so we manually set the initial stationary phase as 10 to 15 seconds in the start and used the observation model for moving cases for the remainder of the test. Using the moving observation model for a stationary RMM may lead to the estimation of the vehicle's yaw angle and position to slow drift away from their correct values slowly. The results are summarized in Table 3.3.

Table 3.3 Test results of vehicle localization

Trajectory	Position RMS error (m)	Heading RMS error (degree)	Maximum Position Error (m)	maximum Heading Error (degree)
Triangle	0.199	0.55	0.310	2.27
Square	0.314	0.56	0.490	2.28

4 CONCLUSIONS AND DISCUSSION

This chapter explains the research conclusions, discusses the research's limitations, and gives suggestions for further developments.

P-I and P-II answered RP1; here, the state of a robotic arm on a floating base can be estimated by low-cost IMUs; P-III gave promising results for RP2 and RP3, showing that the oscillation of bogies and wheel rotation can be estimated by IMU with gravity as a reference; the P-IV showed that the rotary IMU can provide attitude information for the grasper of a crane; and RP5 was answered by P-V, inwhich we showed that with the fusion of IMU and wheel odometry, the RMM's position and orientation on slippery ground can be captured.

4.1 State Estimation of Robotic Arm on Floating Base (RP1)

Can on-board floating base serial link robotic manipulator motions be estimated accurately utilizing multiple low-cost IMUs attached on the surface of the links?

For estimation of the joint angle, we needed the specific force of the joint origin expressed in two different frames. The distance between the sensors could lead the outputs of the accelerometers to be different, such as when the links' rotation introduced acceleration to the measurements. Through arithmetic operation of the accelerations and fusing with the output from gyroscopes in the rotation axis, the joint angle was estimated. However, installing the accelerometers exactly into the origin of each joint was difficult in practice. We applied GFIMU theory to obtain the specific force on the joint origin for each link, here with multiple IMUs placed around the origin. The angular acceleration of the link was also produced with the accelerometer network of the GFIMU. Both the angular speed and angular acceleration of the joint were useful information for controlling the robotic arm.

Traditional algorithms use a forward kinematic model that propagates the states from previous links forward, so any imperfections in the states of the base or previous joint will be propagated into the current joint. Our novel development removed this kind of forward kinematic model. The algorithm for angle estimation of a joint only used the measurements of IMUs on the two links forming the joint, allowing us to decouple the pose estimation of a robotic arm from the motion of its platform base and, hence, resulting in the floating base estimation.

Using practice data where the simulated bias was added to one 3-DOF accelerometer on one link, we found the difference of the estimated specific force on the joint origin to be about 25% of the added disturbances compared with the estimation without this added bias. This may imply that the sensor network of IMUs can improve the robustness of the system compared with a single IMU.

However, assembling a sensor network with a large number of IMUs may increase the complexity of the system's hardware. Additionally, low-cost IMUs use a smaller amount of bits for sampling the measurement, leading to the noises of the outputs being more significant compared with a high-quality IMU. The noises of the outputs from a GFIMU network were sensitive to the position of its IMUs on the link's body-fixed frames. For more flexibility in choosing the positions of the IMUs on the links, high-quality IMUs with low noise should be used.

For our implementation, the rotation plane of the joints may not be parallel to the ground because we used gravity as a reference.

Once the position and pose of the base, angle of each joint, and the yaw angle of the links' rotation plane have been acquired, the position of the robotic arm's tip can be calculated through Denavit–Hartenberg parameters [35]. The estimation of the angle of the swing joint with respect to the base was not successful, however, because the gravity assistance was invalidated in this case.

With the quick pace of MEMS technology development, there are now moderate-cost IMU options that internally use more bits in their analog-to- digital converters (ADCs) than the low-cost IMU used in the current thesis, hence increasing the sensitivity of the sensors' measurements. Future implementations have the option to choose better-performing MEMS IMUs while retaining a lower cost.

P-I partially answered RP1: during the tests, one joint that simulated the floating base only rotated within a vertical plane. In P-II, the test platform was a full floating base that had a moving capability of 6 DOF; the results in this publication answered RP1; however, there were some new RPs that arose, such as if we only use one IMU attached to each link, can we estimate the state of motion for a robotic manipulator of serial links on a floating base, here with an external radio source like GNSS information to correct the IMU bias? Can we only use one IMU for each link and arbitrarily choose the position of it on each link and still get similar results?

4.2 Mobile Robotic Spatial Odometry (RP2 and RP3)

Can the RMM wheel's continuously rotating motion state attached on bogie suspension arrangements be estimated? What is the challenge in developing algorithms for attitude estimation of the RMM's wheels on bogies based on low-cost IMU measurements?

Based on low-cost and continuously rotating IMUs, can the rotation of an RMM wheel be used for a low drift estimation of the wheel yaw and roll angles?

We used low-cost IMUs to build an odometer for the RMM, here for control or localization.Although bogie oscillation introduced extra angular speed to the wheel, which slightly violated the assumption that the rotation speed would be constant, we used rotary IMU theory to integrate the yaw and roll angle for the base and achieve errors within ±5 *deg* and ±2 *deg*, respectively, for each angle for an 11-minute-long test. The misalignment of IMU installation on the wheel rotation axis can introduce a sensing error. As shown in equation 3.5, an algorithm using k_{xy} and k_{zy} will multiply the rotation speed to generate the gyroscope's error caused by the installation error in the other two axis. Regarding the rotation axis, the scale factor S_y compensated for the nonlinearity error.

We used an EKF to estimate the oscillation angle of the bogie and rotation angle of wheel, here using gravity as a reference. The accuracy of angle estimation was within ±2 *deg*. However, in practice, the acceleration of vehicle moving will add to the gravity reference, and the filter cannot easily separate the gravitational acceleration from the sensed total acceleration. An adaptive EKF may be suitable for this implementation.

The IMU unit used a battery as its power supply, and the data were transferred wirelessly. A longer lasting power supply and miniaturization of the IMU unit are possible research directions.

In P-III, the tests results gave positive answers regarding RP2. For this problem, we still used traditional EKF and manipulated the covariance matrix in a Cartesian coordinates. However, the rotational angle was in a rotational space, so we should try other filters to improve the estimation accuracy, such as ESKF, for future development.

Regarding rotary IMU theory, P-III also showed that a constant rotating IMU can provide the yaw angle information for RMM, hence answering RP3.

4.3 Attitude Calculation for a Grasper (RP4)

Based on IMU, can we use the theory of continuously rotation IMUs to calculate the attitude of the grasper for its antisway control purposes?

In this work, we validated the theory that a rotary gyroscope can decrease the drift of the angle integration in all axes, except the axis of the gyroscope's rotation. Using the quaternion form in attitude integration can significantly decrease the computational load. The industry-grade gyroscope allowed us to choose a simple initial correction procedure: just keep the gyroscope stationary for about 30 seconds, compare the average outputs with zero, and get the bias of the gyroscope. The rotation motor increased the noise from the gyroscope significantly because the motor itself oscillated and the rotation axis was not aligned perfectly with the gyroscope's axis. If the rotation speed was set as a constant value, the installation error introduced an offset error when converting the sensed rotation speed into the body-fixed frame. For our implementation, the offset error in the rotation axis was the key factor for decreased performance.

The encoders installed inside the joints provided the ground truth for attitude output with respect to the body-fixed frame of the Hiab033 robotic arm. However, because the whole robotic arm was not rigid completely, some errors were introduced during the tests.

The test results in P-IV answered RP4, indicating that an IMU with constant rotation speed can provide the attitude information over a relatively long period without another reference.

4.4 Localization of a Heavy-Duty Omnidirectional Vehicle (RP5)

Can we estimate the position and attitude for the base of RMM with IMU, by fusing it with the wheel odometry on slippery ground?

Because RMMs work in harsh environments, wheel slippage will make positioning estimation that is only dependent on wheel odometry unreliable. Additionally, high accuracy sensors for wheel odometry need complex manufacturing and dedicated calibration, further limiting their implementation in a scenario without other sensors. External radio sources such as GNSS signals can suffer from occlusion, for example, not being available reliably when an RMM moves in a forest.

The yaw angle was unobservable when fusing gyroscopes and accelerometers with a filter using gravity as a reference. Hence, the accumulated error of the integration in the yaw direction could not be corrected. However, the accuracy of the yaw angle value was important for the position estimation of HACVs. The installation error of IMUs regarding the body-fixed frame of the RMM significantly affected the algorithms' performance. We only used a scale factor k to correct the installation error in the yaw direction. The error of the roll and pitch angle could be easily corrected with the gravity reference.

In the plane perpendicular to the ground, we applied a nonholonomic constraint, giving the velocity in body-fixed frame a zero value with some Gaussian noise and treating it as an observation. The constraint improved the estimation's accuracy.

Our test platform was an omnidirectional RMM, and the wheel odometer provided two directions of velocity, v_x and v_y, as expressed in the RMM's body-fixed frame. Therefore, the nonholonomic constraint could not be applied to the side direction for our tests. However, the constraint the in side direction may correct the tiny error in yaw angle integration for a typical car-like RMM with Ackermann steering. Additionally, because slippage of the wheels occurred during the tests, the velocity observed in v_x and v_y cannot provide the true velocity of the RMM at all times. We applied two strategies in the algorithm designed to address this. First, we set the observation noise from the wheel odometers to be relatively high, meaning we depended more on the IMU output. For our case, recognizing when slipping happens was difficult. Second, we included the effect of the earth's rotation into the bias in the yaw direction of the gyroscope: because the navigation frame rotated in inertial frame, we could not ignore this for our 5-minute test.

We set two models for the observation model of our ESKF: a stationary model and motion model. It was essential for estimation results that the filter could switch to the proper observation model for each case, such as when the RMM was stationary, moving with acceleration, moving with constant velocity, or moving while slipping sideways, for example. However, the outputs of the inertial sensors have noise and biases, and algorithms cannot choose the proper motion model for observation when only an IMU-based method is used, as in our case. Future development may include other sensors to assist IMUs in determining the motion model of the RMM.

KF manipulates the noise covariance matrix of the attitude in a Cartesian space. However, the real physical process for attitude happens in a rotation space. By applying an ESKF to choose the error states, the error states are only tiny deviations from the origin of zeros, and the effect of this conflict between the rotation space and Cartesian space is insignificant. However, the filters that deal with the noises of attitude in rotation space need further investigation.

P-V answered RP5, showing that fusing the IMU and wheel odometry can provide promising position and attitude information for an RMM.

5 SUMMARY OF PUBLICATIONS

This thesis summarizes five research publications, each of which is briefly listed below. The research field of Publication I (P-I) and Publication II (P-II) are about the joint state estimation for robotic arms with low-cost IMUs on a floating base. Publication III (P-III) is about using low-cost IMUs to form an odometer for a mobile RMMs. Publication IV (P-IV), focuses on attitude calculation for the grasper of a crane with a rotary gyroscope. The final paper, Publication V (P-V), focuses on localization of MWMs moving on slippery ground at low speed.

5.1 Summary of P-I: Joint Angle Estimation for Floating Base Robots Utilizing MEMS IMUs

In this publication, a novel algorithm of motion estimation for floating base manipulators is presented. Four strap-down MEMS IMUs are mounted on each link to form a virtual IMU whose body-fixed frame is located at the joint's axis of rotation. Using the concept of GFIMUs, the four three degrees-of-field (3DOF) accelerometers of the IMUs on the surface of one rigid link output the specific force of the joint center, the angular acceleration of the link, and the quadratic form of the angular rate of the link. Since it is difficult to use the quadratic form of the angular rate to determinate the sign of the angular rate, we applied an EKF to fuse the output of the GFIMU and the angular rate of the gyroscopes to acquire the angular rates and bias of the gyroscopes, and the bias of all the accelerometers.

In practice, after the EKF, a CF is applied to fuse the angle resulting from acceleration and from integration of the gyroscope. The algorithm is tested with a fixed-base heavy-duty manipulator, HIAB XS033, in a laboratory setting. During the test, only the vertical-plane shoulder and elbow joints are moved. In this test bed, the shoulder joint is used to emulate a floating base movement disturbance, and the elbow link is the test link for the developed angle estimation algorithm.

The results show that our algorithm is very promising. The principal results are that even with low-cost IMUs, which cost less than 5 Euros per chip, and without a forward kinematic model of the manipulator, the angle estimation's maximum error is within ±1.0 *deg*, and the estimation accuracy's RMS error is less than 0.5 *deg*. These initial promising results in the controlled laboratory environment test bed suggest that the developed algorithm should be tested in a real-world mobile manipulator. This test bed only has two planar rotation links and movement in a vertical plane, and it is driven by a hydraulic system.

5.2 Summary of P-II: Angle Estimation for Robotic Arms on Floating Base Using Low-Cost IMUs

This publication is an extension of the work presented in P-I. The algorithm is presented in more detail and it is validated with a commercial MWM, which consists of a 6DOF wheeled base platform and a 3DOF hydraulic anthropomorphic arm. The 2D chart of the links and the IMU boxes attached to it are shown in Figure 5.1. It is installed on a commercial heavy-duty forest forwarder, as shown in Figure 3.4. In this setup, four IMU sensor units are installed on both the hydraulic manipulator shoulder link and the elbow link, while the base of the RMM can move arbitrarily with 6DOF on rough terrain. In addition to this, to truly replicate a floating-base manipulator test scenario, there are structural vibration disturbances from the machine's diesel engine at high frequency and, as these heavy-duty manipulators are heavily loaded, so, some link deformation is unavoidable. Nevertheless, the measured results obtained from the 2DOF planar motion of the floating-base hydraulic arm showed that the accuracy of the angle estimation is less than 1 *deg* in RMS error.

5.3 Summary of P-III: Mobile Robotic Spatial Odometry by Low-Cost IMUs

This publication continues the theme of whole-body motion estimation by considering the estimation of an RMM's wheel angle and velocity states, including the state of the wheels' attachment structure, the bogie. RMM motion states are useful, for example, for wheel slippage control and whole-vehicle load distribution and tip-over stability estimation. The conceptual idea is that a battery-powered IMU with wire-

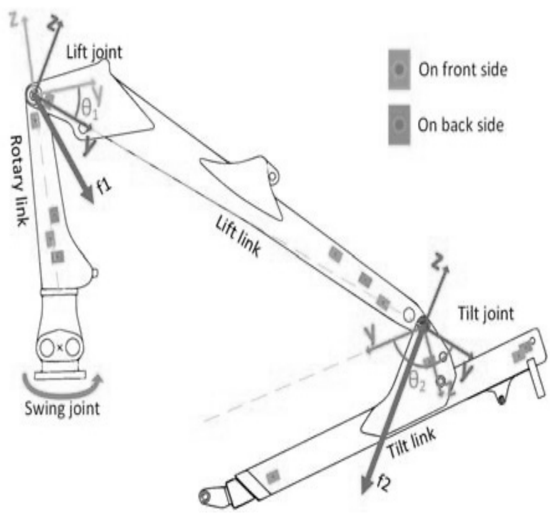

Figure 5.1 Chart of the hydraulic links with attached IMU boxes.

less data transmission is strap-down-installed on the rotation center for each wheel. Moreover, as heavy-duty RMMs often have a suspension arrangement called a bogie, this bogie's motion state should be estimated as well. In this paper, the developed algorithm provides a wheel's rotation angle and the angle of the bogie carrying two wheels. The algorithm also provides the roll and yaw angles of the wheel and bogie over several minutes of continuous wheel rotation.

With gravity as a reference, an EKF is used to fuse the output of the gyroscopes and the accelerometers of the IMU to estimate both the angle of bogie and the rotation angle of the wheel. As the wheel is a natural rotation platform, since a wheel rotates with a roughly constant speed along one axis, the 3DOF gyroscope can form a virtual gyroscope in which the drift on the other two axes can be also decreased. We use this property to calculate the yaw and roll angles of the bogie as well. In this paper, the results are presented based on a simplified bogie-wheel pair test-bed, as shown in Figure 5.2.

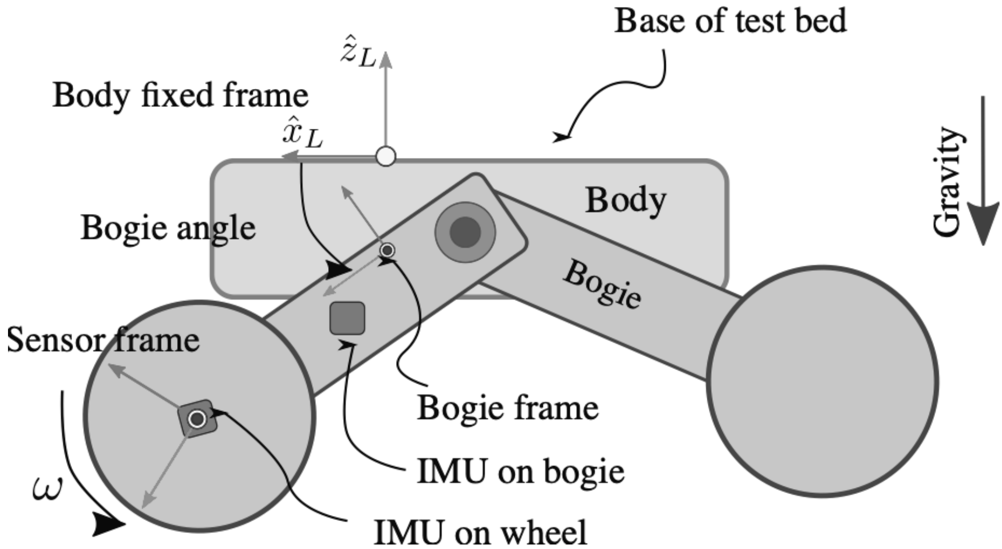

Figure 5.2 Schematics of the test bed containing IMUs strapped on the bogie and the rotating wheel.

5.4 Summary of P-IV: 3D Attitude Calculation for the Grasper of a Crane System with a Rotary Gyroscope

This publication continues the theme started in P-III on rough terrain wheel motion state estimation that is subject to continuous wheel rotation. This problem is shown to call for a battery powered IMU solution; additionally, it is a long-term continuous motion state estimation problem that is subject to gyroscope drift. Moreover, RMMs are often equipped with material graspers that have a continuous grasper rotation joint and two additional passive joints, which increase the dexterity and working envelope of the grasper, in addition to a grasping jaw function. The work in P-IV focuses on the state estimation of such a grasper system, utilizing a 3DOF rotary gyroscope specifically developed for this test and attached to the grasper. We try to decrease the gyroscope's drift in the two axes not perpendicular to the rotation plane. The proposed algorithm is validated on a full-scale heavy-duty manipulator equipped with a commercial log grasper with the above-mentioned DOFs. The test results show that, with a rotary platform, the long-term drift of the gyroscope is decreased and the accuracy of the angle integration for the grasper is increased.

5.5 Summary of P-V: Localization of a Heavy-Duty Omnidirectional Vehicle Using IMU and Wheel Odometry

In this publication, a localization algorithm that uses a vehicle-body-mounted IMU and wheel odometry on a 4 WD MWM for positioning is proposed. While the wheel odometry alone works in ideal cases without wheel slippage, in more realistic scenarios, the velocities measured by the wheel rotation are higher than the actual velocity of the RMM. When the wheels slip to the side, the wheel sensors cannot observe these values. Therefore, it is suitable to fuse IMUs with wheel odometry to generate real-time position feedback. We use an ESKF to fuse the sensor information from an IMU with the wheel odometry, and we show results on a slow-maneuvering RMM in tests up to 5 minutes in length. The IMU is industry-grade MEMS with a gyroscope featuring 6 deg/h bias in-run stability. In the experiments, we used a RTK-GPS as a ground-truth reference for the RMM's heading angle and position. The test results showed that our navigation has an RMS error accuracy of 0.3 m for position and 0.6 deg for the heading angle. Our analysis showed that the non-linearity of the gyroscope in the heading rotation axis is the main limitation for the performance of our implementation.

REFERENCES

[1] ABB. *Absolute Accuracy*. accessed Apr 2022. URL: https://library.e.abb.com/public/0f879113235a0e1dc1257b130056d133/Absolute%20Accuracy%20EN_R4%20US%2002_05.pdf.

[2] Hamza Benzerrouk and AV Nebylov. "Robust IMU/UWB integration for indoor pedestrian navigation". In: *2018 25th Saint Petersburg International Conference on Integrated Navigation Systems (ICINS)*. IEEE. 2018, pp. 1–5.

[3] Martin Brossard, Axel Barrau, and Silvère Bonnabel. "AI-IMU Dead-Reckoning". In: *IEEE Transactions on Intelligent Vehicles* 5.4 (2020), pp. 585–595. DOI: 10.1109/TIV.2020.2980758.

[4] Martin Brossard, Axel Barrau, and Silvere Bonnabel. "RINS-W: Robust inertial navigation system on wheels". In: *2019 IEEE/RSJ International Conference on Intelligent Robots and Systems (IROS)*. IEEE. 2019, pp. 2068–2075.

[5] Tianxing Chu, Ningyan Guo, Staffan Backén, and Dennis Akos. "Monocular camera/IMU/GNSS integration for ground vehicle navigation in challenging GNSS environments". In: *Sensors* 12.3 (2012), pp. 3162–3185.

[6] Jussi Collin. "MEMS IMU carouseling for ground vehicles". In: *IEEE Transactions on Vehicular Technology* 64.6 (2014), pp. 2242–2251.

[7] *Construction Equipment - Global Market Trajectory & Analytics*. Global Industry Analysts, Inc, 2021.

[8] Sébastien Cordillet, Nicolas Bideau, Benoit Bideau, and Guillaume Nicolas. "Estimation of 3D knee joint angles during cycling using inertial sensors: Accuracy of a novel sensor-to-segment calibration procedure based on pedaling motion". In: *Sensors* 19.11 (2019), p. 2474.

[9] G. Dissanayake, S. Sukkarieh, E. Nebot, and H. Durrant-Whyte. "The aiding of a low-cost strapdown inertial measurement unit using vehicle model constraints for land vehicle applications". In: *IEEE Transactions on Robotics and Automation* 17.5 (2001), pp. 731–747. DOI: 10.1109/70.964672.

[10] Gamini Dissanayake, Salah Sukkarieh, Eduardo Nebot, and Hugh Durrant-Whyte. "The aiding of a low-cost strapdown inertial measurement unit using vehicle model constraints for land vehicle applications". In: *IEEE transactions on robotics and automation* 17.5 (2001), pp. 731–747.

[11] DSII. *Doctoral School of Industry Innovation*. accessed Mar 2022. URL: https://www.dsii.fi/.

[12] Shuang Du. "Rotary inertial navigation system with a low-cost MEMS IMU and its integration with GNSS". In: (2015).

[13] Shuang Du, Wei Sun, and Yang Gao. "Improving observability of an inertial system by rotary motions of an IMU". In: *Sensors* 17.4 (2017), p. 698.

[14] Shuang Du, Wei Sun, and Yang Gao. "MEMS IMU error mitigation using rotation modulation technique". In: *Sensors* 16.12 (2016), p. 2017.

[15] Yihai Fang and Yong K Cho. "Crane load positioning and sway monitoring using an inertial measurement unit". In: *Computing in Civil Engineering 2015*. 2015, pp. 700–707.

[16] Daquan Feng, Chunqi Wang, Chunlong He, Yuan Zhuang, and Xiang-Gen Xia. "Kalman-filter-based integration of IMU and UWB for high-accuracy indoor positioning and navigation". In: *IEEE Internet of Things Journal* 7.4 (2020), pp. 3133–3146.

[17] FIMA. *Forum for Intelligent Machines*. accessed Mar 2022. URL: https://www.fima.fi/.

[18] Eric Foxlin. "Inertial head-tracker sensor fusion by a complementary separate-bias Kalman filter". In: *Proceedings of the IEEE 1996 Virtual Reality Annual International Symposium*. IEEE. 1996, pp. 185–194.

[19] Joel. A Hesch, Dimitrios G Kottas, Sean L Bowman, and Stergios I Roumeliotis. "Camera-IMU-based localization: Observability analysis and consistency improvement". In: *The International Journal of Robotics Research* 33.1 (2014), pp. 182–201.

[20] Sinpyo Hong, Man Hyung Lee, Ho-Hwan Chun, Sun-Hong Kwon, and J.L. Speyer. "Observability of error States in GPS/INS integration". In: *IEEE Transactions on Vehicular Technology* 54.2 (2005), pp. 731–743. DOI: 10.1109/TVT.2004.841540.

[21] Guoquan Huang. "Visual-Inertial Navigation: A Concise Review". In: *2019 International Conference on Robotics and Automation (ICRA)*. 2019, pp. 9572–9582. DOI: 10.1109/ICRA.2019.8793604.

[22] Pawel Hyla. "Night vision applicability in anti-sway vision-based solutions". In: *2015 20th International Conference on Methods and Models in Automation and Robotics (MMAR)*. IEEE. 2015, pp. 358–363.

[23] Pawel Hyla. "Single camera-based crane sway angle measurement method". In: *2014 19th International Conference on Methods and Models in Automation and Robotics (MMAR)*. IEEE. 2014, pp. 732–737.

[24] Paweł Hyla and Janusz Szpytko. "Crane payload position measurement vision-based system dedicated for anti-sway solutions". In: *International Conference on Transport Systems Telematics*. Springer. 2014, pp. 404–413.

[25] Jouko Kalmari, Juha Backman, and Arto Visala. "Nonlinear model predictive control of hydraulic forestry crane with automatic sway damping". In: *Computers and Electronics in Agriculture* 109 (2014), pp. 36–45.

[26] Jouko Kalmari, Heikki Hyyti, and Arto Visala. "Sway estimation using inertial measurement units for cranes with a rotating tool". In: *IFAC Proceedings Volumes* 46.10 (2013), pp. 274–279.

[27] S Rao Karumuri, Y Srinivas, J Vijay Sekhar, and K Girija Sravani. "Review on break through MEMS technology". In: *Archiv Phys Res* 2.4 (2011), pp. 158–165.

[28] Zaher Zak M Kassas, Mahdi Maaref, Joshua J Morales, Joe J Khalife, and Kimia Shamei. "Robust vehicular localization and map matching in urban environments through IMU, GNSS, and cellular signals". In: *IEEE Intelligent Transportation Systems Magazine* 12.3 (2020), pp. 36–52.

[29] Yong-Seok Kim, Keum-Shik Hong, and Seung-Ki Sul. "Anti-sway control of container cranes: inclinometer, observer, and state feedback". In: *International Journal of Control, Automation, and Systems* 2.4 (2004), pp. 435–449.

[30] Janne Koivumäki, Janne Honkakorpi, Juho Vihonen, and Jouni Mattila. "Hydraulic manipulator virtual decomposition control with performance analysis using low-cost MEMS sensors". In: *2014 IEEE/ASME International Conference on Advanced Intelligent Mechatronics*. 2014, pp. 910–917.

[31] Andrew Kramer, Carl Stahoviak, Angel Santamaria-Navarro, Ali-akbar Aghamohammadi, and Christoffer Heckman. "Radar-Inertial Ego-Velocity Estimation for Visually Degraded Environments". In: *2020 IEEE International Conference on Robotics and Automation (ICRA)*. 2020, pp. 5739–5746. DOI: 10.1109/ICRA40945.2020.9196666.

[32] Sampo Kuutti, Saber Fallah, Konstantinos Katsaros, Mehrdad Dianati, Francis Mccullough, and Alexandros Mouzakitis. "A survey of the state-of-the-art localization techniques and their potentials for autonomous vehicle applications". In: *IEEE Internet of Things Journal* 5.2 (2018), pp. 829–846.

[33] Ern J Lefferts, F Landis Markley, and Malcolm D Shuster. "Kalman filtering for spacecraft attitude estimation". In: *Journal of Guidance, control, and Dynamics* 5.5 (1982), pp. 417–429.

[34] Yang Li, Yutong Liu, Yanping Wang, Yun Lin, and Wenjie Shen. "The Millimeter-Wave Radar SLAM Assisted by the RCS Feature of the Target and IMU". In: *Sensors* 20.18 (2020). ISSN: 1424-8220. DOI: 10.3390/s20185421. URL: https://www.mdpi.com/1424-8220/20/18/5421.

[35] G.L. Long. *Fundamentals of Robot Mechanics*. Quintus-Hyperion Press, 2015. ISBN: 9780986109416. URL: https://books.google.fi/books?id=4-b9rQEACAAJ.

[36] F Landis Markley. "Attitude error representations for Kalman filtering". In: *Journal of guidance, control, and dynamics* 26.2 (2003), pp. 311–317.

[37] Xiaoli Meng, Heng Wang, and Bingbing Liu. "A robust vehicle localization approach based on GNSS/IMU/DMI/LiDAR sensor fusion for autonomous vehicles". In: *Sensors* 17.9 (2017), p. 2140.

[38] Hyung Gi Min and Eun Tae Jeung. "Complementary filter design for angle estimation using mems accelerometer and gyroscope". In: *Department of Control and Instrumentation, Changwon National University, Changwon, Korea* (2015), pp. 641–773.

[39] Faraz M. Mirzaei and Stergios I. Roumeliotis. "A Kalman Filter-Based Algorithm for IMU-Camera Calibration: Observability Analysis and Performance Evaluation". In: *IEEE Transactions on Robotics* 24.5 (2008), pp. 1143–1156. DOI: 10.1109/TRO.2008.2004486.

[40] Pauli Mustalahti and Jouni Mattila. "Nonlinear full-model-based controller for unactuated joints in vertical plane". In: *2017 IEEE International Conference on Cybernetics and Intelligent Systems (CIS) and IEEE Conference on Robotics, Automation and Mechatronics (RAM)*. IEEE. 2017, pp. 201–206.

[41] NASA. *MARS 2020 Mission Perseverance Rover*. accessed Jul 2020. URL: https://mars.nasa.gov/mars2020/.

[42] NASA. *MARS Exploration Rovers*. accessed Feb 2019. URL: https://mars.nasa.gov/mer/mission/rover-status/#recent.

[43] Xiaoji Niu, Yibin Wu, and Jian Kuang. "Wheel-INS: A Wheel-mounted MEMS IMU-based Dead Reckoning System". In: *IEEE Transactions on Vehicular Technology* 70.10 (2021), pp. 9814–9825.

[44] Aboelmagd Noureldin, Tashfeen B Karamat, and Jacques Georgy. "Fundamentals of inertial navigation, satellite-based positioning and their integration". In: (2013).

[45] Wei Ouyang, Yuanxin Wu, and Hongyue Chen. "INS/Odometer Land Navigation by Accurate Measurement Modeling and Multiple-Model Adaptive Estimation". In: *IEEE Transactions on Aerospace and Electronic Systems* 57.1 (2021), pp. 245–262. DOI: 10.1109/TAES.2020.3011998.

[46] Ponsse. *Ponsse Forest Machines*. accessed Apr 2022. URL: https://www.ponsse.com/en/web/guest/home#/.

[47] Florentin Rauscher, Samuel Nann, and Oliver Sawodny. "Motion control of an overhead crane using a wireless hook mounted IMU". In: *2018 Annual American Control Conference (ACC)*. IEEE. 2018, pp. 5677–5682.

[48] Zhengru Ren, Amrit Shankar Verma, Behfar Ataei, Karl Henning Halse, and Hans Petter Hildre. "Model-free anti-swing control of complex-shaped payload with offshore floating cranes and a large number of lift wires". In: *Ocean Engineering* 228 (2021), p. 108868.

[49] Nicholas Rotella, Sean Mason, Stefan Schaal, and Ludovic Righetti. “Inertial sensor-based humanoid joint state estimation”. In: *2016 IEEE International Conference on Robotics and Automation (ICRA)*. 2016, pp. 1825–1831.

[50] Laith Rasmi Sahawneh, Mohammad Amin Al-Jarrah, Khaled Assaleh, and Mamoun F Abdel-Hafez. “Real-time implementation of GPS aided low-cost strapdown inertial navigation system”. In: *Journal of Intelligent & Robotic Systems* 61.1 (2011), pp. 527–544.

[51] Thomas Seel, Jörg Raisch, and Thomas Schauer. “IMU-based joint angle measurement for gait analysis”. In: *Sensors* 14.4 (2014), pp. 6891–6909.

[52] Bosch Sensortec. *BMI160-Small, low power inertial measurement unit, Data sheet*. Tech. rep. BST-BMI160-DS00001-08 https://www. bosch-sensortec. com/media/boschsensortec ..., 2018.

[53] Eun-Hwan Shin and Naser El-Sheimy. “Accuracy improvement of low cost INS/GPS for land applications”. In: *Proceedings of the 2002 national technical meeting of the institute of navigation*. 2002, pp. 146–157.

[54] Joan Sola. “Quaternion kinematics for the error-state Kalman filter”. In: *arXiv preprint arXiv:1711.02508* (2017).

[55] Yonggang Tang, Yuanxin Wu, Meiping Wu, Wenqi Wu, Xiaoping Hu, and Lincheng Shen. “INS/GPS Integration: Global Observability Analysis”. In: *IEEE Transactions on Vehicular Technology* 58.3 (2009), pp. 1129–1142. DOI: 10.1109/TVT.2008.926213.

[56] Jean-Philippe Tardif, Michael George, Michel Laverne, Alonzo Kelly, and Anthony Stentz. “A new approach to vision-aided inertial navigation”. In: *2010 IEEE/RSJ International Conference on Intelligent Robots and Systems*. IEEE. 2010, pp. 4161–4168.

[57] David Titterton, John L Weston, and John Weston. *Strapdown inertial navigation technology*. Vol. 17. IET, 2004.

[58] NF Toda, JL Heiss, and FH Schlee. “Spars: The system, algorithms, and test results”. In: *Proceedings of the Symposium on Spacecraft Attitude Determination, Aerospace Corp. Rept. TR-0066 (6306)-12*. Vol. 1. 1969, pp. 361–370.

[59] Nikolas Trawny and Stergios I Roumeliotis. "Indirect Kalman filter for 3D attitude estimation". In: *University of Minnesota, Dept. of Comp. Sci. & Eng., Tech. Rep* 2 (2005), p. 2005.

[60] José Fernandes Vasconcelos, Carlos Silvestre, Paulo Oliveira, Pedro Batista, and Bruno Cardeira. "Discrete time-varying attitude complementary filter". In: *2009 American Control Conference*. IEEE. 2009, pp. 4056–4061.

[61] Juho Vihonen, Janne Honkakorpi, Jouni Mattila, and Ari Visa. "Novel pairwise coupled kinematic solution for algebraic angular acceleration estimation of serial link manipulators". In: *2015 IEEE International Conference on Robotics and Automation (ICRA)*. 2015, pp. 809–814.

[62] Juho Vihonen, Janne Honkakorpi, Janne Tuominen, Jouni Mattila, and Ari Visa. "Linear accelerometers and rate gyros for rotary joint angle estimation of heavy-duty mobile manipulators using forward kinematic modeling". In: *IEEE/ASME Transactions on Mechatronics* 21.3 (2016), pp. 1765–1774.

[63] Juho Vihonen, Jouni Mattila, and Ari Visa. "Joint-space kinematic model for gravity-referenced joint angle estimation of heavy-duty manipulators". In: *IEEE Transactions on Instrumentation and Measurement* 66.12 (2017), pp. 3280–3288.

[64] Yan Wang and Xin Li. "The IMU/UWB fusion positioning algorithm based on a particle filter". In: *ISPRS International Journal of Geo-Information* 6.8 (2017), p. 235.

[65] Adam Werries, John Dolan, et al. *Adaptive Kalman filtering methods for low-cost GPS/INS localization for autonomous vehicles*. Tech. rep. Carnegie-Mellon University, 2016.

[66] Yuanxin Wu. "Versatile land navigation using inertial sensors and odometry: Self-calibration, in-motion alignment and positioning". In: *2014 DGON Inertial Sensors and Systems (ISS)*. IEEE. 2014, pp. 1–19.

[67] X Xinjilefu, Siyuan Feng, and Christopher G Atkeson. "A distributed mems gyro network for joint velocity estimation". In: *2016 IEEE International Conference on Robotics and Automation (ICRA)*. IEEE. 2016, pp. 1879–1884.

[68] Haoyang Ye, Yuying Chen, and Ming Liu. “Tightly coupled 3d lidar inertial odometry and mapping”. In: *2019 International Conference on Robotics and Automation (ICRA)*. IEEE. 2019, pp. 3144–3150.

[69] Xingxing Zuo, Patrick Geneva, Woosik Lee, Yong Liu, and Guoquan Huang. “Lic-fusion: Lidar-inertial-camera odometry”. In: *2019 IEEE/RSJ International Conference on Intelligent Robots and Systems (IROS)*. IEEE. 2019, pp. 5848–5854.

PUBLICATIONS

PUBLICATION I

Joint angle estimation for floating base robots utilizing MEMS IMUs

Xiaolong Zhang, Eelis Peltola, and Jouni Mattila

DOI: 10.1109/ICCIS.2017.8274788

Joint angle estimation for floating base robots utilizing MEMS IMUs

Xiaolong Zhang
Automation and Hydraulic Engineering

Tampere University of Technology
Tampere, Finland
xiaolong.zhang@tut.fi

Eelis Peltola
Automation and Hydraulic Engineering

Tampere University of Technology
Tampere, Finland
eelis.peltola@tut.fi

Jouni Mattila
Automation and Hydraulic Engineering

Tampere University of Technology
Tampere, Finland
jouni.mattila@tut.fi

***Abstract*—This paper describes a novel motion estimation algorithm for floating base manipulators that utilizes low-cost inertial measurement units (IMUs) containing a three-axis gyroscope and a three-axis accelerometer. Four strap-down microelectromechanical system (MEMS) IMUs are mounted on each link to form a virtual IMU whose body's fixed frame is located at the center of the joint rotation. An extended Kalman filter (EKF) and a complementary filter are used to develop a virtual IMU by fusing together the output of four IMUs. The novelty of the proposed algorithm is that no forward kinematic model that requires data flow from previous joints is needed. The measured results obtained from the planar motion of a hydraulic arm show that the accuracy of the estimation of the joint angle is within ± 1 degree and that the root mean square error is less than 0.5 degree.**

Keywords: Inertial measurement unit, motion estimation, floating base, extended Kalman filter, hydraulic manipulator

I. INTRODUCTION

Hydraulic manipulators have high payload capabilities and are widely used in rough-terrain mobile work machines, such as forest machines, material transport vehicles, excavators, etc. These machines are ideal for carrying out work in harsh and remote environments as their GPS signals can often be invisible and the base of the manipulators can be nonstationary. Traditionally, joint resolvers or potentiometers are used to measure the manipulator joint angles. However, to reduce system costs and enable adaptation to a variety of environments, the possibility of estimating the motion state of manipulator joints using MEMS-based strap-down IMUs has been investigated [1-3]. In these studies, the robot base was assumed to be stationary, and the estimator was built on a known forward kinematics model of a serial link manipulator, thus requiring IMU information flow from the previous links. In addition, a motion state estimation method for serial link, nonstationary manipulators (so-called floating base manipulators) with MEMS IMUs was developed in [4], with each link employing a tactile grade IMU and costing more than USD 1,000. In that work, the angle estimation was successfully decoupled from the state of the vehicle floating-base. However, this algorithm did not include an estimation of accelerometer bias, and the angular acceleration was derived from time derivative of angular velocity. These assumptions clearly limit the use of the approach to only high-quality IMUs that have low accelerometer bias and low gyroscope noise. Recently, [5] and [6] have developed methods that use IMUs to estimate the motion state for floating-base humanoid joints. In [6], a tactical-grade fiberoptic 6 degree-of-freedom (DOF) IMU (KVH1750) was used as an accurate reference point for a network of low-cost MEMS gyros. Therefore, an accurate base state was required, and a forward kinematic model with data flow from previous links was used. The work in [5] used traditional joint position sensors (potentiometers) in their IMU sensor fusion method for the joint acceleration estimation, which use pairwise IMUs on each consecutive link, but the accelerometer bias was still not included in the estimation.

In this paper, we propose a novel algorithm for the estimation of link angles using MEMS IMUs (BMI160) that cost less than USD 5 each. We use four strap-down IMUs mounted on each link to form a single virtual IMU whose body's fixed frame is located at the center of joint rotation. We show that the same specific force added to the joint center can be expressed in two of these fixed frames. Through algebraic manipulation of the elements of the specific force outputted from the two fixed frames, we can determine the relative angle of the two links. We then apply EKF and a complementary filter (CF) to fuse this angle with the outputs of the gyros and estimate the accelerometer bias and drift of the gyros to decrease the noise of the proposed angle estimation. The initial measured results obtained for the planar motion of a stationary hydraulic arm show that our theory is valid, with the accuracy of the joint angle estimation within ± 1 degree and the root mean square error (RMS) less than 0.5 degree. In addition, these results are of the same order of magnitude as the results obtained in [4], which used IMUs that were 200 times more expensive.

II. THEORETICAL BACKGROUND

Consider two body fixed frames, {A} and {B}, whose origins are located in the center of the joint rotation of two consecutive links, and the two links are connected as a 1 DOF joint (see Fig. 1). Their x-axis coincides with the rotation axis and the y-axis along the links; the z directions complete the right-hand coordinate system. The specific force vector, ${}^{A}_{I}f_{A}$, is added to the center of the joint rotation, observed in frame {A} with respect to the inertial frame and is expressed in frame {A}. ${}^{B}_{I}f_{B}$ is the same specific force but is observed and expressed in frame {B}:

$$ {}^{A}_{I}f_{A} = g_{A} + a_{A} \tag{1}$$

and

$$ {}^{B}_{I}f_{B} = g_{B} + a_{B}, \tag{2}$$

where g_A and g_B are Earth gravity expressed in frame {A} and {B}, respectively. a_A and a_B are the motion acceleration of the joint center expressed in {A} and {B}, respectively. The two expressions of the specific force have a relationship, as shown in (3):

$$ {}^{B}_{I}f_{B} = {}^{I}R_{B}^{T}\ {}^{I}R_{A}\,{}^{A}_{I}f_{A} = {}^{B}R_{A}\,{}^{A}_{I}f_{A} \tag{3}$$

${}^{I}R_{A}$ is the rotation matrix from frame {A} to the inertial frame, and matrix ${}^{I}R_{B}^{T}$ rotates a vector in the inertial frame to {B}. Then ${}^{B}R_{A}$ is the rotation matrix from {A} to {B}, with the Euler angle θ, and can be written as (4):

$$ {}^{B}R_{A} = \begin{bmatrix} 1 & 0 & 0 \\ 0 & \cos\theta & -\sin\theta \\ 0 & \sin\theta & \cos\theta \end{bmatrix}. \tag{4}$$

The links' relative angle is θ, and using (5), we can establish the relationship between this angle and the elements of specific force.

$$ \theta = atan2(f_{Ay}f_{Bz} - f_{Ay}f_{Az}\ , f_{By}f_{Ay} + f_{Az}f_{Bz}) \tag{5}$$

Here $atan2(\cdot,\cdot)$ is the function that returns the four-quadrant inverse tangent function of the two inputs. The scalars of f_{Ay}, f_{Az}, f_{By}, and f_{Bz} are the elements of ${}^{A}_{I}f_{A}$ and ${}^{B}_{I}f_{B}$ in the *y* and *z* directions, respectively.

A. Gyroscope-free IMUs

In practice, it is very hard to mount an IMU on the joint center. However, the accelerations read by IMUs on the link are dependent on the coordinates of the IMUs when the link rotates with respect to the inertial frame. Here, we utilize the approach called gyroscope-free IMUs (GFIMU), which uses multiple accelerometer outputs for calculating the angular rate and angular acceleration, as well as the specific force of the coordinate origin.

GFIMU has been widely studied [7-10]. For example, [7] investigated the performance of coordinates' configurations with IMUs for GFIMU. In [8], the use of EKF to fuse the output from GFIMU and one gyro's output was investigated as a way to overcome the problem of the sign being indistinct when angular rate was close zero. The results for implemented for pedestrian navigation.

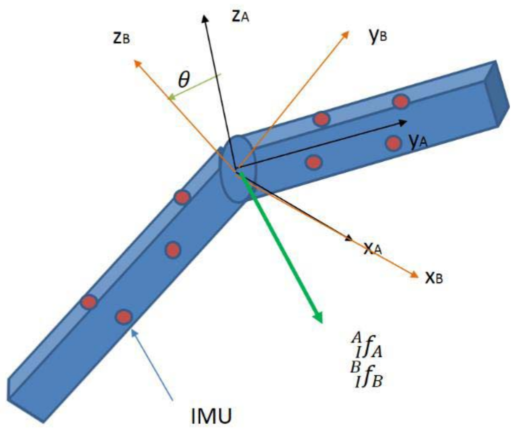

Fig. 1. Body fixed frames {A} and {B} located at the origin of the two links' joint center. The specific force of the joint center is expressed in the two frames. Each link has four IMUs with three-axis accelerometers and a three-axis gyroscope.

Here, for simplification purposes, ${}^{A}_{I}f_{A}$ is denoted as f_{Ao}, and we use frame {A} in Fig. 1 as an example in derivation below.

The specific force of the origin of frame {A} is

$$ f_{Ao} = f_{Ai} - {}^{A}\omega_{A} \times ({}^{A}\omega_{A} \times r_{Ai}) - {}^{A}\alpha_{A} \times r_{Ai}. \tag{6}$$

Here f_{Ai} is the specific force sensed by the i[th] IMU, which is attached on link A, $i \in 1,\ldots 4$. The angular rate and the angular acceleration of link A are denoted as ${}^{A}\omega_{A}$ and ${}^{A}\alpha_{A}$, respectively. In addition, the coordinates of the four IMUs are indicated as r_{Ai}.

Extract f_{Ai} (6) can be written as

$$ f_{Ai} = D_{Ai}T, \tag{7}$$

where

$$ T = \begin{bmatrix} f_{Ao} \\ {}^{A}\alpha_{A} \\ qu(\omega) \end{bmatrix} \tag{8}$$

and

$$ D_{Ai} = [I \quad -S(r_{Ai}) \quad L(r_{Ai})]\ . \tag{9}$$

In (8), the quadratic combination of the angular velocity is

$$ qu(\omega) = \begin{bmatrix} \omega_1^2 \\ \omega_2^2 \\ \omega_3^2 \\ \omega1\omega2 \\ \omega1\omega3 \\ \omega2\omega3 \end{bmatrix}, \tag{10}$$

and in (9) $S(.)$ is the following skew-symmetric matrix. L is also a function of the coordinate.

$$L(r_{Ai}) = \begin{bmatrix} 0 & -r1 & -r1 & r2 & r3 & 0 \\ -r2 & 0 & -r2 & r1 & 0 & r3 \\ -r3 & -r3 & 0 & 0 & r1 & r2 \end{bmatrix} \tag{11}$$

Stack the four IMUs of link A

$$F = DT, \tag{12}$$

where

$$F = \begin{bmatrix} f_{A1} \\ \vdots \\ f_{A4} \end{bmatrix} \tag{13}$$

is the outputs of four three-axis accelerometers stacked in one 12-element vector. In addition, D is a constant matrix and only contains the coordinate information of the IMUs:

$$D = \begin{bmatrix} D_{A1} \\ \vdots \\ D_{A4} \end{bmatrix} \tag{14}$$

Invert D, and partition it as

$$C = inv(D) = \begin{bmatrix} C_f \\ C_a \\ C_{sq1} \\ C_{sq2} \end{bmatrix}. \tag{15}$$

Then,

$$f_{Ao} = C_f F \tag{16}$$

$$^{A}\alpha_A = C_a F, \tag{17}$$

$$sq1 = \begin{bmatrix} \omega_1^2 \\ \omega_2^2 \\ \omega_3^2 \end{bmatrix} = C_{sq1} F, \tag{18}$$

and

$$sq2 = \begin{bmatrix} \omega 1 \omega 2 \\ \omega 1 \omega 3 \\ \omega 2 \omega 3 \end{bmatrix} = C_{sq2} F. \tag{19}$$

We can summarize (16)-(19) as

$$T = CF. \tag{20}$$

The output T from GFIMU can be the input of an EKF, which is described in the next section.

B. Extended Kalman filter

[8] developed the model for an EKF that fuses the output of GFIMU and the measurement of one three-axis gyroscope and estimates the angular rate, the drift of the gyros, and the bias of the accelerometers.

State that vector $x[k]$ contains 18 elements,

$$x[k] = \begin{bmatrix} \omega[k] \\ b_g[k] \\ b_a[k] \end{bmatrix}, \tag{21}$$

where $\omega[k]$ is the angular rate of one link in time step k, $b_g[k]$ is the drift of the gyroscope, and $b_a[k]$ is the bias of 4 three-axis accelerometers. The system dynamics of discrete-time are

$$x[k+1] = Ax[k] + B\tilde{F}[k] + w[k], \tag{22}$$

where the state transition matrix is

$$A = \begin{bmatrix} I & 0 & C_a \Delta t \\ 0 & e^{-D(\beta_g)\Delta t} & 0 \\ 0 & 0 & e^{-D(\beta_a)\Delta t} \end{bmatrix}. \tag{23}$$

The input matrix in (22) is

$$B = \begin{bmatrix} C_a \Delta t \\ 0 \\ 0 \end{bmatrix}. \tag{24}$$

In addition, the process noise is

$$w[k] = \begin{bmatrix} C_a \Delta t \eta_a[k] \\ \eta_{b_g}[k] \\ \eta_{b_a}[k] \end{bmatrix}, \tag{25}$$

where Δt is the sampling interval; η_a represents the white noise of the accelerometers and is a 12-by-1 vector; η_{b_g} represents the white noise for the random walk of b_g and is a 3-by-1 vector; and η_{b_a} is the white noise for the random walk of b_a and is a 12-by-1 vector.

In (22), the specific force from (16) is denoted as $\tilde{F}$ and can be regarded as a control input. The bias and drift, b_a, b_g, model as first-order Gauss-Markov random walk, in (23) the $D(\beta_a)$ represents a 12-by-12 diagonal matrix, with the element of time constant as β_a on the main diagonal. Similarly, $D(\beta_a)$ is a 3-by-3 matrix. The observation model of the EKF has a nonlinear form of

$$z[k] = h(x[k]) + v[k], \tag{26}$$

where

$$h(x[k]) = \begin{bmatrix} \omega[k] - b_g[k] \\ qu(\omega[k]) - C_{qu(\omega)} b_a[k] \end{bmatrix} \tag{27}$$

and the measurement noise is

$$v[k]=\begin{bmatrix}-\eta_{b_g}[k]\\ -C_{qu(\omega)}\eta_{b_a}[k]\end{bmatrix}. \tag{28}$$

The measurement is the output of a gyroscope on the link. In (27), the form of $qu(\omega[k])$ is given by (10). We apply one EKF developed above for four IMUs mounted on each link. For every time step, the estimated bias of accelerometers, b_a, is removed from the measurements of the accelerometers; then, (16) is again to determine the corrected specific force ${}^{A}_{I}f_A$ and ${}^{B}_{I}f_B$; finally, (5) is used to determine the relative angle of the two links, θ.

C. Complementary filter

In practice, since the noise of accelerometers are several orders of magnitude higher compared to gyroscopes, the drift of gyroscope b_g cannot be estimated properly all of the time. Therefore, we can connect a CF after estimating the EKF:

$$\begin{bmatrix}\hat{\theta}(k)\\ \hat{b}^x(k)\end{bmatrix}=\begin{bmatrix}1 & \Delta t\\ 0 & 1\end{bmatrix}\begin{bmatrix}\hat{\theta}(k-1)\\ \hat{b}^x(k-1)\end{bmatrix}+ \\ \begin{bmatrix}\Delta t & 0.5\Delta t^2\\ 0 & \Delta t\end{bmatrix}\begin{bmatrix}k_p\\ k_I\end{bmatrix}(x_2\text{-}\hat{\theta}(k-1))+\begin{bmatrix}\Delta t\\ 0\end{bmatrix}x_1, \tag{29}$$

where x_2 is the joint angle from (5) and $x_1=\omega_B-\omega_A$ is the difference of the angular velocity from the output of the gyroscope's x-axis on links B and A.

III. EXPERIMENTS

A. Test platform

The HIAB XS033 hydraulic crane shown in Figure 2 is a typical anthropomorphic arm that consists of a two-link planar arm with additional rotation about an axis of the plane called base rotation [11]. We call the first planar arm link a shoulder joint and the second an elbow joint. These shoulder and elbow joint links are labeled as A and B in Figure 1. The crane has a reach of about 5.3 meters, and its base rotation was not moved during the measurements. In Table 1, the locations of the four link-mounted IMUs are shown with lengths corresponding to the approximate measured distances from the links' joint base coordinate.

The low-cost MEMS IMU test platform consisted of eight Bosch BMI160 3-DOF IMUs mounted on arm shoulder and elbow links. The IMUs had three-axis accelerometers with the measuring range of $\pm 2\,g$ and three-axis angular rate gyroscopes with a measuring range of $\pm\,125\,\frac{deg}{s}$, both with 16-bit resolution. The maximum rate of measurement for the BMI160 IMU was $1{,}600\ Hz$.

Fig. 2. The HIAB XS033 crane used for testing.

A baseboard was designed to link the IMU to an ARM Cortex M4-powered STM32F407 microcontroller (see Fig. 3).

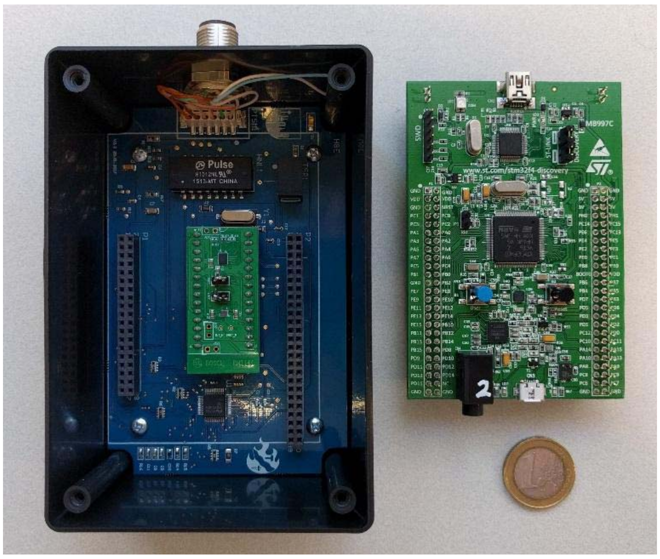

Fig. 3. A BMI160 IMU sensor prototype with its microcontroller taken out.

Each BMI160 IMU sensor node had a microcontroller that read the IMU through a serial peripheral interface (SPI). The sensor unit included an Ethernet physical layer PHY chip to realize the Ethernet UDP connection for sending data to a dSpace DS1005 real-time data acquisition and control system. Each IMU sent a total of 12 bytes of raw data to the DS1005 at a rate of 400 Hz. The DS1005 ran a Simulink model in real time. Each IMU sent its data to a unique UDP port number, which allowed for different IMU data identification and parallel data acquiring for the sensor data fusion. The joint angles were also measured with two Posital Fraba incremental rotary encoders (accuracy 16384 increments/revolution) on the crane's shoulder and elbow joints to serve as an accurate ground truth reference to the developed joint angle estimates.

Table 1. IMUs' Position Coordinates on Links A and B

$[x,y,z]^T(m)$	IMU 1	IMU 2	IMU 3	IMU 4
Shoulder link (link A)	0.19 -0.13 -0.04	-0.19 -0.15 -0.08	-0.19 0 0	0.1 1.50 0.02
Elbow link (link B)	0.175 0.22 0	0.175 0.37 0.08	-0.06 0.22 0.02	-0.06 1.68 -0.05

Table 1 provides a list of approximate IMU positions mounted on the shoulder and elbow links. The body frames of the IMUs were parallel to the links' body fixed frames. The test performance depended on the chosen IMU mounting coordinates. In practice, we could not freely choose the mounting position for each IMU to obtain optimal performance of the algorithm since the hydraulic manipulators' link surfaces had cables, hydraulic hoses, and pipes. However, the recommended criterion of the mounting positions for the IMUs was to make the diagonal elements of matrix W as small as possible, meaning that the measurement noise of the accelerometers would be smaller when the proposed algorithm was applied as follows:

$$W = CC^T, \tag{30}$$

where C is a 12-by-12 matrix in (20), which only contains the coordinate information of the IMUs.

B. *Experiment results*

In Figure 4 below, the upper plot shows the motion of the shoulder and elbow joint angles, with blue and red lines, respectively. The lower part of the Figure 4 shows the angle estimation errors, in which we used the joint angle encoders as the ground truth reference. The blue line represent estimation without reducing the bias b_a, from the measurements of each accelerometer; and for the estimation of red line, after the EKF get the b_a, it is removed from the measured accelerations, the specific forces f_{Ao} and f_{Bo}, which are expressed in the origin of $\{A\}$ and $\{B\}$, are calculated again.

In Figure 5, the angle estimation is compared with the accurate encoder reference. The error peaks occur when the motion changes direction, which means at that at these points, the dynamic accelerations added to the joint rotation centers are changed significantly. By increasing the complementary filter gain, k_p, in (29), we might be able to reduce the value of the peak errors. However, this would take more information from the IMU accelerations, which would introduce more noise in the estimation results. In this test, k_p and k_I were set as 12 and 0.02, respectively.

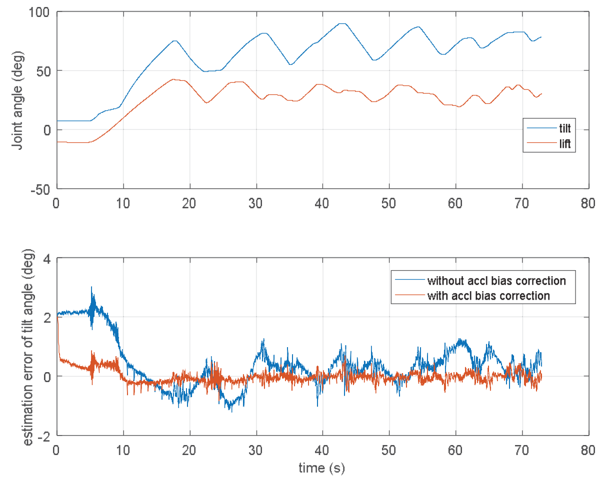

Fig. 4. The top graph shows the motion of the shoulder and elbow joint angles during the test, while the lower graph shows the test results with and without correcting the bias of the accelerometers.

Table 2 provides a summary of the joint angle estimation errors with and without the accelerometer bias correction. With the bias correction, the accuracy of the estimation improved significantly regarding implementation with low-cost IMUs. The data shown are statistics from the steady states of the EKF, from 0.5 seconds to the test end, about 73 seconds.

Table 2. Errors in Angle Estimation

	Peak abs. error (deg)	*Mean abs. error (deg)*	*Root mean square error (deg)*
With correction of accelerometers bias	0.887	0.154	0.202
Without correction of accelerometers bias	3.019	0.624	0.874

Figure 6 show the bias of one accelerometer on the *x*-, *y*-, and *z*-axes installed on link A in coordinates [0.19, -0.13, -0.04] with respect to body fixed frame A. We can see that after several seconds, each axis bias approximately converges to their steady-state value. We attach the nodes of IMUs on the surfaces of links manually; there exist inaccuracy of orientation and position of them. In addition, the hydraulic manipulators might not move exactly on the vertical plane, so except for the measurement noise and the bias of the IMUs' measurements, some new errors are introduced with respect to the nominal state. We can use the state of the accelerometer bias b_a to absorb all these errors. Note that in these test cases, the low-cost IMUs have no precalibration done in the lab or on turntables.

IV. CONCLUSION

In this paper, we describe how we built a sensor network with low-cost MEMS IMUs for the angle estimation of floating-base robotic systems. The proposed algorithm uses the measurements of four accelerometers mounted on each robot link to calculate the specific force at the coordinate origin and the link's angular acceleration. These estimates are then fused with the gyroscope measurements utilizing a complementary filter to obtain the desired joint angle estimate.

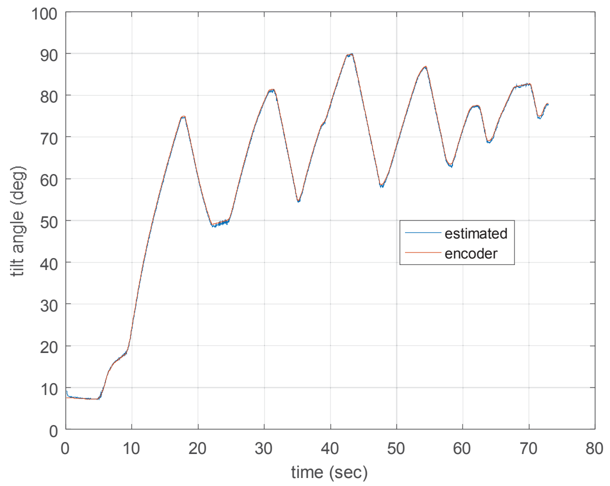

Fig. 5. Comparison of the angle estimation and encoder output for the elbow angle, indicated with blue and red line, respectively. The estimation one uses the EKF to correct the bias of acceleration.

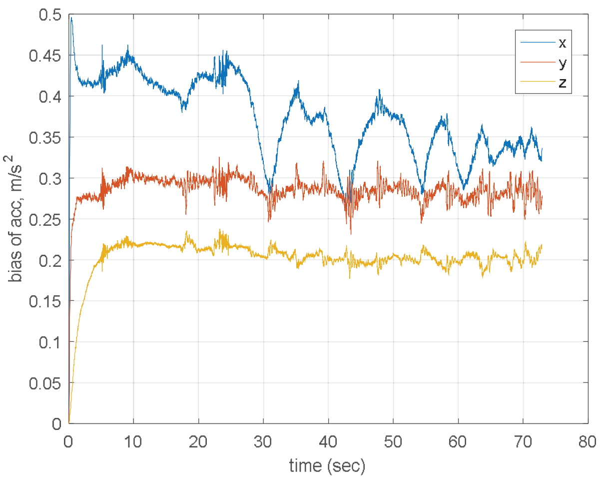

Fig. 6. Estimated bias of one 3-DOF accelerometer in link A.

The novelty of the developed algorithm is that the use of a forward kinematic model requiring data flow between consecutive joints is not needed. Our initial measured results with a two-link planar arm validate the algorithm in 2-D motion. Even with very low-cost 3-DOF IMUs (costing less than USD 5 each) and without any precalibration of these IMUs, the accuracy of the joint angle estimation is better than 0.5 degrees (RMS).

The proposed algorithm can be used for real-time robot motion control, and its performance for horizontal base rotation of joint angle estimation should be further studied and tested. As a next step, we also plan to validate our algorithm in a full-scale rough terrain vehicle with the base moving at 6-DOF. In addition, the random walk behavior of the gyroscopes should be further investigated. Currently, we mainly use a CF to remove the drift in the gyroscopes and simply set the process noise for the random walking at close to zero for the EKF.

Acknowledgments

This research work was supported in part by the Doctoral School of Industry Innovations (DSII), by Tampere University of Technology (TUT), the Forum for Intelligent Machines (FIMA), and the Academy of Finland (Grant no. 294915).

References

[1] Koivumäki, J., Honkakorpi, J., Vihonen, J., & Mattila, J. (2014, July). Hydraulic manipulator virtual decomposition control with performance analysis using low-cost MEMS sensors. In *Advanced Intelligent Mechatronics (AIM), 2014 IEEE/ASME International Conference on* (pp. 910-917). IEEE.

[2] Vihonen, J., Honkakorpi, J., Tuominen, J., Mattila, J., & Visa, A. (2016). Linear accelerometers and rate gyros for rotary joint angle estimation of heavy-duty mobile manipulators using forward kinematic modeling. *IEEE/ASME Transactions on Mechatronics*, *21*(3), 1765-1774.

[3] Vihonen, J., Honkakorpi, J., Mattila, J., & Visa, A. (2015, May). Novel pairwise coupled kinematic solution for algebraic angular acceleration estimation of serial link manipulators. In *Robotics and Automation (ICRA), 2015 IEEE International Conference on* (pp. 809-814). IEEE.

[4] Vihonen, Juho, Mattila, J& Visa, A. (2017, in press). Joint-space kinematic model for gravity-referenced joint angel estimation of heavy-duty manipulators. *IEEE Transactions on Instrumentation and Measurement.*

[5] Rotella, N., Mason, S., Schaal, S., & Righetti, L. (2016, May). Inertial sensor-based humanoid joint state estimation. In *Robotics and Automation (ICRA), 2016 IEEE International Conference on* (pp. 1825-1831). IEEE.

[6] Xinjilefu, X., Feng, S., & Atkeson, C. G. (2016, May). A distributed MEMS gyro network for joint velocity estimation. In *Robotics and Automation (ICRA), 2016 IEEE International Conference on* (pp. 1879-1884). IEEE.

[7] Escobar Alvarez, H. D. (2010). Geometrical configuration comparison of redundant inertial measurement units (MSc Thesis, University of Texas USA).

[8] Williams, T., Pahadia, A., Petovello, M., Lachapelle, G., "Using an Accelerometer Configuration to Improve the Performance of a MEMS IMU: Feasibility Study with a Pedestrian Navigation Application," *Proceedings of the 22nd International Technical Meeting of The Satellite Division of the Institute of Navigation (ION GNSS 2009)*, Savannah, GA, September 2009, pp. 3049-3063.

[9] Schopp, P., Klingbeil, L., Peters, C., Buhmann, A., & Manoli, Y. (2009). Sensor fusion algorithm and calibration for a gyroscope-free IMU. *Procedia Chemistry*, *1*(1), 1323-1326.

[10] Park, S., Tan, C. W., & Park, J. (2005). A scheme for improving the performance of a gyroscope-free inertial measurement unit. *Sensors and Actuators A: Physical*, *121*(2), 410-420.

[11] Sciavicco, L., & Siciliano, B. (2000). Modeling and Control of Robot Manipulators, London, Spring

PUBLICATION
II

Angle estimation for robotic arms on floating base using low-cost IMUs

Xiaolong Zhang, Eelis Peltola, and Jouni Mattila

DOI: 10.1109/ICRA.2018.8462898

2018 IEEE International Conference on Robotics and Automation (ICRA)
May 21-25, 2018, Brisbane, Australia

Angle estimation for robotic arms on floating base using low-cost IMUs

Xiaolong Zhang, Eelis Peltola, and Jouni Mattila

***Abstract*— An algorithm that uses low-cost inertial measurement units (IMUs) for estimating link angles for floating base robotic platforms is proposed. Each link has four IMUs attached on its surfaces, and an Extended Kalman Filter (EKF) and a Complementary Filter (CF) are used for fusing the sensors' data. The algorithm is validated with a commercial mobile working machine, which consist of six degrees-of-freedom (DOF) wheeled base platform, and a 3-DOF hydraulic anthropomorphic arm. Although there are vibrational disturbances from the machine's diesel engine and deformation of the links themselves, the measured results from the planar motion of a floating base hydraulic arm show that the accuracy of the angle estimation is impressively less than 1 degree in the root mean square (RMS) error.**

I. INTRODUCTION

For navigation or pose estimation, strap-down microelectromechanical system (MEMS) IMUs are widely used nowadays in all kinds of mobile devices, from mobile phones to cars and more. Off-road heavy-duty working machines (such as excavators in construction, forwarders in forestry, and drill rigs in mining) markets form a massive industrial sector, with global construction machine sales alone reaching 700,000 units in 2016 [1]. With a motivation to automate their hydraulic manipulators to lower operating costs and increase productivity, these machines have huge potential for autonomous hydraulic robotics (for example, global sales of industrial robots in 2019 is predicted to be only 400,000 units [2]). The advent of robotics is projected to revolutionize the heavy-duty machine industry [3], and many of those machines would benefit greatly from an alternative to costly and hard-to-install joint resolvers and potentiometers traditionally used for manipulator joint angle feedback.

In an attempt to reduce system cost and improve robustness, the use of cheap MEMS-based IMUs for estimating the state of manipulator joints has been investigated in [4], [5]. However, these studies assume the base of the manipulator is stationary (or fixed based). Recently, [6] developed an algorithm for pose estimation of arms with a floating base; one high-quality IMU, which cost more than 1000 USD each, was applied to each link. However, this algorithm did not include an estimation of accelerometer bias, and the angular acceleration was derived from the time derivative of angular velocity. These assumptions clearly limit the use of the approach to only high-quality IMUs that have low accelerometer bias and low gyroscope noise.

In [7], a tactical-grade fiber optic 6-DOF IMU (KVH1750 costing over 15 000 USD each), was used as an accurate reference point for a network of low-cost MEMS gyros for humanoid joint velocity estimation, and therefore high-cost accurate base state IMU was required.

In [4], [5], a forward kinematic model with data flow from previous links was used for IMU-based motion estimation of fixed base manipulator. This makes the algorithm complex, and any imperfect estimation for the state of previous links or base will propagate to the end of the links. The work in [8] used traditional joint position sensors (potentiometers) in their IMU sensor fusion method, which used pairwise IMUs on each consecutive link for the joint acceleration estimation, but the accelerometer bias was not included in the estimation. Pose estimation using a fusion of IMUs and other sensors, such as cameras [9], magnetometers [10] and ultra-wide band systems [11], has been studied widely. However our approach has the advantage of using only one kind of strap-down IMUs, resulting in easier implementation and more robust final system. Most other sensors, particularly cameras, also significantly raise the system cost and decrease the applicability and robustness.

The aim of the work presented in this paper is to develop an algorithm that uses low-cost IMUs for the state estimation of robotic arms mounted on a floating base thereby removing the need to use a traditional forward kinematic model. In [12], we initially tested our algorithm with low-cost IMUs on a planar hydraulic arm where the first joint was moved to generate a motion disturbance to the second joint angle we estimated. A RMS error of 0.202 degrees was observed in the estimated angle. However, the disturbance motion only had one DOF, and no diesel engine induced vibrational disturbances were present.

The proposed algorithm for the estimation of link angles uses three-axis gyroscope and three-axis accelerometer IMUs that cost less than 5 USD each (Bosch BMI160). We use four strap-down IMUs mounted on each link's surface to form a single virtual IMU whose body-fixed frame's origin is located at the center of the joint's rotation axis. We show that the same specific force added to the joint center can be expressed in two of these fixed frames. Through algebraic manipulation of the elements of the specific force that are output from the two fixed frames, we can determine the relative angle of the two links. We then apply an EKF and a CF to fuse this angle with the outputs of the gyros and estimate the accelerometer bias and drift of the gyros to decrease the noise of the proposed angle estimation.

*This research work was supported in part by the Doctoral School of Industry Innovations (DSII), Tampere University of Technology (TUT), the Forum for Intelligent Machines (FIMA), and the Academy of Finland (Grant no. 294915).

Xiaolong Zhang, Eelis Peltola and Jouni Mattila are with the Department of Automation and Hydraulic Engineering, Tampere University of Technology, FI-33101, Finland. E-mail:firstname.surname@tut.fi

In this paper, we validate the proposed algorithm with a heavy-duty mobile working machine with an anthropomorphic arm [13], as shown in Fig. 1. The swing joint, which connects the three-link arm and the machine's base, was only used to move the plane of the arm and its angle was not estimated in the current work. The mobile machine was a floating-base 6-DOF wheeled-platform and had a running diesel engine for a full-scale test scenario, see Fig. 3.

The measured results show that our theory is valid, with the accuracy of the joint angle estimation within 1 degree in RMS error, which is the same order of magnitude as in studies utilizing high-cost IMUs [6].

The error analysis shows that one of the main error sources is the deformation and/or oscillation of links when external torques are present, which violates the assumption of rigid body kinematics in our algorithm. The other error source is the high frequency disturbance caused by the machine's engine, which increases the noise in the IMUs' measurements. This also increases the convergence time of our algorithm.

This paper is organized as follows: in Sect. II, the mathematical foundations for calculating manipulator joint angles with IMU measurements are introduced. The experimental setup for the algorithm is shown in Sect. III, where low-cost IMUs are used to make measurements from the movement of an off-road heavy-duty platform with a hydraulic manipulator. Test results are given in Sect. IV-A with error analysis. Finally, discussion of the results is presented in Sect. V, and the conclusions are outlined in Sect. VI.

II. Joint angle estimation with IMUs

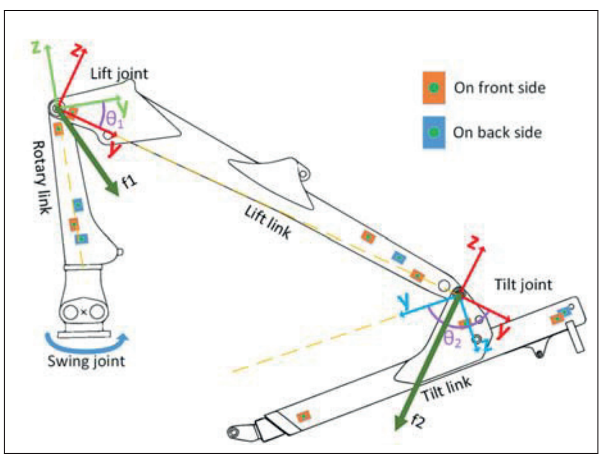

Fig. 1. 2-D chart of the hydraulic links of test platform, body-fixed frames, and IMU boxes on the links.

A. Angle calculation with gravity-aiding

In Fig. 1, $f1$ and $f2$ indicate the specific forces expressed in an inertial frame, which are added in the joint center for the lift and tilt angles, respectively. Using the tilt angle as an example, we define the origins of the two body-fixed frames as being in the joint center. Also, the two x-axes coincide with the rotation axis, their y-axes are along the links, and z-axes complete the right-hand coordinate system. The force added in the center of tilt joint can be written as the following:

$$f2 = {}^I R_t {}^t_I f_t = {}^I R_l {}^l_I f_l, \tag{1}$$

where ${}^I R_t$ and ${}^I R_l$ are the rotation matrices from body fixed frames of the tilt link and lift link to the inertial frame respectively. ${}^t_I f_t$ and ${}^l_I f_l$ are the specific forces with respect to the inertial frame, but expressed in the body fixed frames of the tilt and lift links, respectively. From (1) we can derive the following:

$${}^t_I f_t = {}^I R_t^T {}^I R_l {}^l_I f_l, \tag{2}$$

and the rotation matrix from the body-fixed frame of the lift link to tilt link is the following:

$${}^t R_l = {}^I R_t^T {}^I R_l = \begin{bmatrix} 1 & 0 & 0 \\ 0 & \cos\theta_2 & -\sin\theta_2 \\ 0 & \sin\theta_2 & \cos\theta_2 \end{bmatrix}. \tag{3}$$

From (2) and (3), we get the following joint angle:

$$\theta_2 = atan2\left(f_{ty}f_{lz} - f_{ty}f_{tz}\ , f_{ly}f_{ty} + f_{tz}f_{lz}\right), \tag{4}$$

where $atan2(\cdot,\cdot)$ is the function that returns the four-quadrant inverse tangent function of the two inputs, and f_{ty}, f_{lz}, f_{tz}, and f_{tz} are the scalar elements of ${}^t_I f_t$ and ${}^l_I f_l$ in y-axis and z-axis. It is well known that the specific force is the gravity plus the motion force. Assume two IMUs can be installed in the tilt joint center, but their coordinates are aligned with the body-fixed frame of the joined links. The outputs of the installed IMUs' accelerometers are the following:

$${}^t_I f_t = g_t + a_t + n \tag{5}$$

$${}^l_I f_t = g_l + a_l + n, \tag{6}$$

where g_t and g_l are gravity expressed in the body-fixed frames of the tilt and lift links, respectively. a_t and a_l are the motion accelerations of the tilt-joint center expressed in the same body-fixed frames. n is the Gaussian noise of the accelerometers. From (4)-(6), we notice that once the specific force of the joint center has a projection in the motion plane of the links, the joint angle can be calculated through the output of the accelerometers.

B. Gyroscope Free IMU (GFIMU)

In practice, it is impossible to install IMUs exactly on the joint's center. We introduce the approach of gyroscope free IMUs (GFIMUs). GFIMUs use four 3-axis accelerometers that are attached on a rigid body to get the specific force, angular acceleration, and quadratic form of the angular rate on any point of the body; details can be found in [14], [15]. Through GFIMU, we can form a virtual IMU mounted in the rotation center and get rid of the forward kinematic model that is applied to the state estimation of serial links. It is also relatively easy for us to choose the positions of IMUs on the platform's links, as shown in Fig. 1, where the squares with dots indicate the IMUs boxes on links.

$$T = CF \tag{7}$$

where

$$T = \left[\begin{array}{c} f_{Ao} \\ {}^{A}\alpha_{A} \\ qu\left(\omega\right) \end{array} \right]. \tag{8}$$

In (8), f_{Ao} indicates the specific force at the joint center of link A expressed in the frame of link A, ${}^{A}\alpha_{A}$ is the angular acceleration of link A expressed in the frame of link A, and

$$qu\left(\omega\right) = \left[\begin{array}{c} \omega_1^2 \\ \omega_2^2 \\ \omega_3^2 \\ \omega 1 \omega 2 \\ \omega 1 \omega 3 \\ \omega 2 \omega 3 \end{array} \right] \tag{9}$$

(9) is the quadratic form of the angular rate for link A, expressed in link A. In (7), F is the measurement of the four IMUs' accelerometers, and C is a constant matrix, which only contains the position information of the four IMUs on link A. Since T has 12 elements, the minimal requirement for sensors is 4 IMUs with 3-D accelerometer on each link. Details can be found in [14] and Sect. III-B.

C. Data fusion

[14] developed the model for an EKF which fuses the output of GFIMUs to estimate the bias of the accelerometers and drift of the gyroscopes. The state vector contains 18 elements as follows:

$$x\left[k\right] = \left[\begin{array}{c} \omega\left[k\right] \\ b_g\left[k\right] \\ b_a\left[k\right] \end{array} \right], \tag{10}$$

where $\omega[k]$ is the angular rate of one link in time step k, $b_g[k]$ is the drift of the gyroscope, and $b_a[k]$ is the bias of four accelerometers with a triad-axis. The process model is as follows:

$$x\left[k+1\right] = Ax\left[k\right] + B\tilde{F}\left[k\right] + w\left[k\right], \tag{11}$$

where the state transition matrix is as follows:

$$A = \left[\begin{array}{ccc} I & 0 & C_a \Delta t \\ 0 & e^{-D(\beta_g)\Delta t} & 0 \\ 0 & 0 & e^{-D(\beta_a)\Delta t} \end{array} \right] \tag{12}$$

and the input matrix is as follows:

$$B = \left[\begin{array}{c} C_a \Delta t \\ 0 \\ 0 \end{array} \right].$$

The matrix of noise for the states is as follows:

$$w\left[k\right] = \left[\begin{array}{c} C_a \Delta t \eta_a\left[k\right] \\ \eta_{b_g}\left[k\right] \\ \eta_{b_a}\left[k\right] \end{array} \right], \tag{13}$$

where Δt is the sampling interval; C_a is a constant matrix and the part that corresponds to the angular acceleration in matrix C of (7); η_a represents the white noise of the accelerometers and is a 12 by 1 vector; η_{b_g} represents the white noise for the random walk of b_g and is a 3 by 1 vector' and η_{b_a} is the white noise for the random walk of b_a and is a 12 by 1 vector. In (11), the specific force from (7) is denoted as $\tilde{F}$ and can be regarded as a control input. The bias and drift, b_a, b_g, are modeled as first-order Gauss-Markov random walk, in (12) the $D(\beta_a)$ represents a 12 by 12 diagonal matrix, with the element of time constant as β_a on the main diagonal. Similarly, $D(\beta_g)$ is a 3 by 3 matrix.

The observation model has a nonlinear form as follows:

$$z\left[k\right] = \left[\begin{array}{c} \omega\left[k\right] - b_g\left[k\right] \\ qu\left(\omega\left[k\right]\right) - C_{qu(\omega)} b_a\left[k\right] \end{array} \right] + \left[\begin{array}{c} -\eta_{b_g}\left[k\right] \\ -C_{qu(\omega)}\eta_{b_a}\left[k\right] \end{array} \right] \tag{14}$$

The measurement is the average of the outputs of the gyroscopes on the link and the quadratic form of the angular rate from (9). We apply one EKF developed above for four IMUs mounted on each link. For every time step, the estimated bias of accelerometers, b_a, is used to correct the specific force for the joint center of each link, and (4) is used to determine the relative angle of the two links, θ.

D. Complementary filter

The angle θ has a high noise, and we use a complementary filter to smooth it.

$$\left[\begin{array}{c} \hat{\theta}\left(k\right) \\ \hat{b}^x\left(k\right) \end{array} \right] = \left[\begin{array}{cc} 1 & \Delta t \\ 0 & 1 \end{array} \right] \left[\begin{array}{c} \hat{\theta}\left(k-1\right) \\ \hat{b}^x\left(k-1\right) \end{array} \right]$$

$$+ \left[\begin{array}{cc} \Delta t & 0.5\Delta t^2 \\ 0 & \Delta t \end{array} \right] \left[\begin{array}{c} k_p \\ k_I \end{array} \right] \left(x_2 - \hat{\theta}\left(k-1\right)\right) + \left[\begin{array}{c} \Delta t \\ 0 \end{array} \right] x_1, \tag{15}$$

where measurement x_2 is the joint angle from (4), and $x_1 = \omega_B - \omega_A$ is the difference of the angular velocity from the output of EKF for the gyroscope's x-axis. $\hat{\theta}\left(k\right)$and $\hat{b}^x\left(k\right)$ are the estimated angle and bias.

The estimation process for the joint angles is summarized in Fig. 2.

III. Experiments

A. Experimental setup

The Ponsse Caribou is a 12-ton, 8-wheel forest forwarder used to load and carry logs, and is shown in Fig. 3. It includes a typical four-link heavy-duty hydraulic manipulator arm. The first three 1-DOF joints compose an anthropomorphic arm, and the last joint is prismatic, effectively making the last link an extension. This extension link was not considered in our setup, bringing the effective outreach of the arm to 5.5 meters. Our naming convention for the used links is seen in Fig. 1. The forest forwarder acts as a floating base for the arm.

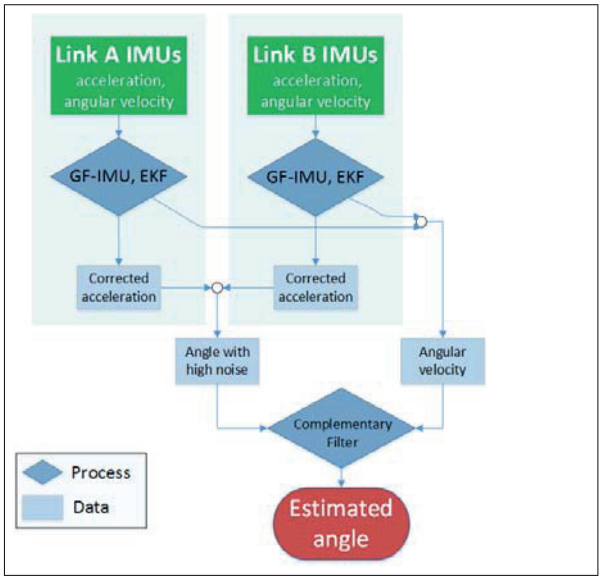

Fig. 2. Flowchart of processing for the joint angle estimation

Fig. 3. The forest forwarder mobile test platform, completed with manipulator arm.

For the algorithms in this paper, each measured joint angle needs four IMUs mounted on the links connected to that joint. We are estimating two joint angles connected in series, which means that the total number of IMUs needed is 12, as shown in Fig. 1. The placement of the IMUs was chosen first by hand using educated guesses and then verified with an algorithm described in Sect. III-B.

B. Position of IMUs on links

It is well-known that the specific force on any point of a rigid body can be written as the following:

$$f_{Ai} = f_{Ao} + {}^{A}\omega_A \times \left({}^{A}\omega_A \times r_{Ai}\right) + {}^{A}\alpha_A \times r_{Ai}, \quad (16)$$

where f_{Ai} denotes the specific force of the i^{th} point on link A, which has the coordinate r_{Ai}. f_{Ao} is the specific force in the origin of body-fixed frame A, ${}^{A}\omega_A$ is the angular rate of link A, and ${}^{A}\alpha_A$ is the angular acceleration; all of these are expressed in body-fixed frame A.

With (16), to get a linear expression, ${}^{A}\omega_A$ is written as its quadratic form, $\left[\begin{array}{ccc}\omega_1^2 & \omega_2^2 & \omega_3^2\end{array}\right]^T$ and $\left[\begin{array}{ccc}\omega_1\omega_2 & \omega_1\omega_3 & \omega_1\omega_3\end{array}\right]^T$. Regard these two vectors as two unknowns and f_{Ao}, ${}^{A}\alpha_A$ as the other two unknowns. If we have the values of the specific forces for four points on link A, we can extract the coordinates information into a matrix D:

$$F = DT, \quad (17)$$

where T has the same meaning and form as in (7), F is a 12 by 1 vector that stacks the specific forces of four points, and D is the following:

$$D = \left[\begin{array}{c} D_1 \\ \vdots \\ D_4 \end{array}\right]. \quad (18)$$

In (18), each element of D has a form of the following:

$$D_i = \left[I \quad -S\left(r_{Ai}\right) \quad L\left(r_{Ai}\right)\right] \ , \quad (19)$$

where $S\,(\ .)$ is the following skew-symmetric matrix. L is also a function of the coordinate r_{Ai}.

$$L\left(r_{Ai}\right) = \left[\begin{array}{cccccc} 0 & -r1 & -r1 & r2 & r3 & 0 \\ -r2 & 0 & -r2 & r1 & 0 & r3 \\ -r3 & -r3 & 0 & 0 & r1 & r2 \end{array}\right] \quad (20)$$

Matrix D is the inverse matrix of C in (7). We assume all the IMUs in our tests are of the same quality, and the standard deviation of their Gaussian noises are on the same level. Multiply C with its transpose, as follows:

$$W = CC^T. \quad (21)$$

Denote the diagonal elements of W as N, which is applied as the criterion for choosing the positions of IMUs on links. With (21) and (7), we notice that the first three elements in N use the measurements of the accelerometers of the IMUs to get the specific force in the joint center, the next three elements for the angular acceleration, and the last six elements for the quadratic form of angular rate.

In practice, the placements cannot be chosen freely, because hydraulic manipulator links have uneven surfaces, pipes and hydraulic hoses that come in the way of mounting. We try to keep the first three numbers of N smaller than 2 when choosing the position of the four IMUs on one link, which means the diagonal elements of the covariance matrix for the specific force in the joint center is two times larger than the measurements of the IMUs' accelerometers. Similarly, keep the other elements of N smaller than 100, meaning the standard deviation of noise for angular acceleration and quadratic form of angular rate in T is 10 times less than that of accelerometers'.

The final placements for the IMUs are provided in Table I. The choices for the IMUs' positions are not optimal, but they are acceptable noise ratios for implementation of the

GFIMUs, while also being convenient for us to attach the IMUs on the platform's links.

TABLE I
IMU POSITION COORDINATES

	IMU #	Coordinates [x, y, z] (m)		
Swing link	1	-0.142	0.057	-0.642
IMUs in	2	-0.143	-0.030	-0.934
reference to	3	0.141	-0.015	-0.185
link joint	4	0.142	0.046	-0.860
Lift link	1	0.082	0.093	0.001
IMUs in	2	0.035	2.934	0.051
reference to	3	-0.243	3.047	-0.009
link joint	4	0.032	3.154	-0.044
	IMU #	Coordinates [x, y, z] (m)		
Lift link	1	0.082	-3.411	0.001
IMUs in	2	0.035	-0.570	0.051
reference to	3	-0.243	-0.457	-0.009
tilt joint	4	0.032	-0.350	-0.044
Tilt link	1	0.020	-0.650	0.498
IMUs in	2	-0.223	-0.622	0.372
reference to	3	0.075	0.112	0.138
tilt joint	4	0.020	0.972	0.525

C. Sensor implementation

MEMS technology has enabled cheap and small inertial sensors, resulting in ubiquitous use and availability, for example, [16]–[18]. In this setup, the low-cost MEMS IMU used was a Bosch BMI160 6-DOF IMU, featuring a three axis accelerometer and three axis gyroscope, at a market price of less than four euros. This results in the use of four low-cost IMUs on one link being considerably cheaper than using one high-cost IMU, as in [5]. Each IMU was implemented in a sturdy IP66-protected box with the following hardware:

- Bosch BMI160 IMU development shuttleboard, featuring the BMI160 IMU and BMM150 magnetometer. The magnetometer was not used because metallic bodies interfere with it, making it unreliable. The BMI160 accelerometer range was configured to $\pm 8\ g$, and the gyroscope range to $\pm 125\ \frac{\text{deg}}{s}$. Both are given in 16-bit resolution by the BMI160.
- ARM Cortex M4 -powered STM32F407 Discovery micro-controller development board. Used for reading the IMU through a serial peripheral interface (SPI) and sending the read data forward to a computer with a Ethernet user datagram protocol (UDP). Programmed graphically in Simulink with the Waijung third-party blockset, which compiles the Simulink model to STM32F407-compatible C code.
- A custom-designed base board, hosting the aforementioned boards, a power regulator, an Ethernet physical layer (PHY) chip, and other electronics needed to support the Ethernet connection.

The electronics are pictured in a plastic box in Fig. 4. The actual black BMI160 chip, with a width of 3 mm, can be seen slightly above the center on its shuttleboard. The same M12 connectors pictured are used in our metallic boxes. Each IMU sent a total of 12 bytes of raw data (two for each axis, six axes in total). Data from the IMUs were first sent to a Simulink Real-Time target computer, where it was gathered into a single vector for each time step and sent forward to the dSpace MicroAutoBox II. For reference regarding the IMU data, both estimated joints also had a Heidenhain ROD 456 incremental encoder.

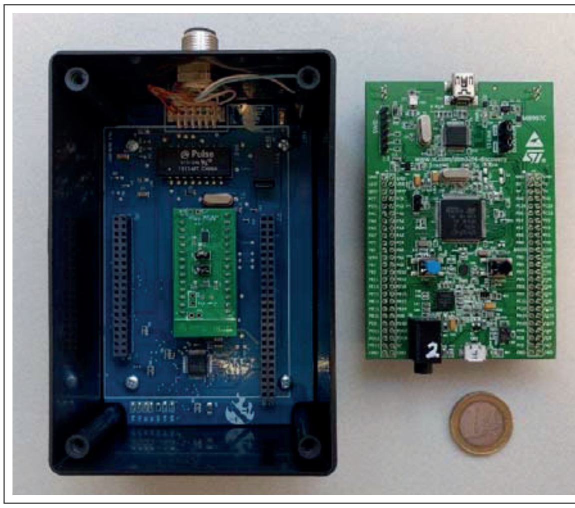

Fig. 4. The electronics used. BMI160 shuttleboard on the base board, and the STM32F407 development board taken out of the box.

We collected data with dspace MicroAutoBox II, and validate the algorithm offline in current phase. Please notice, each of our IMU box has a micro-controller of STM32F407, even one of them can support the computation for all the EKF and CF of the three links in real-time at 400 Hz.

IV. TEST RESULTS

A. Summary of test results

TABLE II
TEST RESULTS

	standard deviation	mean abs. error	maximum error
tilt(deg)	0.947	0.612	4.49
lift(deg)	0.638	0.480	1.952

In Table II, we summarize the results of one general test for the algorithm we propose in this paper. The angles' measurements from encoders are set as references; the standard deviation, mean of absolute error, and maximum of absolute error are listed. They are counted from the first time step to the end of the test. The prior states for the EKF use zeros, and a zero is used for the prior value of $\hat{b}^x$ in CF. During the test, all three joints of platform links were rotated arbitrarily in a plane by a human operator using open-loop control. The angle positions are shown at the top of Fig. 5. The off-road working machine was driven several times from even ground to a slope made of rubble. This fully forms a moving 6-DOF platform for the hydraulic links. The base's motion is not shown in Fig. 5. The estimation error of the tilt and lift angles are shown in the middle and bottom, respectively. Because the engine of the vehicle is running at the time of testing, extra disturbance of oscillation is transferred to the links. This is analyzed in detail in Sect. IV-B. Currently, we validate the algorithm with angle estimations only for the tilt and lift joints; estimating the swing angle is our next goal.

B. Analysis of error sources

The algorithm we propose assumes all the links are rigid bodies, which means that on the same link, the angular rate is the same at any point, that if the IMUs' orientations on one link are aligned, output of the angular rates should be close to each other, with the exception of some offset or drift. However, during practice tests, each link has some bending and oscillation because of external torque, and the assumption of a rigid body is not held at all times. In Fig. 6, the four plots focus on a part of the test for tilt angle estimation as the rotation angle changes at high speed. The upper left plot indicates the difference of the angular rate between two IMUs on the lift link in the x direction, and the peak of this difference reaches more than 5 $\frac{deg}{s}$, even though the two IMUs are on the same link. The upper right plot indicates the angle value we get from equation (4): it shows that the high frequency oscillation of the link itself has a significant effect for specific force estimation on the joint's center. The bottom left plot in Fig. 6 shows the estimation result of the tilt angle: the blue line indicates the estimation result, and the red line is the output from the encoder, which is regarded as a ground truth reference. The bottom right part shows the estimation error: its peak value is about 11 degrees. This error peak occurs when the joint angle changes from -55 degrees to -95 degrees and goes back within 1 second. One of the two IMUs is located close to the link joint, and the other is close to the lift joint. The distance between them is about 3 m, so as the lift link undergoes high angular acceleration, the link's deformation or oscillation worsens the estimation. When the engine of the test machine is turned on, the vibration of the engine will transfer to the links. As an example, the upper plot in Fig. 7 indicates the accelerometer's output of IMU number 9 in the x direction when the machine's engine is started; the bottom plot shows the gyroscope's output in the y direction for the same IMU and at the same time.

The same data for Fig. 5 are outputted in Fig. 8 in a different form, the regions of error peak, and the links that stay in stationary status are enlarged. The red and dark lines indicate the encoder's measurement and estimation for the angle of lift joint, respectively. The blue and green lines are for the angle of the tilt joint from encoder and its estimation. The dark star and pink star indicate the error peak of the estimation for the tilt and lift angle, respectively. The angle position of the swing joint and the base's motion are not shown in Fig. 8.

From the enlarged sub-boxes, we can say that the peaks of errors for angle estimation mainly occur as the joints rotate at a high speed. In this situation, the links may just have high angular acceleration, the links' deformation cause the angle estimation with (4) to become worse; although this deformation can recover within a very short time, the convergence time of estimation with the CF described in (15) increases. This leads to bigger error for the final angle estimation, and the shape of the estimation curve has a delay compared to the output from the encoder.

The enlarged section for the end of the estimation shows that when the links are stationary, which means the angles' positions have no motion, but the machine's engine is turned on, and the errors are smaller; as measured, the errors of RMS are less than 0.4 degrees for both joints.

V. Discussion

In Sect. IV-B, we noticed that the non-rigid property of links introduces error for the estimation of joint angles in our algorithm. The most direct way to avoid this disadvantage is to shorten the distance between IMUs on a single link. Currently, the IMUs on the lift link are positioned so that three of them are close to the tilt joint, and the fourth is close to the lift joint. Moving the fourth IMU closer to the other three would decrease the effect of the oscillation of the link itself to the angle estimation of the tilt joint angle. Alternatively, moving the other three IMUs closer to the lift joint would improve the estimation of the lift joint angle. To simplify the hardware network, we use the IMUs on the tilt link both for tilt and lift joints' angle estimation. Because choosing a longer distance between IMUs can make the elements of N smaller, choosing a distance is a trade-off for our test platform between avoiding the bending of the link affecting the measurements and having less noise when calculating the elements of T.

For the disturbances introduced by the engine shown in Fig. 7, we use (15) as a low frequency pass filter to filter the high frequency oscillation from the engine. The amplitude and frequency of the engine's disturbances also change as the engine's output power changes, and this changes the time to the steady states as other disturbances added. An adaptive filter should perhaps be considered as a choice. Currently, the machine's engine is running throughout the entire test, and in (15), we set the gain, k_p and k_I, as constants 2 and 0.7, respectively.

The IMUs we use are low-cost MEMS, each of them costing less than 5 USD. We do not calibrate them before they were installed into the test environment, because calibration of the IMUs in a lab is usually expensive. One of the main aims of this work is to pursue decreasing costs for hardware.

We remove the forward kinematic model that requires a data flow between consecutive joints. The angle estimation of a joint only uses the measurement of IMUs on the two links that form the joint, and that allows us to decouple the pose estimation of a robotic arm from the motion of its platform base, resulting in floating base estimation.

We usually consider the outputs of low-cost IMUs to have a bigger bias or drift than high-quality ones. By adding simulated disturbances to the raw data measured from the practice test, we can check the performance of the algorithm with some sensors that have worse bias or drift than the sensors used in the test. For example, a simulated extra bias of accelerometers, as described in (22), can be added to one of the IMUs' measurements in the test which Fig. 5

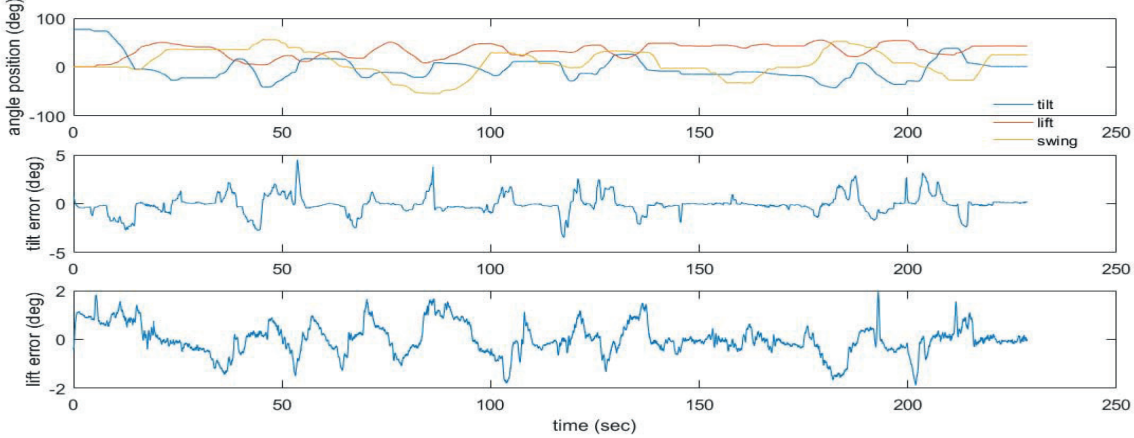

Fig. 5. The top figure shows the angle positions of the three joints; the middle one is the error of estimation for the tilt joint, and the bottom is the estimation error of the lift angle.

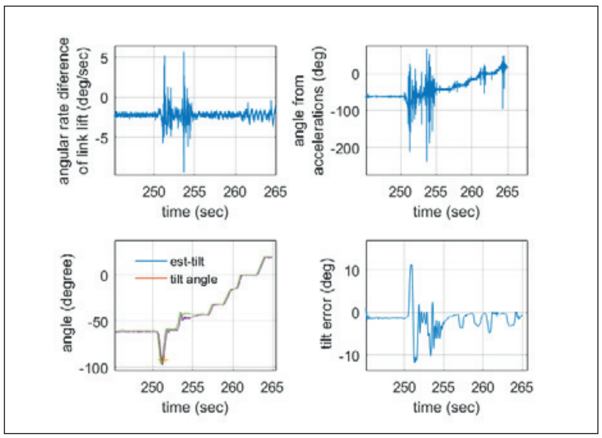

Fig. 6. Oscillation of the link itself introduces an estimation error.

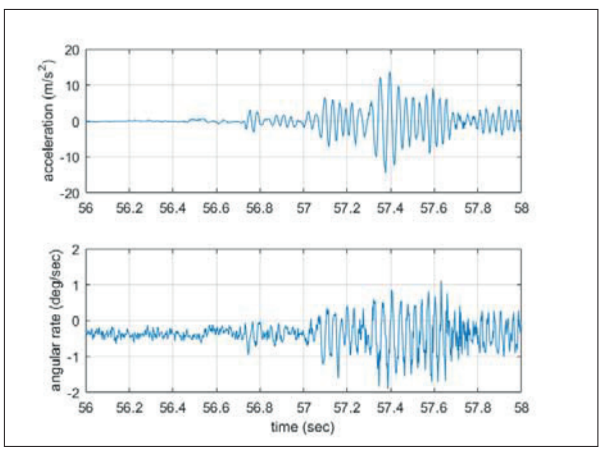

Fig. 7. Disturbances introduced to IMU by the vehicle engine.

is generated from. The selected IMU is close to lift joint, and attached to the lift link.

$$\begin{cases} \Delta x = 0.3 + 0.3sin(0.06\pi t + 0.3\pi) \\ \Delta y = 0.4 + 0.4sin(0.08\pi t + 0.4\pi) \\ \Delta z = 0.5 + 0.5sin(0.12\pi t + 0.5\pi) \end{cases} \tag{22}$$

where Δx, Δy, and Δz are the simulated disturbances added to the raw data; t is the simulation time. The variation of

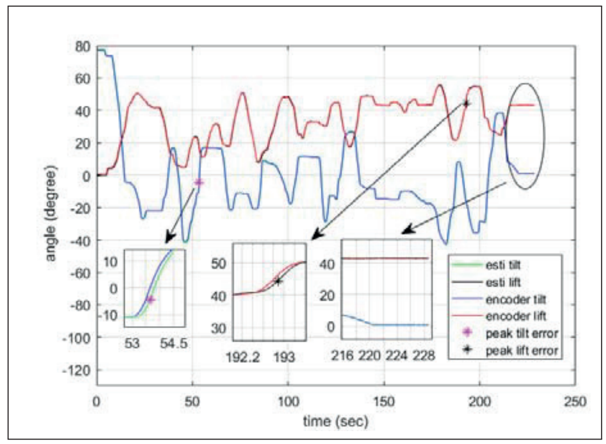

Fig. 8. The output of estimation results for tilt and lift angle, with the enlarged local regions.

these disturbances in (22) is much bigger than that of the accelerometers' bias in this work. The EKF in the proposed algorithm is used to estimate the specific force in the center of the tilt joint, with the extra bias added to the IMU and without it. The difference of this specific force is shown in Fig. 9.

From Fig. 9, we notice that the force's difference has the same frequency and phase as defined by (22), but the amplitude and mean values shrink to about 25% of it. If we add similar simulated accelerometer bias to each axis of each IMU on the lift link, this difference of specific force has the same shape as the sum of the extra bias added to each axis of each accelerometer, but amplitude decreases by about 75%. (7) and the process model of the proposed EKF have linear form and should thus hold the property of linear superposition.

There exist inaccuracies in the installation of IMUs: the orientation errors of the IMUs are about 1 or 2 degrees, and the coordinate errors are about 1 or 2 cm. In addition, the hydraulic manipulator might not move in an exact plane, and the triad-axes of the accelerometers are misaligned because we use low-cost IMUs. So, except for the measurement noise

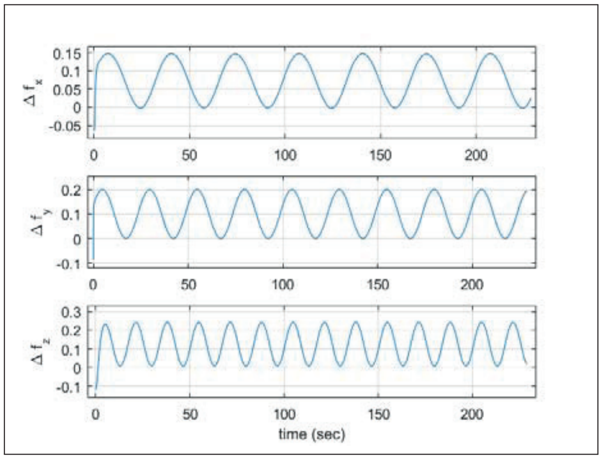

Fig. 9. Difference of specific force in the tilt joint center.

and the bias of the IMUs' measurements, other errors are also introduced. We use the state of the accelerometers' bias, b_a, to absorb all these errors.

Similarly, we could add disturbances to the angular rate for observation of the EKF: if we set the amplitude up to 5 $\frac{deg}{s}$ in each direction, the differences of the estimation for specific force in the joint centers is smaller than one order of magnitude compared to the noise of the forces. This means it has little effect in the output of angle calculation with (4), even if the drift of the gyroscope cannot be estimated well by the EKF. Thus, we can set the covariance of the gyroscope's noise smaller than specified and eliminate the drift or bias for the gyroscopes in CF.

Although we specifically validate the algorithm in a heavy-duty mobile machine, it can also apply for the angle estimation of links on other robotics arm which has 1-DOF joint. And the rotation plane of their joints should not be parallel to the ground, since we use gravity as reference.

VI. CONCLUSIONS

The proposed algorithm uses the measurements of four three-axis accelerometers mounted on each manipulator link to calculate the specific force at the coordinate's origin. These estimates are then fused with the angular rate from an EKF by utilizing a complementary filter to obtain the desired joint angle estimate. The novelty of the developed algorithm is that the use of a forward kinematic model requiring data flow between consecutive joints is not needed. Algorithm is validated with a heavy duty working machine that has a base that is in 6-DOF floating base motion. Even with very low-cost IMUs (costing less than 5 USD each), without any IMU precalibration and with the base of the manipulator moving over complex terrain, the accuracy of the joints' angle estimation is better than 1 degree (RMS), which is the same order of magnitude than in studies utilizing high-cost IMUs [3]. As a next step, we plan to try to estimate the relative rotation angle between the platform base and the manipulator in situations where the base is not parallel to the ground or is in non-uniform motion.

REFERENCES

[1] K. Gribbins. (2016) The ultimate 2016 compact excavator market watch. Accessed: 15.9.2017. [Online]. Available: http://compactequip.com/excavators/the-2016-compact-excavator-market-watch/

[2] International Federation of Robotics (IFR). Executive summary world robotics 2016 industrial robots. Accessed: 15.9.2017. [Online]. Available: https://ifr.org/img/uploads/Executive_Summary_WR_Industrial_Robots_20161.pdf

[3] J. Mattila, J. Koivumki, D. G. Caldwell, and C. Semini, "A survey on control of hydraulic robotic manipulators with projection to future trends," *IEEE/ASME Transactions on Mechatronics*, vol. 22, no. 2, pp. 669–680, April 2017.

[4] J. Koivumäki, J. Honkakorpi, J. Vihonen, and J. Mattila, "Hydraulic manipulator virtual decomposition control with performance analysis using low-cost MEMS sensors," in *Advanced Intelligent Mechatronics (AIM), 2014 IEEE/ASME International Conference on*. IEEE, 2014, pp. 910–917.

[5] J. Vihonen, J. Honkakorpi, J. Tuominen, J. Mattila, and A. Visa, "Linear accelerometers and rate gyros for rotary joint angle estimation of heavy-duty mobile manipulators using forward kinematic modeling," *IEEE/ASME Transactions on Mechatronics*, vol. 21, no. 3, pp. 1765–1774, jun 2016.

[6] J. Vihonen, J. Mattila, and A. Visa, "Joint-space kinematic model for gravity-referenced joint angel estimation of heavy-duty manipulators," in *IEEE Transactions on Instrumentation and Measurement*. IEEE, 2017 [Accepted].

[7] X. Xinjilefu, S. Feng, and C. G. Atkeson, "A distributed MEMS gyro network for joint velocity estimation," in *Robotics and Automation (ICRA), 2016 IEEE International Conference on*. IEEE, 2016, pp. 1879–1884.

[8] N. Rotella, S. Mason, S. Schaal, and L. Righetti, "Inertial sensor-based humanoid joint state estimation," in *Robotics and Automation (ICRA), 2016 IEEE International Conference on*. IEEE, 2016, pp. 1825–1831.

[9] Y. Tao, H. Hu, and H. Zhou, "Integration of Vision and Inertial Sensors for 3D Arm Motion Tracking in Home-based Rehabilitation," *The International Journal of Robotics Research*, vol. 26, no. 6, pp. 607–624, 2007. [Online]. Available: http://dx.doi.org/10.1177/0278364907079278

[10] A. M. Sabatini, "Quaternion-based Extended Kalman Filter for determining orientation by inertial and magnetic sensing," *IEEE Transactions on Biomedical Engineering*, vol. 53, no. 7, pp. 1346–1356, July 2006.

[11] J. A. Corrales, F. A. Candelas, and F. Torres, "Hybrid tracking of human operators using IMU/UWB data fusion by a Kalman filter," in *2008 3rd ACM/IEEE International Conference on Human-Robot Interaction (HRI)*, March 2008, pp. 193–200.

[12] X. Zhang, E. Peltola, and J. Mattila, "Joint angle estimation for floating base robots utilizing MEMS IMUs," in *8th Conference on Robotics, Automation and Mechatronics (RAM), 2017 IEEE International Conference on*. IEEE, 2017 [Accepted].

[13] L. Sciavicco and B. Siciliano, *Modelling and control of robot manipulators*. Springer Science & Business Media, 2012.

[14] T. Williams, A. Pahadia, M. Petovello, and G. Lachapelle, "Using an accelerometer configuration to improve the performance of a MEMS IMU: Feasibility study with a pedestrian navigation application," in *ION GNSS*, 2009.

[15] S. Park, C.-W. Tan, and J. Park, "A scheme for improving the performance of a gyroscope-free inertial measurement unit," *Sensors and Actuators A: Physical*, vol. 121, no. 2, pp. 410–420, 2005.

[16] M. Perlmutter and S. Breit, "The future of the MEMS inertial sensor performance, design and manufacturing," in *2016 DGON Intertial Sensors and Systems (ISS)*, sep 2016, pp. 1–12.

[17] F. Khoshnoud and C. W. de Silva, "Recent advances in MEMS sensor technology-mechanical applications," *IEEE Instrumentation Measurement Magazine*, vol. 15, no. 2, pp. 14–24, apr 2012.

[18] A. Purwar, D. U. Jeong, and W. Y. Chung, "Activity monitoring from real-time triaxial accelerometer data using sensor network," in *2007 International Conference on Control, Automation and Systems*, oct 2007, pp. 2402–2406.

PUBLICATION III

Mobile robotic spatial odometry by low-cost imus

Xiaolong Zhang, Teemu Mononen, Jouni Mattila, and Mohammad M Aref

DOI: 10.1109/MESA.2018.8449209

Mobile Robotic Spatial Odometry by Low-Cost IMUs

Xiaolong Zhang
Automation and Hydraulic Engineering
Tampere University of Technology
Tampere, Finland
xiaolong.zhang@tut.fi

Teemu Mononen
Automation and Hydraulic Engineering
Tampere University of Technology
Tampere, Finland
teemu.mononen@tut.fi

Mohammad M. Aref
Automation and Hydraulic Engineering
Tampere University of Technology
Tampere, Finland
m.aref@ieee.org

Jouni Mattila
Automation and Hydraulic Engineering
Tampere University of Technology
Tampere, Finland
jouni.mattila@tut.fi

***Abstract*—This paper shows the use of microelectromechanical system (MEMS) low-cost inertial measurement units (IMUs) to realize absolute odometry information for a mobile vehicle or field robotics, by providing the rotation angle of a wheel and its suspensions with respect to gravity. In addition, with the proposed algorithm we calculate the yaw and roll angle information for the bogie by integrating the output of the rotation gyroscope, which decreases the angle drift considerably. A test bed was set up to validate the algorithm, and the results are analyzed in detail.**

***Keywords*—MEMS, IMU, EKF, AFS, mobile robotics**

I. Introduction

In mobile robotics, it is a common practice to attach a localization sensor system to the robot body to measure the robot's pose and sometimes fuse this information with dead reckoning of the robot's wheel odometry. However, this method might not be a suitable approximation of an articulated frame steerable (AFS) mobile robot even on a flat and balanced driving surface. It becomes even worse in rough terrain motions. Pure rolling assumptions, on which nonholonomic dynamic constraints are built [1], cannot be valid without measuring and estimating the robot's internal dynamic parameters. For instance, it is impossible to assume zero side slippage of the wheels for an AFS mobile robot even inside a simple configuration space, and appropriate measurements for the wheels are necessary.

Therefore, even if we temporarily neglect environmental effects, the velocities of the rear and front parts cannot be independent variables for measurements, and at the same time, each alone cannot express the vehicle's status, as shown in Fig. 1.

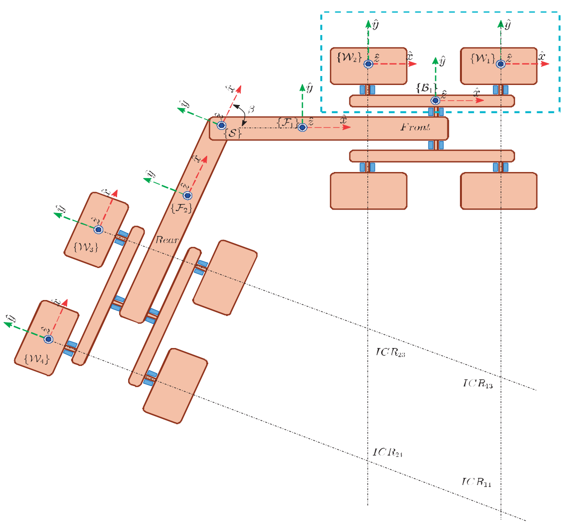

Fig. 1. Top view of the base for one type of heavy-duty mobile machine.

Fig. 2. Wheels and bogie of a forest vehicle. The size and dimensions are shown in millimeters.

Based on this, it is clear that the installation of an inertial measurement unit (IMU), or localization with simple dead-reckoning methods, is not enough to determine the robot's status.

For solving this problem, and the tradeoff between system cost and complexity, we propose installing one strap-down microelectromechanical system (MEMS) IMU on the rotation center for each wheel and on each bogie. With gravity as a reference, we propose using an extended Kalman filter (EKF) to fuse the measurements of the accelerometers and the measurements of the gyroscopes to estimate the pitch angle of the bogie and the rotation angle of the wheel.

As the wheel of a vehicle is a natural rotation platform, a triad rotation gyroscope with a constant rotation speed along one axis can form a virtual gyroscope which can decrease the gyro's drift except the rotation axis [3], [4]. We use this property to calculate the yaw and roll angles for the bogies when the wheel of the vehicle has a constant angular rate or the change in the rotation speed is small.

In this study, we simplified the test bed as one bogie-wheel pair; the prototype is shown in Fig. 3. This test bed imitates the bogie-wheel configuration of the forestry machine presented in Fig. 2.

II. THEORETICAL BACKGROUND

In Fig. 3, two IMUs with triad accelerometers and triad gyroscopes are installed on the test bed. One is attached on the bogie, and the other is on the rotation center of the wheel. The bogie has 1 degree of freedom (DOF) to the test bed, and the bogie can move up and down with a range about 20 degrees. The base of the test bed is stationary. We define the axis $\hat{z}_L$ to align with gravity and the positive direction toward the up direction. All the frames in Fig. 3 share the same y direction, outward. The angle of the bogie is the angle difference between the body fixed frame of the bogie and the test bed, and the angle of the wheel rotation is the angle difference between the sensor frame and the body fixed frame of the bogie. The rotation positive direction of the bogie and the wheel is counter-clockwise. To measure these two angles in a two-dimensional (2D) frame, we chose the EKF.

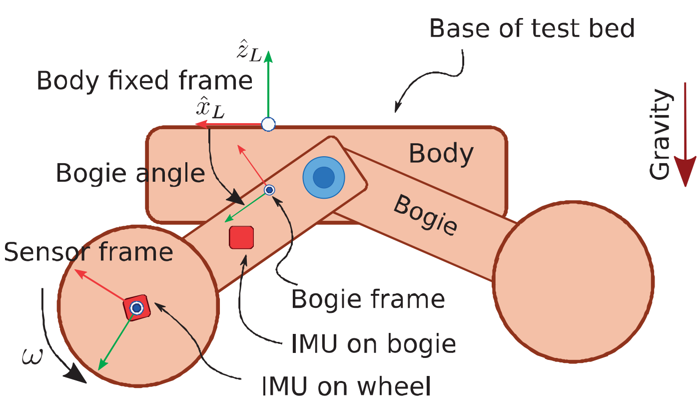

Fig. 3. Schematics of the test bed containing IMUs strapped on the bogie and the rotating wheel. The bogie moves using an electric motor at its center.

A. EKF for Pitch Angle Estimation

$\theta[k]$ is the angle in time step k, $\dot{\theta}$ is the angular velocity, b_g is the bias of the angular velocity, and the state of the EKF is

$$x[k] = \begin{bmatrix} \theta[k] \\ \dot{\theta}[k] \\ b_g[k] \end{bmatrix}. \tag{1}$$

The discrete process model is

$$x[k+1] = Ax[k] + w[k], \tag{2}$$

where the state transition matrix is

$$A = \begin{bmatrix} 1 & T & 0 \\ 0 & 1 & 0 \\ 0 & 0 & 1 \end{bmatrix}. \tag{3}$$

T is the sampling interval. The process noise is

$$w[k] = T \begin{bmatrix} n_{\omega,k} \\ n_{\alpha,k} \\ \eta_{b_a} \end{bmatrix}. \tag{4}$$

$n_{\omega,k}$, $n_{\alpha,k}$, and η_{b_a} are Gaussian noise.

Assuming the noises are not correlated, the matrix of process noise is

$$Q = E(ww^T) = T^2 \begin{bmatrix} \sigma_\omega^2 & 0 & 0 \\ 0 & \sigma_a^2 & 0 \\ 0 & 0 & \sigma_{ba}^2 \end{bmatrix}. \tag{5}$$

We use three of the IMU outputs as observations, measurements of the accelerometer in the x and z directions and measurement of the gyro in the y direction. We take the gravity as the reference for the pitch angle estimation.

The observation model is

$$h = \begin{bmatrix} 9.81\cos\theta + az \\ -9.81\sin\theta + ax \\ \dot{\theta} + b_g \end{bmatrix} + \begin{bmatrix} n_z \\ n_x \\ n_\theta \end{bmatrix}. \tag{6}$$

n_z, n_x, and n_θ are Gaussian noise. az and ax represent the motion acceleration in the z and x directions of the sensor frame. Please notice we assume that gravity mainly projects into the x-z plane of the sensor frame. Taking az and ax as the noise vector, then the observation matrix is

$$H_k = \begin{bmatrix} -9.81\sin\theta_k & 0 & 0 \\ 9.81\cos\theta_k & 0 & 0 \\ 0 & 1 & 1 \end{bmatrix} . \tag{7}$$

Please notice we can get the roll angle, θ_{roll_b}, from Section II B, and the acceleration in the x-z plane is

$$a_{xz} = 9.81\cos\left|\theta_{roll_b}\right| . \tag{8}$$

However, currently the test bed cannot provide the roll rotation; therefore, we use $9.81\mathrm{m/s}^2$ in (6) and (7).

B. *Calculation of the Yaw and Roll Angles with a Rotation Gyroscope*

In Fig. 1, we denote the measurements of the gyro on the wheel as w_x and w_z, on the x and z axes, respectively. They can be written as true angular rates plus long-term bias and noise:

$$w_x = w_{xt} + b_x + n_x , \tag{9}$$

$$w_z = w_{zt} + b_z + n_z . \tag{10}$$

Ignoring the noise terms, we transfer these two outputs into the body fixed frame of the bogie and integrate them with time to get the yaw and roll angles of the bogie:

$$\theta_{yaw_b} = \int_0^{t_{end}} [(w_{x_t} + b_x)\cos\emptyset - (w_{z_t} + b_z)\sin\emptyset]dt, \tag{11}$$

$$\theta_{roll_b} = \int_0^{t_{end}} [(w_{z_t} + b_z)\cos\emptyset_k + (w_{x_t} + b_x)\sin\emptyset_k]dt. \tag{12}$$

Where $\emptyset_k$ is the rotation angle of the wheel, it is the difference between the sensor frame with respect to the gravity expressed in the inertial frame, and

$$\emptyset_k = \int_0^{t_k} r\, dt . \tag{13}$$

In (13), r is the rotation speed of the wheel. If we assume r is constant, and we combine (11) and (12), we notice that the integration term that contains the long-term bias part will disappear after one complete circle.

We can estimate the angle of the bogie and the angle of the wheel with respect to the test bed frame or gravity and then get the angle of $\emptyset_k$. The whole solution is based on a pure IMU; no external information is needed.

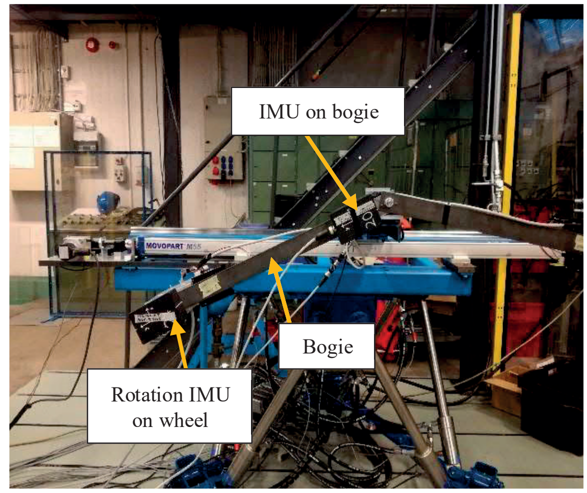

Fig. 4. A photograph of the test bed.

III. Test Environment and Results

A. *Test Environment*

The test bed shown in Fig. 4 contains two separate measurement units. One BMI160 IMU sensor is wrapped in a box with a wireless communication function and mounted on a rotating joint at the tip of the bogie. The joint can be rotated by an electric motor to simulate the wheel's rotation. A second IMU (the same type as the first) is attached close to the joint of the bogie and the base of the test bed. The joint also has a motor to control the joint rotation to simulate the bogie's pitch angle fluctuations. The two rotational joints have incremental encoders to provide the angle information as a sound reference for the angle estimation. The sensor units send data to a dSpace MicroAutoBox to acquire data in real time and to control the motors; the sampling time is 400 Hz.

B. *Pitch Angle of the Bogie*

The test sequence lasts about 12 min. For the first minute, the IMUs and the bogie are kept stationary. From the second minute, the rotation IMU starts to rotate at a constant speed of 170 degrees per second. The bogie starts moving, and for the motion of oscillation from 3 mins to the end of the test, the amplitude is about 8 degrees, and the period is 20 s, to simulate the vehicle's motion on uneven ground. The results from this test are shown in Fig. 5 and Fig. 6. In this test, the root mean square error of the motion estimation for the bogie was 0.6727 degrees.

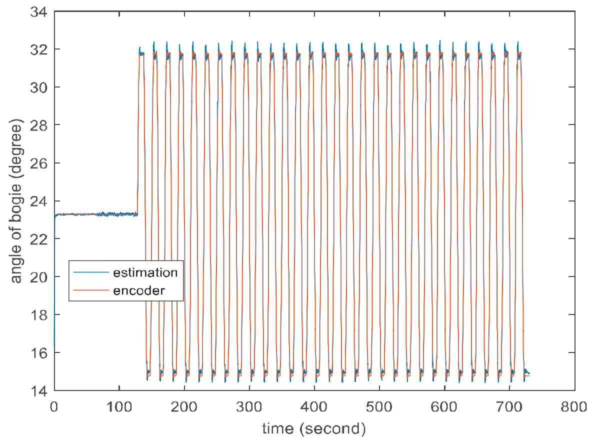

Fig. 5. The bogie motion and estimation results for the test described in III B. The red line is from the encoder, and the blue line is the estimated output from the EKF.

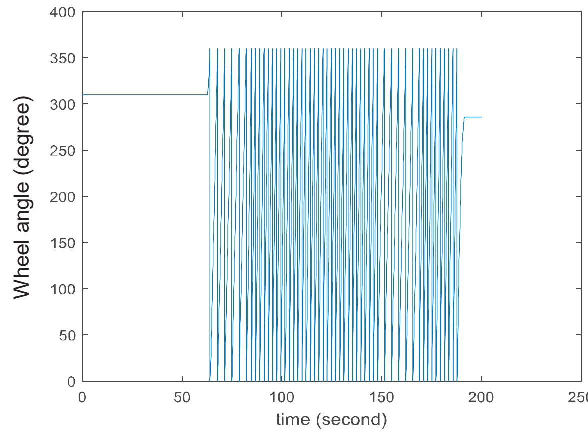

Fig. 7. Wheel rotation test with the bogie kept stationary. For the first minute, the wheel is kept stationary, and then the rotation begins at a speed of 100 °/s for about 20 s, then 170 °/s for about 40 s, then 100 °/s for another 20 s, and then 170 °/s for the last 20 s.

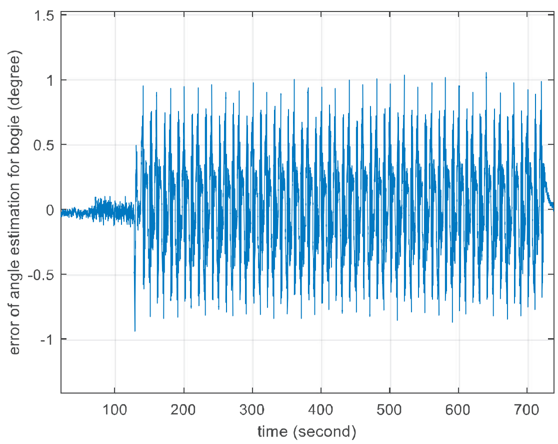

Fig. 6. The error of the bogie's motion from estimation in the test scenario described by Fig. 5.

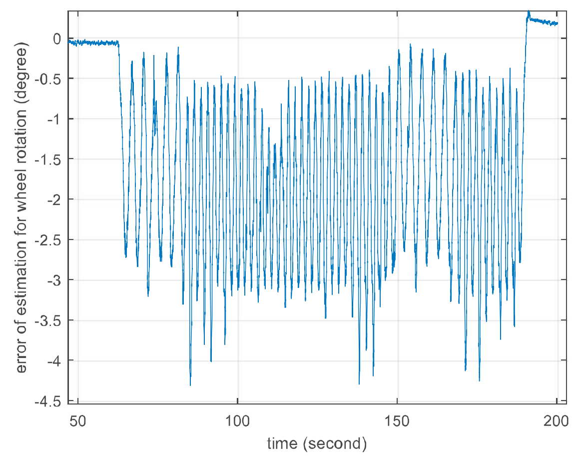

Fig. 8. The error for the wheel rotation test of Fig. 7.

C. Rotation Angle of the Wheel

To test the algorithm's efficacy, the wheel rotation angle is estimated in a test, where the wheel is rotated at varying speeds while the bogie is kept stationary. The wheel rotation is presented in Fig. 7, and the estimation error in Fig. 8. Another test was conducted with both the wheel and the bogie in motion. The resulting wheel rotation estimation error is presented in Fig. 9. In the latter test, the root mean square error of the wheel rotation estimation was 1.886 degrees.

D. Calculation of the Yaw and Roll Angles of the Bogie

To compute the yaw and roll angles of the bogie, the test process is the same as described in section III B, but the measure degrees per second integrates the yaw and roll angles of the wheel. As the test bed has no yaw and roll motion, we simply use zero as the reference, to validate the idea that the rotation gyroscope can decrease the drift of the angle integration in the other two axes except the rotation axis.

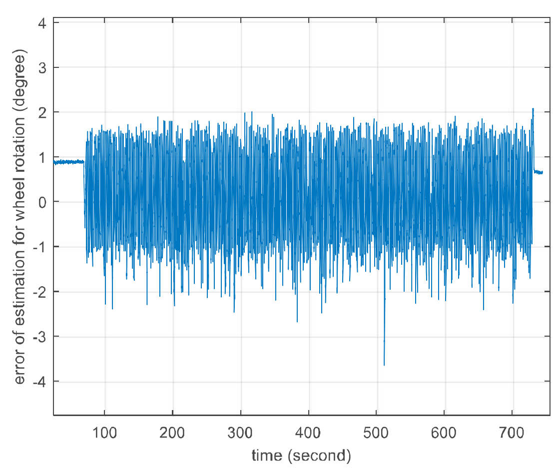

Fig. 9. Error of wheel rotation estimation in a test where both the wheel and the bogie are in motion. The bogie starts oscillating as in Fig. 5, and the wheel rotates at a speed of 100 °/s after 60 s.

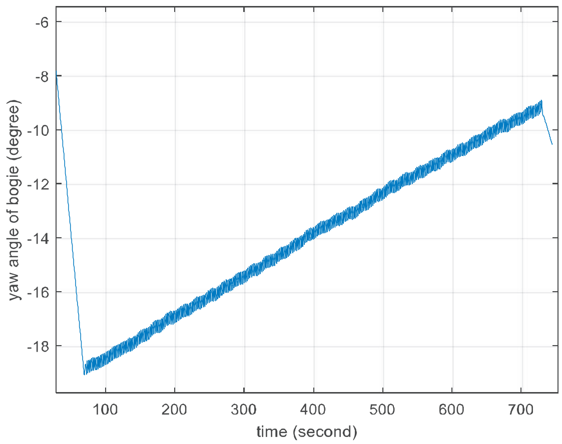

Fig. 10. The yaw angle of the bogie.

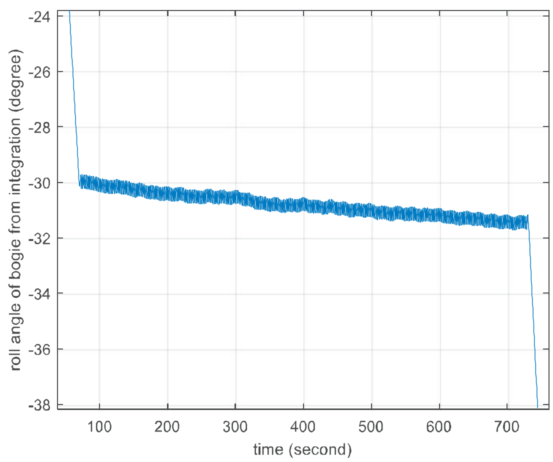

Fig. 11. The roll angle of the bogie.

The values of the yaw and roll angles are shown in Fig. 10 and Fig. 11, respectively. When the wheel has no rotation during the first minute, the angles drift considerably, because we use low-cost IMUs. Once the wheel starts rotating, most of the long-term bias in the gyro's x and y-axes has been eliminated, and the drift of the yaw and roll angles become much smaller.

Please notice that the wheel has a rotation speed of 170°/s with respect to the body fixed frame of the bogie after about 65 s. However, after about 125 s, the bogie starts oscillating, and this oscillation introduces extra velocity to the wheel with respect to the inertial frame, violating the assumption in (13) that the wheel maintains a constant rotation speed. As the bogie's maximum angular speed is less than 12 °/s, one less order than the wheel's, the error introduced by this speed change in the rotation is not large but is still observed in Fig. 10 and Fig. 11 after 125 s.

In Fig. 12 and (11) and (12), we notice that the integration angle for the yaw and the roll should be some sinusoid, and the amplitude depends on the long-term bias in the gyroscope on the x- and z-

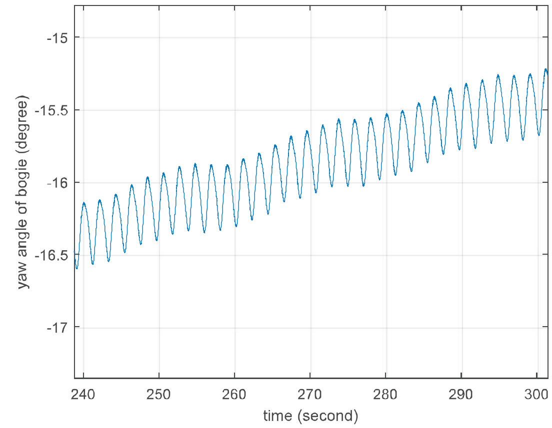

Fig. 12. An enlarged part of Fig. 10 to showcase the signal behavior.

axes. In section IV A, we show after we deduce this long-term bias from the raw data from the gyro that the amplitude of this sinusoid wave decreased.

IV. Discussion

A. Error Correction

In [4] and [5], a method for calibrating MEMS IMUs is given. For our implementation, if the IMU rotates around the y-axis, ignoring the Earth rotation, a simple error model for the gyro is

$$\begin{bmatrix}\delta\omega_x\\ \delta\omega_y\\ \delta\omega_z\end{bmatrix}=\begin{bmatrix}k_{xy}\omega+d_x\\ S_y\omega+d_y\\ k_{zy}\omega+d_z\end{bmatrix}, \tag{14}$$

Where d_x, d_y, and d_z are the gyro biases in the sensor frame, and $[\delta\omega_x \quad \delta\omega_y \quad \delta\omega_z]^T$ is the error of the gyro in the sensor frame. k_{xy} is the factor of the installation error for the x-axis in relation to the y-axis, which means if the y-axis has a rotation speed of ω, because of the installation inaccuracy, it will project into the x-axis an angular speed with the factor. k_{zy} is the factor of the installation error for the z-axis in relation to the y-axis. S_y is the scale factor in the y-axis, indicating the nonlinearity of the gyro in this axis, and ω is the rotation speed of the y-axis. As we can use gravity as a reference to correct the error of the gyro in the y-axis, as shown in sections III B and C, we do not discuss the S_y and d_y here.

For the test in section III B, in the first 65 s the system is stationary. We take the mean values of the first 5 s from the gyro's raw output in the x- and z-axes, compare it with zero, and get the bias d_x, and d_y. From 65 s to 125 s of the test, only the wheel has a rotation with a speed of 170 degree/s, and we take the mean value of the gyro's output in the other two axes during this period as $\delta\omega_x$ and $\delta\omega_z$, with the bias d_x, and d_y from the first 5 s period.

Using (14), we get k_{xy} and k_{zy}. In each time step k, we use (15) and (16) to give the gyro error in the x- and z-axes:

$$\delta\omega_x[k] = k_{xy}\omega_{est}[k] + d_x \,, \tag{15}$$

$$\delta\omega_z[k] = k_{zy}\omega_{est}[k] + d_z \,. \tag{16}$$

$\omega_{est}[k]$ is the estimated rotation speed in the y-axis. After we correct the gyro error given by (15) and (16), we apply (11) and (12) to get the yaw and roll angles again. The results are shown in Fig. 13.

Fig. 13 shows that with the correction for the gyro on the x- and z-axes in the sensor, the drift in the yaw and roll angle calculations decreased. A comparison to Fig. 10 and Fig. 11 shows that for about 11 min the yaw angle drift reduces from about 10 degrees to 5 degrees, and the roll angle from 2 degrees to about 1 degree. As the estimation is inaccurate for the rotation angle of the wheel, if the bias or error is in the gyro's x- and z-axes, it cannot be eliminated completely and will accumulate as the integration continues. Additionally, the amplitude of this sinusoid wave is shortened to 0.07 degree in Fig. 13; in Fig. 12, the amplitude is about 0.4 degree before the correction.

B. Gyro Error within a Short Period

In Fig. 14, the blue part indicates the raw output of the gyro's x-axis when the wheel rotates around the y-axis at a speed of 170 °/s, and the red line is the rotation phase of the wheel divided by 360 for convenience. The output of the gyro in the x-axis has a short-term bias or error as the gyro rotates in the gravity field. This means that for the low-cost IMUs we use in the test, the gyro's output correlates with the acceleration. This short-term bias cannot be eliminated with (11) and (12) when the yaw and roll angles are integrated. Our next step is to try to estimate this bias with the EKF.

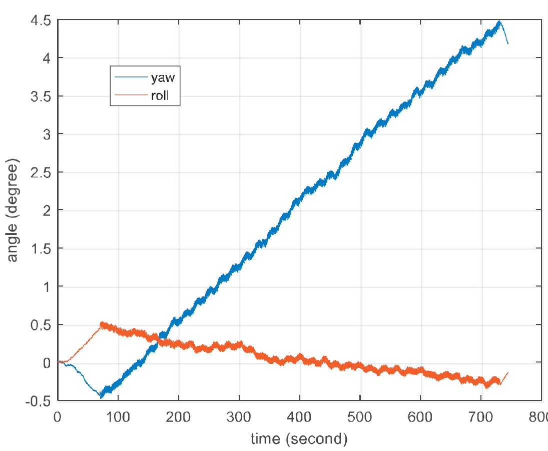

Fig. 13. After the correction of error for gyro on the x- and z-axes, the drift in the integration of yaw and roll angle became smaller.

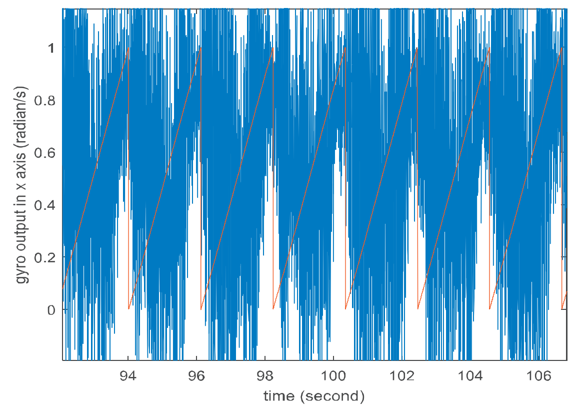

Fig. 14. The raw wheel-installed, x-axis gyroscope data (blue) and the wheel rotation phase from the encoder (red) normalized between 0 and 1.

V. Conclusion

In this paper, we used only low-cost IMUs to build an odometer for field robotics, for the purpose of control or localization. The method is verified experimentally on the test setup that has encoders to obtain ground truth. The maximum rotation angle estimation error for the wheel is within 5 degrees for the experiments. This odometer can also provide useful angle information for the yaw and roll angles for several minutes. In addition to the wheel odometer information provided based on the proposed estimation method, the calculation of the body roll and yaw is a key benefit. Calculating these angles provides the control system of such platforms with a more realistic estimation of the robot's status. This information is more important for platforms with complicated internal dynamics, such as off-road vehicles in field robotics where the suspensions (active or passive) can bring more degrees of freedom, and therefore, more complexity in the platforms' motion model.

Acknowledgment

This research work was supported in part by the Doctoral School of Industry Innovations (DSII), by Tampere University of Technology (TUT), the Forum for Intelligent Machines (FIMA), and the Academy of Finland (Grant no. 294915).

References

[1] M. Aref, Mohammad, R. Ghabcheloo, and Jouni Mattila, "A macro-micro controller for pallet picking by an articulated-frame-steering hydraulic mobile machine," in IEEE Int. Conf. Robotics Auto. (ICRA), 2014, pp. 6816–6822.

[2] J. Vihonen, J. Mattila, and A. Visa, "Joint-space kinematic model for gravity-referenced joint angle estimation of heavy-duty manipulators," IEEE Trans. Instrum. Meas., vol. 66, pp. 3280–3288, Dec. 2017.

[3] J. Collin, "MEMS IMU carouseling for ground vehicles," IEEE Trans. Veh. Technol., vol. 64, pp. 2242–2251, 2015.

[4] S. Du, "Rotary inertial navigation system with a low-cost MEMS IMU and its integration with GNSS," Ph.D. dissertation, Univ. Calgary, 2015.

[5] S. Du, W. Sun, and Y. Gao, "MEMS IMU error mitigation using rotation modulation technique," Sensors, vol. 16, p. 2017, Nov.

PUBLICATION
IV

3D Attitude Calculation for the Grasper of a Crane System with a Rotary Gyroscope

Xiaolong Zhang, Pauli Mustalahti, Eelis Peltola, and Jouni Mattila

DOI: 10.1109/ICICIP.2018.8606668

Ninth International Conference on Intelligent Control and Information Processing
November 9-11, 2018; Wanzhou, China

3D Attitude Calculation for the Grasper of a Crane System with a Rotary Gyroscope

Xiaolong Zhang, Pauli Mustalahti, Eelis Peltola and Jouni Mattila
Depatment of Automation and Hydraulic Engineering, Tampere University of Technology,
Tampere, Finland
Emails: {xiaolong.zhang, pauli.mustalahti, eelis.peltola, jouni.mattila}@tut.fi

***Abstract*——This paper focuses on attitude calculation for a grasper, which hangs on a heavy-duty machine with rope or links at the boom tip, using a triad-axis rotary gyroscope attached on the grasper. The aim of the attitude calculation is to provide anti-sway control. We try to decrease the drift of the gyroscope in two directions, except the rotation axis. The algorithm was validated on a test bed, which is based on a crane system. The test results show that with a rotary platform, long-term drift of the gyro decreased and the accuracy of angle integration for the grasper became better.**

Keywords—IMU, quaternion, anti-sway, crane.

I. INTRODUCTION

Crane systems are widely used to move loads in factories, forests, construction fields, etc. These systems have a grasper connected to the tip of their manipulator with links or cables, making the grasper not controllable directly since the acceleration from operating the crane and external disturbances move the grasper. To ensure the system's safety and to increase operating efficiency, an anti-sway controller is applied to these cranes to restrict unwanted swaying of the grasper, such as in [1]-[3].

In [1] and [2], the crane grasper swaying is constrained to vertical plane motions, and the sway angle is measured with accuracy sensors directly. [3] presents a grasper rotated around two axes. The hydraulic manipulator has 4 degrees of freedom (DOF), and the state of sway estimation uses two Inertial Measurement Units (IMU), based on an Extended Kalman Filter (EKF) presented in [4].

[4] applied a dynamic model of a grasper system, which hung with multiple links from the boom tip, for fusing the outputs from an accelerometer and gyroscope measuring its sway angle. However, the amplitude of the sway angle in their implementation is relatively small, less than 7 degrees.

In this paper, we develop a measurement approach for a grasper with a rotary gyroscope to be used for anti-sway control. In [5], a rotary IMU is mounted on the wheel of a vehicle and an EKF is applied for fusing the measurements from the IMU's gyroscope and accelerometer together to correct the drift of angular velocity in the rotation axis. A rotary IMU benefits from being easily mountable onto a complete system, unlike encoders.

In [6] and [7] kinematic model-base algorithm developed, and complementary filter (CF) applied for fuse the measurements from accelerometers and gyroscopes, and gravity is an aiding reference.

Contrary to [5]-[7], in this paper, we do not use a model and filter, because in our case the dynamic or kinematic model for a filter is difficult to build. The grasper has three DOF for rotation; the rotation joints experience friction forces and the boom's manipulation frequently adds disturbing acceleration to the grasper. In practical operation, the grasper will hold all kinds of loads with different shapes, which lead to the center of mass changing. In addition, there are other external forces such as wind; the load may collide with other objects, etc. A dynamic model would have to take all of these into account. In addition, kinematic model needs us deploy sensors on each links, this significant improve the complexity of the system.

We use a triad-axis gyroscope attached to the grasper through a rotary platform. With the rotary gyroscope, measure the angular velocity and integrate the rotation angle of the grasper. The gyroscope rotates with a constant speed respect to the body-fixed frame of the grasper. The gyroscope has less effect with eternal force disturbances, and it is also considered as a reliable sensor in most environments. However, it is well known that the drift of a gyroscope causes the error of angle integration to increase. Even for a high performance, industry-grade gyroscope, the error of angle integration will diverge rapidly without correction by another sensor or frequent calibration.

A rotary gyroscope can decrease the drift of measured angular velocity in any axis except the rotation axis [8], [9]. The test results show that our approach is promising, within two minutes the error of the integration for sway angles smaller than 2 degrees.

II. EXPERIMENTAL SETUP

We built the test bed based on a HIAB XS033 crane, as presented in Fig. 1. The hydraulic manipulator has three links and a reach of about 5.3 meters. The lift and tilt joints can rotate in the vertical plane, while the locked base joint has no rotation.

Fig. 2 shows the rotation platform attached to the grasper, with the IMU in box rotated by an electric motor; the angular velocity controlled to 250º/s respect by motor controller. Position and velocity references for the rotation of IMU-sensor provide by encoder.

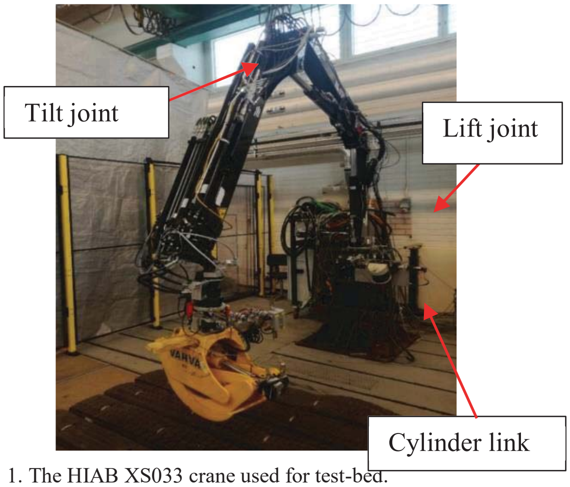

Fig. 1. The HIAB XS033 crane used for test-bed.

The joints and links, which connect the grasper with the boom tip, are shown in Fig. 3. Position references for the three unactuated joints are also given by encoders.

A CAN-bus connects the sensors to dSpace, and dSpace runs the Simulink model collecting sample data with a rate of 500 Hz/s. The results in this paper were calculated offline with Matlab.

The hardware in the tests summary below:

- PowerPC-based dSpace ds1103 with a sample time of 2 ms
- SICK DFS60B incremental encoder (10000 inc/rev) for the IMU rotation
- Fraba incremental encoders (16384 inc/rev) for the joint 1 and joint 2 angles
- Heidenhain ROD 426 incremental encoder (5000 inc/rev) for the joint 3 angle
- Gripper tool with a mass of 90 kg
- Maxon M110743 motor for rotating the IMU, controlled by an EPOS2 motor controller
- ADIS16485 iSensor MEMS inertial unit by Analog Devices with three-axis angular gyroscope (±450°/s) and three-axis accelerometer (±5g)

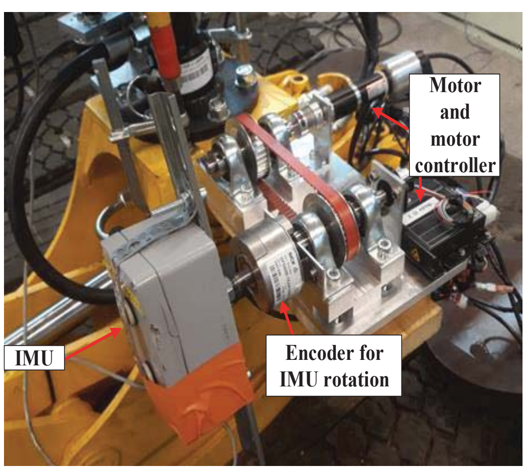

Fig. 2. IMU box and its rotation platform.

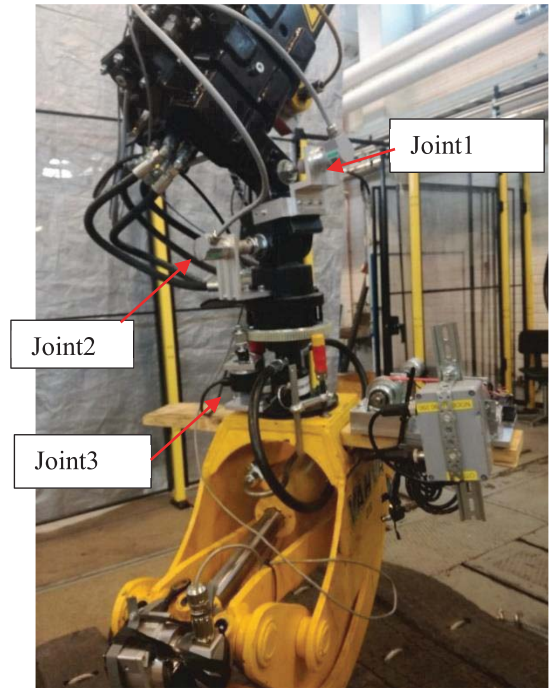

Fig. 3. The unactuated joints and links of grasper.

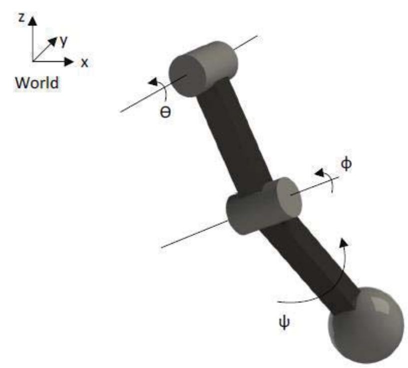

Fig. 4. Model of the system.

The IMU in the test bed contains accelerometer; however, our algorithm only uses the gyroscope output.

The grasper system, shown in Fig. 3, may be simplified as a model presented in Fig. 4. The reference of pitch angle Θ in the world frame can attained by combining the output of the encoders of joint 1, the lift joint and tilt joint. The encoder in joint 2 gives the reference for the roll angle φ. However, we cannot lock the base rotation entirely for the cylinder link, indicated in Fig. 1; the reference for roll is not accurate enough. The angle ψ in Fig. 4 corresponds to the joint 3 angle in Fig. 3. Notably, it is not the yaw angle of the grasper in the world frame, as the encoder of joint 3 only gives the rotation angle of the grasper with respect to the body-fixed frame of the link between joints 2 and 3.

Once the link of the grasper is perpendicular to the ground, world frame roughly align with body-fixed frame of the grasper, then the yaw angle coincides with ψ.

III. Mathematical Background

A. Angular Velocity Modulation with a Rotation Gyroscope

Denote the measurements of the gyroscope of the rotation IMU as w_x and w_z, on the x and z axes respectively. Written as true angular rates plus long-term bias and noise:

$$w_x = w_{xt} + b_x + n_x \,, \tag{1}$$

$$w_z = w_{zt} + b_z + n_z \,. \tag{2}$$

Ignoring the noise terms, we transfer these two outputs into the body-fixed frame of the grasper:

$$\dot{\theta}_{bx} = (w_{x_t} + b_x)\cos\emptyset_k - (w_{z_t} + b_z)\sin\emptyset_k \,, \tag{3}$$

$$\dot{\theta}_{bz} = (w_{z_t} + b_z)\cos\emptyset_k + (w_{x_t} + b_x)\sin\emptyset_k \,, \tag{4}$$

where $\emptyset_k$ is the rotation angle of the IMU box. It is the angle of the sensor frame with respect to the body-fixed frame of the grasper, determined by

$$\emptyset_k = \int_0^{t_k} r\, dt \,. \tag{5}$$

In (5), r is the rotation speed of the IMU box. If we assume r is constant and combine (4) and (5), we notice that the integration term that contains the long-term bias will disappear after one complete circle.

In (5), r is the rotation speed of the IMU box. If we assume r is constant and integrate (3) and (4), we notice that the integration term that contains the long-term biases b_x and b_y will disappear after one complete circle.

We set the rotation speed of r in (5) as 250 °/s. The rotation speed of the grasper in each direction is less than 50 °/s for most of the testing time, much smaller than the rotation speed of the gyroscope. Therefore, in our implementation, the majority of angle error caused by long-term bias in two axis directions of the gyroscope can be removed.

For the rotation speed of the grasper in the y-axis of its frame, we use the measurement of gyroscope in this direction minus the angular speed of the IMU box in this direction, which can directly get from the encoder installed with the IMU-box as showing in Fig. 2.

$$\dot{\theta}_{bz} = w_y - r \tag{6}$$

From (3), (4) and (6) we form a virtual gyroscope, which gives the rotation speed of the grasper with respect to the world frame expressed in the body-fixed frame of the grasper.

$$\omega = \begin{bmatrix} \dot{\theta}_{bx} \\ \dot{\theta}_{bz} \\ \dot{\theta}_{bz} \end{bmatrix} \tag{7}$$

B. Angle Integration with Quaternion Form

Since integration of quaternion form for angular velocity is computationally light, and usually the computer of an embedded system has very limited computational resources, we choose quaternion form for expressing rotation.

Defining the rotation quaternion from world frame to local frame in time step k as

$$q_k = \begin{bmatrix} q_1 & q_2 & q_3 & q_4 \end{bmatrix}^T_k \,, \tag{8}$$

the time derivative of q_k becomes

$$\dot{q}_k = \frac{1}{2} q_k \otimes \begin{bmatrix} 0 \\ \omega_k \end{bmatrix} = \frac{1}{2}\Omega(\omega_k) q_k \,, \tag{9}$$

where $\otimes$ denotes quaternion multiplication, ω_k is expressed in the local frame of the grasper in time step k ,which is given by (7), and $\Omega(\omega_k)$ has the form

$$\Omega(\omega) = \begin{bmatrix} 0 & -\omega_x & -\omega_y & -\omega_z \\ \omega_x & 0 & \omega_z & -\omega_y \\ \omega_y & -\omega_z & 0 & \omega_x \\ \omega_z & \omega_y & -\omega_x & 0 \end{bmatrix} . \tag{10}$$

The integration of the rotation quaternion is

$$q_{k+1} = q_k + \dot{q}_k \Delta t \,, \tag{11}$$

where Δt is the sample interval. In addition, (11) is derived based on the Taylor series of $q(t_k + \Delta t)$ around time $t = t_k$, keeping only the first order term. For our implementation, the sample interval is 0.002 seconds. Compare (11) with other complete form, during 3 minutes, the maximum difference is less than 0.15 degree.

The complete integration form is First order integration in [10],

$$q_{k+1} = q_k \otimes \left(q\{\bar{\omega}\Delta t\} + \frac{\Delta t^2}{24} \begin{bmatrix} 0 \\ \omega_k \times \omega_{k+1} \end{bmatrix} \right) \,, \tag{12}$$

where

$$\bar{\omega} = \frac{\omega_k + \omega_{k+1}}{2} \,, \tag{13}$$

and

$$q\{\bar{\omega}\Delta t\} = e^{\bar{\omega}\Delta t} = \begin{bmatrix} \cos(\|\omega\|\Delta t/2) \\ \frac{\omega}{\|\omega\|}\sin(\|\omega\|\Delta t/2) \end{bmatrix}, \tag{14}$$

(12)-(14) is more accuracy than (11), when sample frequency is lower, since it consider angular acceleration and no ignoring of higher order terms. In this paper, the test results is from (11).

We define the initial quaternion as (15), where the frame of the grasper aligns with the world frame:

$$q_0 = \begin{bmatrix}1 & 0 & 0 & 0\end{bmatrix}^T . \quad (15)$$

In every time step, normalize the quaternion as

$$q_k = \frac{\|q_k\|}{q_k} . \quad (16)$$

The references from encoders in the unactuated joints indicated in Fig. 3 are in the form of Euler angles. Convert the rotation quaternion into Euler angles with (17)-(19):

$$\phi_k = \arctan 2(2(q_{1k}q_{2k} + q_{3k}q_{4k}), \\ 1 - 2(q_{2k}^2 + q_{3k}^2)) \quad (17)$$

$$\theta_k = \arcsin(2(q_{1k}q_{3k} + q_{4k}q_{1k})) \quad (18)$$

$$_w\psi_k = \arctan 2(2(q_{1k}q_{4k} + q_{2k}q_{3k}), \\ 1 - 2(q_{3k}^2 + q_{4k}^2)) \quad (19)$$

where $\arctan 2$ is a function that the return value is in four quadrants. q_{k1} to q_{k4} are the elements of quaternion q_k . $_w\psi_k$ is given in world frame, however, the reference of joint 3 is expressed in local frame, as shown in Figs. 3 and 4.

C. Calibration of the Gyroscope

In [8] and [9], a method for calibrating MEMS IMUs is given. For our implementation, if the IMU rotates around the y-axis, ignoring the Earth rotation, a simple error model for the gyroscope is

$$\begin{bmatrix}\delta\omega_x \\ \delta\omega_y \\ \delta\omega_z\end{bmatrix} = \begin{bmatrix}k_{xy}\omega + d_x \\ S_y\omega + d_y \\ k_{zy}\omega + d_z\end{bmatrix} , \quad (20)$$

where d_x, d_y, and d_z are the gyroscope biases in the sensor frame, and $[\delta\omega_x \quad \delta\omega_y \quad \delta\omega_z]^T$ is the error of the gyroscope in the sensor frame. k_{xy} is the factor of the installation error for the x-axis in relation to the y-axis, which means if the y-axis has a rotation speed of ω , because of the installation position inaccuracy it will project into the x-axis an angular speed with that factor. k_{zy} is the factor of the installation error for the z-axis in relation to the y-axis. S_y is the scale factor in the y-axis, indicating the nonlinearity of the gyroscope in this axis, and ω is the rotation speed of the y-axis.

IV. Results

A. Test Procedure

First, we keep the IMU box and the manipulator stationary for about 30 seconds, take the mean values from the gyroscope's raw output in the x-, y- and z-axes, compare it with zero, and get the bias d_x, d_y and d_z, as defined in (20). Then, only the IMU box is rotated for about 30 seconds, and we take the mean value of the output of gyroscope, with the biases d_x and d_y from the first phase. Using (20), we get k_{xy}, k_{zy} and S_y. From about 70 s, the manipulator is moved frequently, swaying the grasper. During 104 s to 115 s of the test, the sway is manually stopped

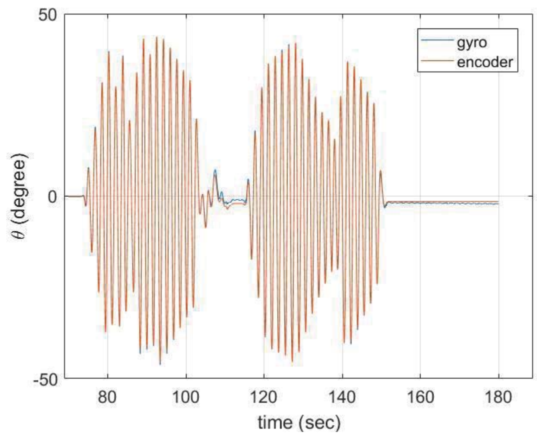

Fig. 5. Pitch angle of the system sway, red line is the reference from encoder, and blue line is from integration of gyroscope.

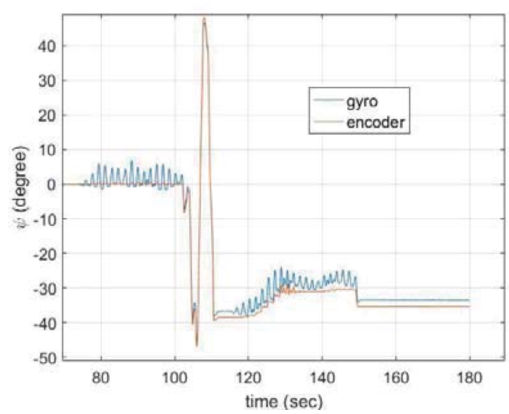

Fig. 6. Rotation of the grasper. The results from the encoder match the reference only during the periods from 104 s to 115 s and 151 s to 180 s.

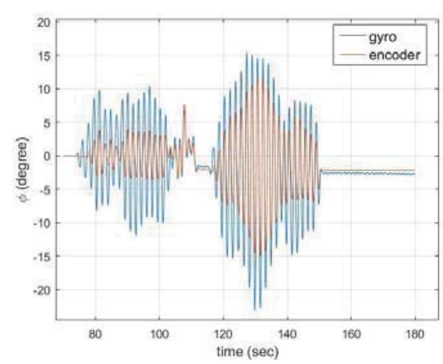

Fig. 7. Roll angle of the system's sway, since the cylinder link of crane has oscillation, the amplitude of gyro's output is bigger than encoder's.

and the grasper is rotated, simulating external disturbances. At about 151 s, the swaying is manually stopped again, ending the test at 180 s.

B. Results Analysis

Fig. 5 shows the sway in pitch direction; the maximum amplitude is about 45 degrees. The error RMS is 0.831 degrees, and the maximum error is 2.95 degrees at about 127 s. During 104 s to 115 s, θ only has small oscillation, and the curve of

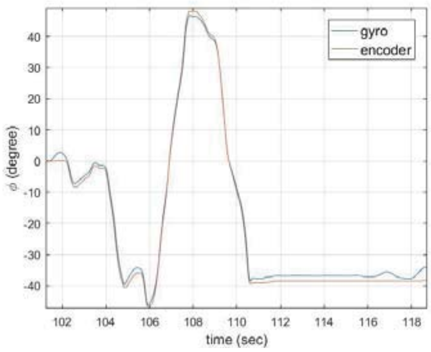

Fig. 8. Yaw rotation of the grasper, with the local frame aligned with the world frame. Enlarged from Fig. 6.

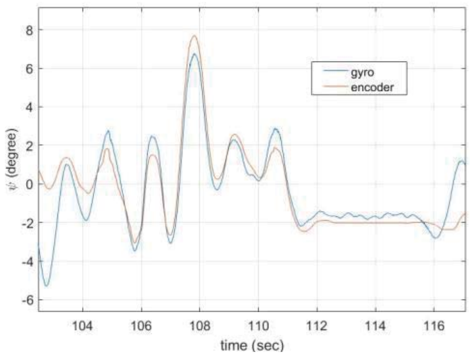

Fig. 9. Sway of the system in roll direction, when the cylinder link of crane has a small rotation angle. Enlarged from Fig. 7.

integration also follows the reference well, with the error peak being less than 1.8 degrees.

Although the calculation result and the reference for the rotation of grasper present in Fig.6 together, but only during two periods (104 s to 115 s, and 151 s to 180 s), the reference is accuracy, since the world frame coincides with the local frame of joint 3 at these moments, as mentioned in Section. II and Section. III. B.

The part of the test from 104 s to 115 s in Fig. 6 is shown enlarged in Fig. 8 The error RMS is 1.43 degrees for this period, while the maximum error is 2.41 degrees and the offset from 110.5 s to 116 s is about 1.7 degrees. During the last period of the test, from 151 s to 180 s, there is also an offset; it is about 1.8 degrees. This offsets may be because of wobble error. In our case, we consider it as the axis of joint rotation is not aligned with the defined axis of the sensor.

As mentioned in Section. II, the cylinder link of the crane has rotation, so the encoder of joint 2 cannot give an accurate reference in world frame. However, after more than 40 seconds of angle integration, once the boom is kept relatively stationary during 104 s to 115 s, the result of the angle calculation from the gyroscope in roll direction roughly follows the reference curve, and as shown in Fig. 9, the maximum error is less than 2 degrees.

V. Discussion

As described in Section. IV. A, our calibration phase lasts for about 60 seconds. This is because our rotation platform of IMU simply installed on the grasper, the rotation axis of the motor is easily have some changing respect to the gyro's axis. The installation error of the gyro may also slightly change as the temperature varies since the components of devices deforms, but this change is small, and we can count it into the gyro's biases d_x and d_y in (20). In fact, these two biases do not need calibration if we have rough values of the installation error for the two axes, because rotation modulate the long-term of bias, as indicated by (3)-(5), and we use industry-grade gyroscope, the bias is relatively small compared to low-cost gyroscopes. Using the data contain the bias in the two axes only produce some small amplitude oscillation of sine wave in angle integration, if the gyroscope rotate with constant speed. For our implementation, this small sine wave has a small effect; we can notice it from the ending part of the blue lines, in Fig. 5 and Fig. 7.

The raw data of angular velocity is presented in Fig. 10 to show the installation error of the gyro. The rotation platform is kept stationary during data collection. In the beginning, the gyroscope doesn't rotate, and the z-axis output is around zero. Once the gyroscope starts rotating around the y-axis with a velocity of 250 °/sec, the z-axis of the sensor has an output of -4 °/sec, although the rotation platform itself has no rotation with respect to the world frame. The chosen angular velocity of 250 °/sec is dependent on the range of the gyroscope, ±450°/sec, as the grasper's swing can be more than 150 °/sec. A faster rotation speed could provide better results, if a gyroscope with a wider range was available.

Moreover, once the rotation motor starts, the noise in output from gyroscope increases significantly, and some oscillation is introduced. The introduced noise may be from the electrical motor and the oscillation might result from the center of mass of the IMU not being correctly aligned with the axis of rotation. For a more reliable and higher performance test bed, updating the rotation platform is required.

In the rotation axis of the gyroscope, y-axis, there is no correction method applied to the angular velocity except for the calibration during the beginning. This means that for long-term operation, the integration of the angle will diverge. As discussed above, we may only need to correct the scale factor and bias in the rotation axis. The scale factor of the gyroscope in rotation axis is dependent on temperature, the nonlinearity of the gyroscope in y-axis of the gyroscope, and the installation accuracy between the rotation axis and the sensor axis. Rewrite the second equation of (17) as

$$\begin{aligned}\delta\omega_y &= S_y\omega + d_y \\ &= ({}^{con}S_y + \Delta S_y)\omega + d_y \\ &= {}^{con}S_y\omega + \Delta S_y\omega + d_y \\ &= {}^{con}S_y\omega + \Delta D_y\end{aligned} \quad , \tag{21}$$

where ${}^{con}S_y$ is fixed to a constant value close to the true value of the scale factor. Moreover, the remaining part of ${}^{con}S_y$, ΔS_y, is absorbed into ΔD_y as the rotation speed of the gyroscope is kept constant. Then, the system only needs to estimate one parameter, ΔD_y for the data processing, we try setting d_x and d_y as zero, k_{xy}

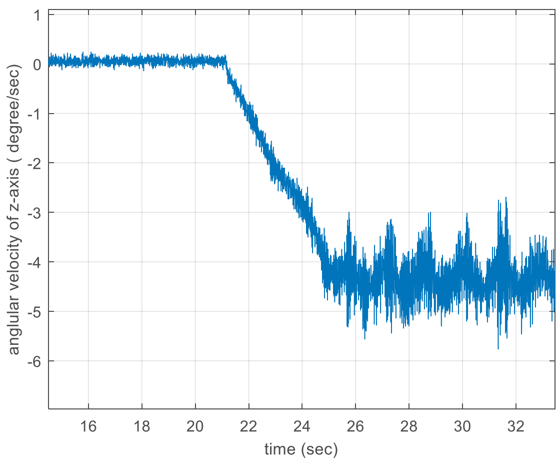

Fig. 10. Raw data from the output of the gyroscope. Once the gyroscope starts rotating, an angular error is projected into other axes.

and k_{zy} as constants close to the true value of installation error with some small constant deviation, but for ${}^{con}S_y$ and ΔD_y to give an accurate value, the result of angle output has no significant difference. Only some small oscillating wave is added, which is acceptable for our implementation. However, giving even a small constant disturbance bigger than 0.01 °/sec, the result has an obvious difference of about two degrees for two minutes of angle integration.

Accurately estimating ΔD_y for our system is easy in a stationary case: there is an encoder on the rotation platform, which can give an accurate observation of the varying angle. However, in a dynamic situation, as mentioned in Section I the model is difficult to build, and we may need to introduce other measurement sensors for correcting ΔD_y in the case of long-term operation without interruptions by calibrations of the gyroscope.

VI. Future Works

The test bed used in this paper is big and cumbersome for the needed task of rotating the gyroscope, and is not practical for real-world use or extensive testing. For future research, the test bed IMU box will be upgraded with a substantially smaller Analog Devices ADIS16475-3 IMU and a built-in rotary unit for the IMU. Fig. 11 shows the unit, containing a motor, an encoder and the rotating IMU connected with a slip ring. This allows us to rotate the IMU only, instead of rotating the complete IMU box. The following key components are added to the setup:

- Hengstler AD35 absolute encoder with length 24 mm and diameter 28 mm
- Six-wire slip ring SRC022-A, with a length of 28 mm and a diameter of 22 mm on the stationary side.
- Maxon DC-max 22 S motor, with length 36 mm and diameter 22 mm, pulse width modulation controlled via an H-bridge by an STM32F4 microcontroller

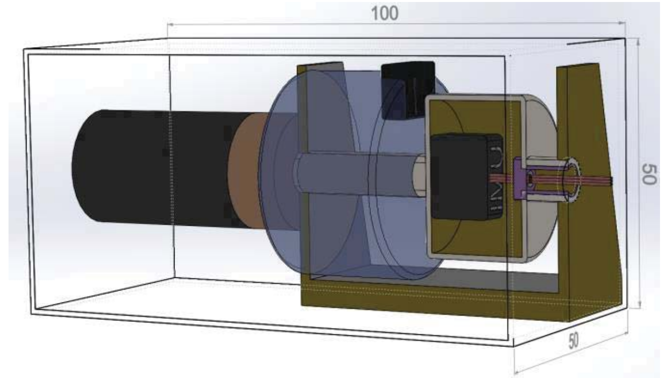

Fig. 11. Sketch of the planned rotary unit, with the motor on the left, encoder in clear blue, and IMU inside a cylinder connected to the slip ring.

The encoder will provide feedback to the microcontroller, which adjusts the speed of the motor to keep the IMU rotating with a steady velocity. The complete electromechanical system fits in an enclosure that is 100 mm long. All signals controlling the motor and reading the encoder and IMU data will be handled by the STM32F4 microcontroller, which sends the data to a real-time computer.

VII. Conclusion

An industry-grade gyroscope with a rotation platform can accurately calculate the attitude of the grasper of the crane. Within two minutes, the RMS error of the attitude is less than two degrees, which allows our method to be applied for anti-sway control in many cases.

Continuously rotating the gyroscope with an external motor can simplify the requirements needed of the angle-calculating algorithm. For long-term operation of the system, the device only need correct one parameters online, which is the bias of angular velocity on the rotation axis.

Acknowledgment

This research work was supported in part by the Doctoral School of Industry Innovations (DSII), by Tampere University of Technology (TUT), the Forum for Intelligent Machines (FIMA), and the Academy of Finland (Grant no. 294915).

References

[1] P. Mustalahti and J. Mattila, "Nonlinear full-model-based controller for unactuated joints in vertical plane," in *Proceedings of the 8th International Conference on Cybernetics and Intelligent Systems and Conference on Robotics, Automation and Mechatronics,* Ningbo, China, Nov. 2017, pp. 201-206.

[2] Y. S. Kim, K. S. Hong, and S. K. Sul, "Anti-sway control of container cranes: inclinometer, observer, and state feedback," *International Journal of Control, Automation and Systems*, vol. 2, no. 4, pp. 435-449, 2004.

[3] J. Kalmari, J. Backman, and A. Visala, "Nonlinear model predictive control of hydraulic forestry crane with automatic sway damping," *Computers and Electronics in Agriculture*, vol. 109, pp. 36-45, 2014.

[4] J. Kalmari, H. Hyyti, and A. Visala, "Sway estimation using inertial measurement units for cranes with a rotating tool," in *Proceedings of the 8th IFAC Symposium on Intelligent Autonomous Vehicles*, Gold Coast, Australia, Jun. 2013.

[5] X. Zhang, T. Mononen, M. M. Aref, and J. Mattila, "Mobile robotic spatial odometry by low-cost imus," in *Proceedings of the 14th International Conference on Mechatronic and Embedded Systems and Applications,* Oulu, Finland, Jul. 2018, pp. 1-6.

[6] J. Vihonen, J. Mattila, and A. Visa, “Joint-space kinematic model for gravity-referenced joint angle estimation of heavy-duty manipulators,” *IEEE Transactions on Instrumentation and Measurement*, vol. 66, no. 12, pp. 3280-3288, 2017.

[7] J. Vihonen, J. Honkakorpi, J. Tuominen, J. Mattila, and A. Visa, “Linear accelerometers and rate gyros for rotary joint angle estimation of heavy-duty mobile manipulators using forward kinematic modeling,” *IEEE Transactions on Mechatronics*, vol. 21, no. 3, pp. 1765-1774, 2016.

[8] S. Du, W. Sun, and Y. Gao, “MEMS IMU error mitigation using rotation modulation technique,” *Sensors*, vol. 16, no. 12, pp. 2017, Nov. 2016.

[9] S. Du, “Rotary inertial navigation system with a low-cost MEMS IMU and its integration with GNSS,” University Calgary, 2015.

[10] J. Sola, “Quaternion kinematics for the error-state Kalman filter,” *arXiv preprint arXiv:1711.02508*, 2017.

PUBLICATION
V

Localization of a Heavy-Duty Omnidirectional Vehicle Using IMU and Wheel Odometry

Xiaolong Zhang, Henri Liikanen, Eelis Peltola, Mohammad M. Aref, and Jouni Mattila

DOI: https://doi.org/10.1007/978-3-030-85318-1_67

Localisation of a Heavy-Duty Omnidirectional Vehicle Using IMU and Wheel Odometry

Xiaolong Zhang, Henri Liikanen, Eelis Peltola, Mohammad M. Aref, Jouni Mattila

Tampere University, Korkeakoulunkatu 7, 33720 Tampere, Finland

firstname.secondname@tuni.fi

Abstract. We introduce a localisation algorithm that uses an inertial measurement unit (IMU) and wheel odometry on a four-wheel-drive heavy vehicle for positioning. While wheel odometry alone works in simple cases without slippage, in cases that feature wheel slippage, the velocities measured by the wheel rotation show higher values. In the case of side slippage, the wheel sensors cannot observe the values. Therefore, IMUs are suitable for fusion with wheel odometry to generate real-time feedback. We use an error state Kalman filter (ESKF) to fuse the sensor information from an IMU with wheel odometry, showing results on a slow-manoeuvring vehicle in tests up to five minutes in length. The IMU is an industry-grade micro-electro mechanical system (MEMS) with a gyroscope featuring 6 deg/h bias in-run stability. We use a real-time kinematic global positioning system (RTK)-GPS as a ground truth reference for the vehicle's heading angle and position. The tests results show our navigation has an accuracy of 0.3 m for position and 0.6 deg for heading angle, both within the root mean square error (RMSE) criteria. Our analysis shows that the nonlinearity of the gyroscope in the heading rotation axis is the key factor for improving performance in our implementation.

Keywords: IMU, KF, wheel odometry, RTK-GPS, HACV

1 Introduction

The real-time motion control of mobile robots, such as our heavy-duty autonomous construction vehicle (HACV) test case, strongly depends on the quality of the feedback that the controller receives. Generally, sensory data for the wheels' rolling rate (i.e. wheel odometry) are the first source of information for the robot's motion. Wheel odometry is already used for the actuator-level control of each wheel, meaning these data are available for the localisation of the HACV at no hardware cost. However, using these sensors implies several practical issues.

First, due to manufacturing complexities and the harsh working environments of the robots, using fine and accurate sensors (e.g. micro pulse encoders or transducers) is not desirable. The sensor hardware must be simple, robust and easily mountable. For this purpose, metallic encoder discs are used for pulse generation with proximity sensors, such as the Hall effect or optical sensors read by counters. Therefore, we face coarse digital measurement outputs that are strongly affected by quantisation and zero-order holds. In the case of slow manoeuvring, which is common for heavy-duty vehicles, the sensors do not generate pulses on each of the control system's sample times. The output thus becomes an event-based signal as opposed to a time-based signal. For example, for a sample time of 50 ms, driving velocities below 0.25 m/s are not reliably measurable [1]. Usually, this issue causes limitations to the HACV in terms of minimum speeds for smooth feedback in autonomous driving.

Second, wheel odometry and its accuracy depend on researchers' correct assumptions about wheel–ground interaction and robot kinematics. In the case of the wheels' longitudinal slippage, the velocities measured by the wheel rotation will show higher values. In the case of the wheels' lateral slippage, the wheel sensors cannot observe the values at all. Therefore, inertial measurement units (IMUs) are a suitable choice for fusion with wheel odometry to generate real-time feedback. They are capable of transmitting absolute data at each sample time without considerable delays in operation or installation problems in manufacturing. These specifications highlight a strong need for IMUs, even when compared to global navigation satellite systems (GNSS) or radio frequency (RF)-based solutions: IMUs are not required to be in a GNSS-available environment, and they are independent of external information sources.

Based on the aforementioned issues, the main focus of this paper is on providing reliable and accurate feedback in real time by fusing wheel odometry with IMU signals. The software architecture for this is shown **Fig. 1**. We present a method that solves the minimum speed requirements for HACVs and preserves positioning accuracy that is comparable with the accuracy of an on-board GNSS.

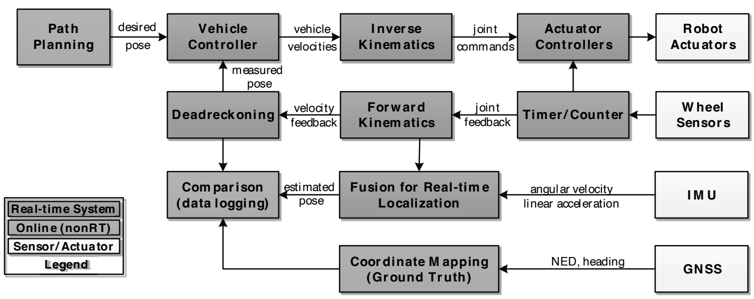

Fig. 1. The software architecture designed to validate the estimation outputs by wheel odometry and IMU in comparison with ground truth (GNSS)

We use an error state Kalman filter (ESKF) [1] to fuse the sensors' information. Moreover, we remove the state of local gravity bias, as our HACV only moves in a small area, and we can set the gravity as a constant based on the latitude and height of our test location [3]. The wheel odometry provides two velocity elements that are parallel to the ground tangential plane, expressed in the HACV's body-fixed frame [4]. For the third velocity element, which is approximately vertical to the ground plane, we apply a non-holonomic constraint [5, 6, 7]. This constraint simply assumes the velocity in the vertical direction to be close to zero with some Gaussian noise, which applies to one more observation element of KF and improves estimation performance.

Normally, a fine initialisation is time-consuming for an IMU [8] if there is no external observation, such as GPS or visual aiding. For our implementation's use cases, the HACV operator expects the start phase to be as short as possible. Additionally, our IMU cannot be used to find geographic North. Our algorithm applies a coarse initialisation at the beginning phase of each test, where the HACV is kept stationary for about 15 seconds. This allows the estimation of biases for the gyroscopes and accelerometers in addition to the initial roll and pitch angles of the HACV. We define the initial heading angle to be zero, as we are mainly concerned with the relative angle for the heading. We achieve accurate estimates of the initial roll and pitch angles merely after running the stationary model. The biases of the gyroscopes along these two axes are also accurate because the estimation uses gravity as a reference.

Through simulations with the test data, we find that small disturbances for the biases of gyroscopes in roll (x-axis) and pitch (y-axis) directions do not affect the estimation results. Thus, we only apply the correction for Earth's rotation along the z-axis, which is approximately along the direction of gravity and away from the ground. We make this correction by introducing the incremental angle of the Earth's rotation around the z-axis into the heading angle observation. For the same reason, we only apply the scale factor for the gyroscope's nonlinearity to the z-axis – the scale factor of the gyroscope in this direction contributes to the main part of the error of the heading angle.

Recently, researchers have used artificial intelligence (AI) combined with traditional filters for vehicle localisation with both IMU and wheel odometry sensors [9] or with IMUs alone [10, 11]. In [9], both the propagation and measurement functions of a dynamic model are improved with neural networks and stochastic variation inference. [10] and [11] use a neural network to use an invariant extended Kalman filter (IEKF) as an adaptive filter. Both [10] and [11] manipulate the filter's covariance or observations according to the deferent motion patterns of their vehicles. Combining [10] and [11], it is obvious that linear acceleration in the horizontal plane can correct the accumulated error of the yaw angle. In this paper, we follow the traditional KF approach, using two kinds of patterns for HACV movement: a stationary model and a moving model. However, we do not separate a model from the moving model in which linear acceleration is introduced in the horizontal plane with no rotation of the HACV. This is suitable for our short-term navigation (i.e. within five minutes). In our future work, we would like to experiment with using an adaptive filter for the long-term localisation of this kind of HACV.

2 Mathematical Background

In this section, subsection 2.1 describes the propagation for the nominal state with high-frequency IMU data and the estimated biases of the sensors. Subsections 2.2 and 2.3 include the prediction and observation models we used for the ESKF. The two observation models are for the two cases when the HACV is kept stationary and for the case when the HACV is moving. When the HACV is stationary, we use gravity as a reference for estimation, and while the HACV is moving, we use wheel odometry for the model's velocities, which are parallel to the observed motion plane. Subsection 2.4 outlines updates to the error state and the covariance matrix. For the nominal state updates, please refer to [2].

2.1 Nominal State Kinematics

The nominal state does not account for noise and model imperfections [2]; further, it corrects accumulated error by feeding it back to the error state. The nominal state is propagated as

$$\begin{bmatrix} p_k \\ v_k \\ q_k \end{bmatrix} = \begin{bmatrix} p_{k-1} + v_{k-1}\Delta t + \frac{1}{2}\{(R^n_{b\,k-1} f_{k-1} - g)\}\Delta t^2 \\ v_{k-1} + (R^n_{b\,k-1} f_{k-1} - g)\Delta t \\ \frac{1}{2}\Omega(\omega_{k-1}\Delta t) q_{k-1} + q_{k-1} \end{bmatrix} \qquad (1),$$

where the subscript k indicates the time step. P and v are the nominal position and velocity, respectively, expressed in the navigation frame. q is the nominal orientation quaternion of the body-fixed frame with respect to the navigation frame. Δt is the interval of the sample time. g is the local gravity vector of the test place. R^n_b is the rotation matrix; it transfers the specific force f expressed in the body-fixed frame to express it in the navigation frame. R^n_b is a function of the orientation quaternion q.

The specific force is

$$f = a_m - a_b \qquad (2),$$

where a_m is the measurement of the accelerometers and a_b is the current estimated bias of the triad-axis accelerometer.

The angular rate ω in (1) is

$$\omega = \begin{bmatrix} \omega_{mx} & \omega_{my} & (1-k)\omega_{mz} \end{bmatrix}^T - \omega_b \tag{3}$$

where ω_{mx} , ω_{my} and ω_{mz} are the measurements of the gyroscope in x, y and z directions, respectively; ω_b is its current estimated angular drift; k is the scale factor, which is a constant value indicating the non-linearity of the gyroscope. We only apply the scale factor in the z direction of the gyroscope.

In (1), Ω is a function of the angular rate and sample interval, taking the form

$$\Omega(\omega\Delta t) = \Delta t \begin{bmatrix} 0 & -\omega_x & -\omega_y & -\omega_z \\ \omega_x & 0 & \omega_z & -\omega_y \\ \omega_y & -\omega_z & 0 & \omega_x \\ \omega_z & \omega_y & -\omega_x & 0 \end{bmatrix} \tag{4}$$

On each time step, we normalise the orientation quaternion q_k .

2.2 Prediction Step of KF

The state has 15 elements:

$$\delta x = \begin{bmatrix} \delta p & \delta v & \delta\theta & a_b & \omega_b \end{bmatrix}^T \tag{5}$$

where δp is the position error and δv is the velocity error, respectively. $\delta\theta$ is the error of orientation in Euler form, with the three elements being roll, pitch and yaw; a_b and ω_b are the biases of the accelerometers and the gyroscope, respectively. Each time there is an update in the error state of KF, we reset the error states of position, velocity and orientation as zero; thus, in (16), we ignore the error state. Since the biases a_b and ω_b have relatively small values, in practice, we keep their state values instead of resetting them to zero.

In KF, we use the Euler form to represent the orientation error; however, this is in quaternion form for the state propagated in (1). Our IMU's sample frequency is approximately 1000 Hz; propagating the system state (5) requires the transformation matrix

R_b^n . This process only involves algebraic operations and does not include sine or cosine functions. The observation datum for the error state KF is 10 Hz – as the KF updates the state, the attitude must be transferred from the quaternion form to the Euler angle form and then transferred back again. This involves sine and cosine functions; however, it only runs at 10 HZ, which is much lower than 1000 HZ. So the computation load is not a problem, even when we apply a relatively higher sample frequency of 1000 HZ.

The transition matrix is

$$F = \begin{bmatrix} I & I\Delta t & O & O & O \\ O & I & -[R_b^n(a_m - a_b)]_\times \Delta t & -R\Delta t & O \\ O & O & I & O & -R\Delta t \\ O & O & O & I & O \\ O & O & O & O & I \end{bmatrix} \quad (6),$$

where I is a 3 x 3 identity matrix and O is a 3 x 3 zero matrix. $[R_b^n(a_m - a_b)]_\times$ is the accelerometer output minus its bias, rotated into the navigation frame and expressed in a skew-symmetric form.

The state covariance propagate as

$$P_{k+1}^{\ \ -} = F_k P_k F_k^{\ T} + BQ_i B^T , \quad (7),$$

where the covariance matrix of perturbation impulses is

$$Q_i = \begin{bmatrix} \sigma_{\bar{a}}^2 \Delta t^2 I & O & O & O \\ O & \sigma_{\varpi}^2 \Delta t^2 I & O & O \\ O & O & \sigma_{ar}^2 \Delta t I & O \\ O & O & O & \sigma_{\omega r}^2 \Delta t I \end{bmatrix} \quad (8)$$

In (8), $\sigma_{\bar{a}}^2$ and σ_{ϖ}^2 are the covariance for the measurement noise of accelerometer and gyroscope, respectively. σ_{ar}^2 and $\sigma_{\omega r}^2$ are the covariance for the random walk of accelerometer's bias and gyroscope's drift, respectively.

The Jacobian of the perturbation in (7) is

$$B = \begin{bmatrix} O & O & O & O \\ I & O & O & O \\ O & I & O & O \\ O & O & I & O \\ O & O & O & I \end{bmatrix} \tag{9}$$

2.3 Observation Step of KF

When the HACV is stationary, we take the velocity to be zero in three directions and fix the heading angle as an initial value or the value right before the HACV's velocity becomes zero minus the current estimated velocity and current estimated heading:

$$z_{k+1} = \begin{bmatrix} 0 \\ 0 \\ 0 \\ \psi_{fix} - \omega_{earth} \sin(La) t_{k+1} \end{bmatrix} - \begin{bmatrix} \hat{v}_x \\ \hat{v}_y \\ \hat{v}_z \\ \hat{\psi} \end{bmatrix} \tag{10}$$

Here, the current estimate is the best-estimated states of the previous time step propagated forward one time step using (1). ψ_{fix} is the fixed value for the heading angle when the HACV is stationary; ω_{earth} is the Earth's rotation rate; La is 61.4°N, the latitude for our test location; t_{k+1} is the current time from the test's beginning.

The Jacobian of (10) is

$$H_{k+1} = \begin{bmatrix} 0_{3\times3} & I_{3\times3} & 0_{3\times9} \\ 0_{1\times8} & 1 & 0_{1\times6} \end{bmatrix} \tag{11}$$

When the HACV is moving, the observation is

$$z_{k+1} = fC_o^I \begin{bmatrix} v_{bx} \\ v_{by} \\ 0 \end{bmatrix} - V_b \tag{12},$$

where v_{bx} and v_{by} are the velocities of the HACV's centre of control in x and y directions, expressed in the body-fixed frame of the wheel odometers and measured by the wheel odometers. We set the velocity of the HACV in z direction to zero using the non-holonomic constraint [6, 7]. f indicates the efficiency of the wheel odometer; since we carefully calibrated our system, we set the value as one for the test in this paper. C_o^I is the matrix denoting any misalignment between the velocity of the wheel odometer and the body-fixed frame of the HACV, which we set as identical for our tests. V_b is the current estimated HACV velocity, expressed in the body-fixed frame of the HACV. It is a function of the estimated velocity $\hat{v}_n$ and the attitude transformation matrix from the navigation frame to the body-fixed frame R_n^b.

$$V_b = R_{n\,k+1}^{b} \hat{v}_n - \omega \times l \tag{13),}$$

where ω is defined in (3) and l is the coordinate of the IMU in the body-fixed frame of the HACV, defined as the constant vector $l = \begin{bmatrix} -1.18 & 0 & 0.4 \end{bmatrix}^T$ m for our case.

The Jacobian of (12) is

$$H_{k+1} = \begin{bmatrix} 0_{3\times3} & R_{b\,k+1}^{n} & 0_{3\times6} & -L \end{bmatrix}, \tag{14),}$$

where L is the skew-symmetric form of coordinate vector l.

2.4 Update Step of KF

The gain of the KF, K, is expressed as

$$K = P^{-}_{k+1} H_{k+1}{}^{T} (H_{k+1} P^{-}_{k+1} H_{k+1}{}^{T} + V)^{-1}, \tag{15),}$$

where V is the matrix of observation noise (depending on which model we use): the stationary model from (10) and (11) or the moving model from (12) and (14).

The error state of each time step is

$$\delta x = K z_{k+1} \tag{16}$$

The update for the covariance matrix is

$$P_{k+1} = (I_{15\times15} - KH) P^{-1}{}_{k+1} \tag{17}$$

Once the observation data come in, the KF outputs the error state δx ; this error state is fed back to the system propagator as defined in (1). Then, the system state, position, velocity and orientation are updated as detailed in [1].

3 Experiment Platform

We conducted our experiments with a Haulotte 16RTJ PRO heavy-duty articulating lift boom with four-wheel drive and active steering [12]. For autonomous driving, we fitted this HACV with a Beckhoff CX2030 real-time platform, which has several modules for interfacing with different sensors and actuators. For each wheel, we installed a Panasonic PM photoelectric odometry sensor, sensing 150 equally distributed holes in a metallic disc; they have a data rate of 1000 Hz.

The IMU used in the test, installed on the body of the HACV, is an Analog Devices ADIS16485 MEMS IMU. Its in-run stabilities are 6 deg/h angular for its triaxial gyroscope and 32 μg for its triaxial accelerometer. It is connected to the CX platform with a controller area network (CAN).

We used a Novatron BX982 differential carrier-phase GNSS receiver with two Trimble LV59 antennas to provide a reference for positioning. The antennas are located 2.6 meters apart on the lift boom HACV; one antenna gets the position of the HACV, and the other is used to form the heading vector for the HACV yaw angle with the first antenna. A commercial base station located 13 kilometres away gives an RTK reference point for correction. Using this correction, the accuracy for horizontal position is ±0.02 meters, and the accuracy for the yaw angle is ±0.09 degrees. The GNSS receiver has a data rate of 50 Hz and is connected to the CX platform via Ethernet user datagram protocol (UDP).

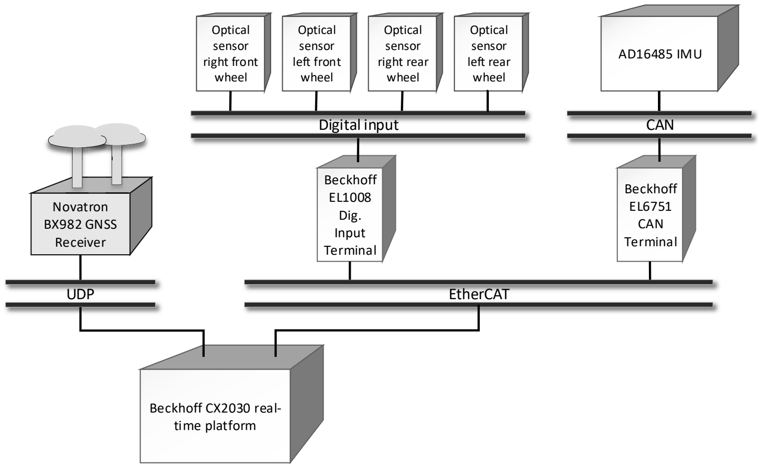

Fig. 2. Project-specific sensor architecture on the Haulotte

Fig. 2 shows the sensors and their connections to the real-time platform. The GNSS receiver also receives its RTK corrections via a mobile network connection on a router in the lift boom HACV.

The Beckhoff CX platform runs the TwinCAT software system; it reads all the sensors. Underlying the sensor connections shown in **Fig. 2**, the CX platform communicates with its modules in EtherCAT. With the exception of the UDP interface, which we wrote in the TwinCAT PLC language, we did all of our programming in Matlab Simulink and built for the TwinCAT system from Simulink.

We performed the tests in Finnish winter conditions, with some sleet on the ground resulting in wheel slippage. The lift boom HACV is shown in **Fig. 3** in the test conditions. A path-following controller handled the steering of the HACV with no manual manoeuvring. We conducted several runs ranging from 1–5 minutes using planned paths.

Fig. 3. The Haulotte lift boom in test conditions

4 Test Results

We include test cases in this article: one trajectory is roughly a triangle shape, and the other is roughly a square shape. Because the installation position of the IMU is at an offset with respect to the control centre of the wheel odometry, the position outputs from KF are transferred to the frame that the wheel odometry uses, represented as a black line in **Fig. 4.** and **Fig. 6.** Similarly, the position outputs from RTK-GPS are also transferred to the centre of the wheel odometer and used as ground truth. They are represented as a red line; the blue line is the HACV's position trajectory calculated only using wheel odometry.

The yaw angles, or HACV heading's evolution in time, are shown in **Fig. 5.** and **Fig. 7.** for the two test cases. As in **Fig. 4.** and **Fig. 6.**, the red line is from the RTK-GPS and is regarded as the ground truth; the blue line represents the wheel-odometry-only calculation. The black line is the yaw estimated by KF. The initial heading angle is set as zero, and the yaw angle output is the angle from the GPS minus its initial value.

During the tests, we kept the engine on at all times. We kept the HACV stationary at the initial stage; KF uses (10) for observation. When the HACV started moving, the observation of KF switched to (12) and remained as such until the test was complete. For the square shape movement, from 0 s to 18 s, and from 155 s to 185 s, we kept the

HACV stationary. For the triangle movement, the stationary phases are from 0 s to 15 s and from 255 s to the test's end.

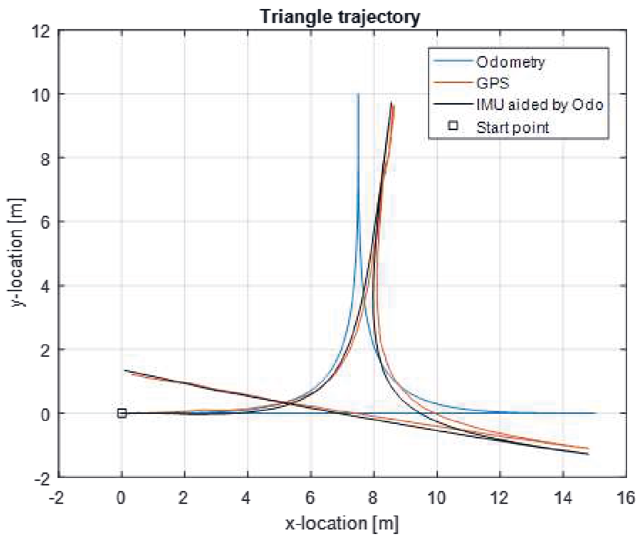

Fig. 4. The trajectory estimated by IMU and wheel odometry roughly matches the ground truth from RTK-GPS. Adding the IMU compensates for the effect of slippage that is apparent when only using the wheel odometry.

Table 1. Test results

Trajectory	***Position RMSE (m)***	***Heading RMSE (Degree)***	***Maximum Position Error (m)***	***Maximum Heading Error (Degree)***
Triangle	0.199	0.55	0.310	2.27
Square	0.314	0.56	0.490	2.28

Table 1 summarises the results of the two test cases. The RMSE of the position represents the absolute distance error in the x–y plane compared with the RTK-GPS output. The output frequency of RTK-GPS is 50 Hz, and the 1000 Hz output of KF is sampled down to 50 Hz when calculating the test results.

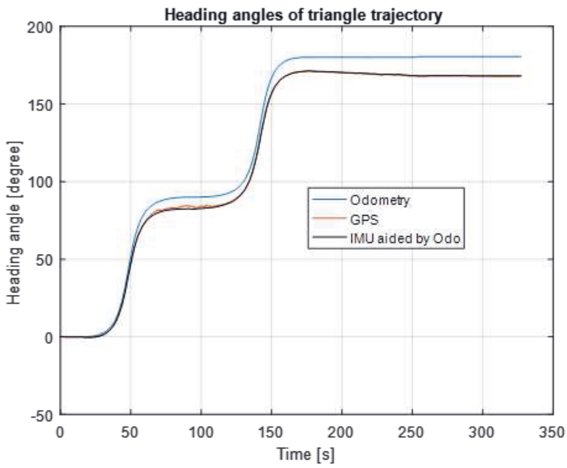

Fig. 5. The heading angle of the HACV continually increases from 0 deg to about 180 deg. Combined with the IMU, the estimated results nearly match the ground truth from the RTK-GPS.

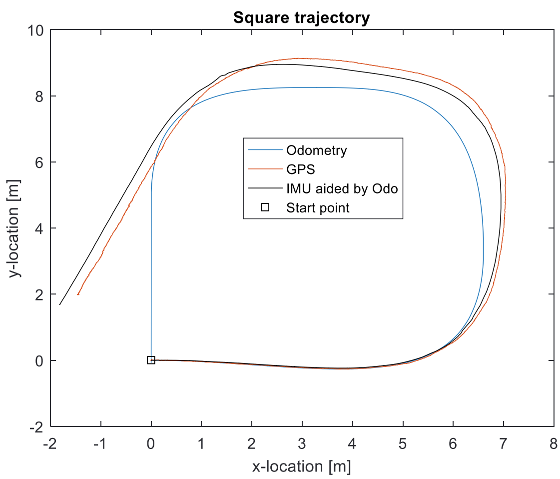

Fig. 6. The trajectory generated by wheel odometry only drifts away compared to the ground truth; however, the trajectory of IMU aided by wheel odometry roughly matches the ground truth.

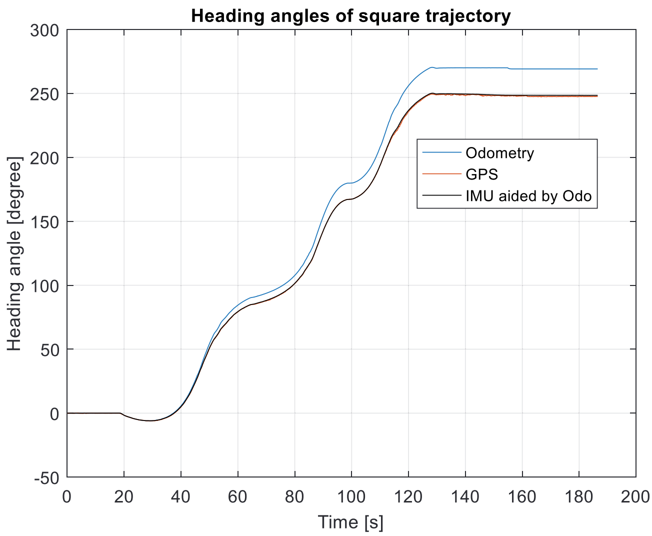

Fig. 7. The heading angle of the HACV continually increases from 0 deg to about 250 deg. Combined with the IMU, the estimated result nearly matches the ground truth from the RTK-GPS. However, using wheel odometry only, the error of the heading angle deviates from the ground truth after each sharp turn of the HACV.

5 Discussion

At the beginning of each test, we keep the HACV stationary for 10–20 seconds to determine the biases of gyroscope and accelerometer and to correct the initial roll and pitch angles. The initial yaw angle we simply set as zero.

The in-run stability of the IMU's gyroscope is 6 deg/h [13]; this accuracy is not enough to justify using only IMU to determine geographical direction. However, for a period of several minutes, the drift of the gyroscope's bias should be small. Moreover, the HACV is moving on ground covered with ice and snow – a very slippery environment – which means the observation velocities from wheel odometry, v_{bx} and v_{by}, have high deviations from the true velocities of the HACV base. Using them to correct the altitude of the HACV and the IMU biases is difficult. Because slipping happens frequently, if we tried to use the wheel odometry to correct the attitude, the output of the HACV velocity would deform. In [8], the authors mention that the added linear acceleration helped them to resolve the ambiguity of IMU bias. However, for our implementation, when there is linear acceleration when moving, slipping occurs regularly; thus, we do not use angular velocity from the wheel odometry in the observation step of the KF.

Now, we summarise the strategy of tuning the parameters of the KF: during the HACV's stationary model, we let the KF converge as quickly as possible to get the biases a_b and ω_b . When switching to the moving model, we update the state using the observations v_{bx} and v_{by} by changing the velocity and not the attitude. The parameters for the KF process noise in (8) are summarised in **Table 2**.

Table 2. Process noise

$\sigma_{\bar{a}}$	σ_{ϖ}	σ_{ar}	$\sigma_{\omega r}$
0.05 *m/s*	5 *deg/s*	0.007 $m/s^{1.5}$	0.0001 $deg/s^{0.5}$

We set the standard deviations for observation noise in the stationary model at 0.02 deg/s for velocity and 0.05 deg/s for heading angle. For the moving model, we set the noise parameter for velocity observation at 7 deg/s and the noise parameter for non-holonomic velocity at 2.5 m/s.

We set the initial standard deviation for the gyroscopes' bias at 0.8 deg/s and at 0.02 m/s^2 for the accelerometers' bias.

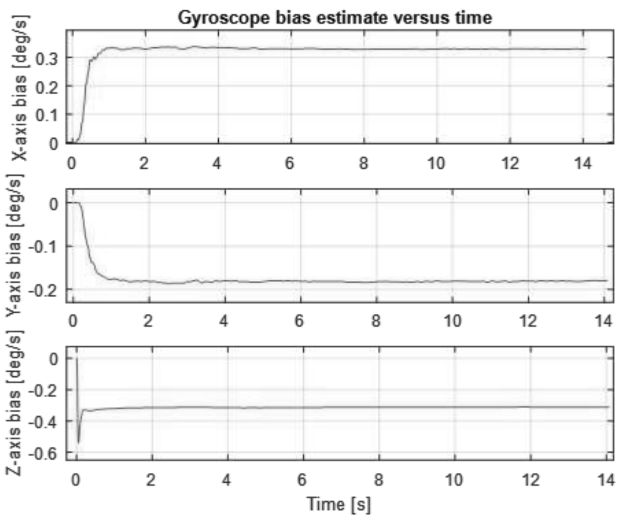

Fig. 8. As the HACV is kept stationary, the bias of the gyroscope converges to a steady state within several seconds. We can use the steady state values for short-term navigation even without updating the state of bias.

As an example, **Fig. 8.** shows the output of the estimated bias for the gyroscope in the triangular trajectory test when the KF is in the stationary model. The gyroscope's bias roughly converges to a steady state within several seconds in all three directions. When the KF switches to the motion model after 14 s, these biases keep a roughly constant value. In the x and y directions, the estimation of the gyroscope's biases can withstand an error of at least up to 0.02 deg/s. With the final values of the gyroscope's bias just after the stationary model starts running, we only add disturbances in the x and y directions, the standard deviation of which is 0.02 deg/s. We inject these three gyroscope biases as the initial state for the KF and set the initial uncertainty of the gyroscope's bias as a very small value: 0.0001 deg/s. We find that the output results have no significant difference compared to when the gyroscope's initial biases are set to zero: only a 1 or 2 cm position RMSE, less than 0.2 deg in yaw angle RMSE. This is because in terms of the roll and pitch directions, the angle estimation can use gravity as a reference.

However, in the z direction (i.e. mainly for the yaw rotation), the results are very sensitive to the gyroscope's bias. Running a motion model for 5 min, we expect the estimation accuracy of the gyroscope's bias in the z direction to reach 0.002 deg/s just after the stationary model stops running. Because there is no other information except for wheel odometry, and because the KF does not use the information from the wheel to correct the attitude (as mentioned previously), the yaw angle accuracy mainly depends on the accuracy of the estimated angular rate in the z direction.

In (10), we add the Earth's rotation effect only for the yaw angle observation. Because the gyroscope's z direction is roughly aligned with gravity, the maximum roll and pitch angles are less than 2 deg. As the HACV only moves in a small area with a known latitude, we set the latitude to a constant value in the test. Thus, the Earth's rotation vector projected into the z direction of the gyroscope is roughly constant. Projecting the Earth's rotation into the x and y axes of the gyroscope results in small values, and they do not affect the test results even when completely ignored in our model. Again, this is because we have gravity as a reference for the roll and pitch angles.

Fig. 9. shows the heading angle error, which we generate by comparing RTK-GPS and KF output with three different settings: the red line corresponds to removing the Earth's rotation in (10). Compared with the blue line, where no removal was done, we notice that for motion taking place for longer than 300 s, the accuracy of the heading angle is about 1 deg worse without the correction of the Earth's rotation. In (10), the value of ψ_{fix} is in respect to an Earth-fixed frame; we also observe it in the Earth-fixed frame. Then, the value for $\psi_{fix} - \omega_{earth} \sin(La) t_{k+1}$ is with respect to the inertial frame but observed in the Earth-fixed frame for the still HACV; the strap-down gyroscope measures the angular rate with respect to the inertial frame. Therefore, the stationary model of our KF outputs a gyroscope's bias in the z-axis, which roughly removes the effect of the Earth's rotation.

From 15 s to 175 s in **Fig. 9.**, the HACV rotates with an angular rate with a maximum value less than 5.2 deg/s in the yaw direction. The yellow line shows that without the scale factor correction, the heading angle error increases more than 2 deg. The scale factor only has an effect when there is an angular rate. For example, from 175 s to 275 s, the HACV moves in a straight line and then remains still until the end. Therefore, after 175 s, the error of the heading angle does not increase even without correcting the scale factor.

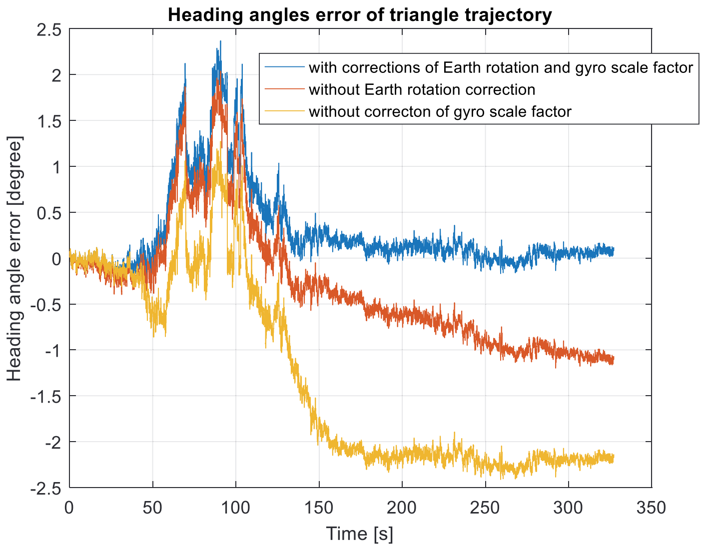

Fig. 9. The result of the estimation for yaw angle improves significantly by introducing the Earth's rotation into the yaw angle observation and including a scale factor in the z-axis for the gyroscope.

For both the triangle and square trajectory tests, the scale factor in (3) takes a constant value of 0.013 after intensive simulations and trials; both of these tests with this scale factor yield optimal results. The scale factor can be regarded as a local parameter; for our tests, the maximum angular rate is less than 6 deg/s, but the full measurement range for the gyroscope is 450 deg/s. The gyroscope's scale factor mainly depends on temperature and the input angular rate, and it can be written as a polynomic formula with these two parameters [14]. For our implementation, we only needed to do a pre-calibration for the gyroscope's bias in the z-axis within a range of angular rate and a range of temperature.

As mentioned previously, our KF does not use the velocity from wheel odometry to correct the altitude states, as it mainly constrains the magnitude of the velocity states. Additionally, our gyroscope's measurement and bias has no jumps. However, in **Fig. 9.**, from about 45 s to 140 s, the error of the heading angle has several peaks. This is because our RTK-GPS has some abnormalities for the yaw angle output during that time. In **Fig. 10.**, we enlarge the local part of **Fig. 5.**, clearly showing that the heading angle from GNSS has some jumps, the magnitudes of which reach 1 deg. This phenomenon is shown in the square trajectory test. This also indicates that the maximum error of the heading angle may in reality be smaller than 1 deg for our tests.

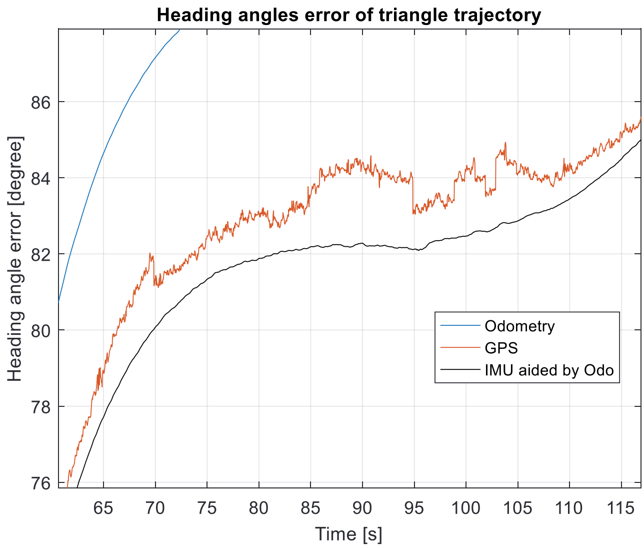

Fig. 10. The RTK-GPS output for the yaw angle's reference has abnormalities in several points.

6 Conclusion

For an HACV that moves slowly on roughly level ground, we use a high-end industry-grade MEMS IMU aided with wheel odometry to obtain an accuracy of heading angle within 1 deg (and 50 cm accuracy for position). The navigation time span is about 5 min, using a coarse initial alignment of less than 15 seconds of data when the HACV is kept stationary. The main limitation is the nonlinearity of the gyroscope on the heading rotation axis; delicate pre-calibration of the scale factor for this axis of the gyroscope would significantly improve system performance. For our implementation, we only needed to carry out the pre-calibration of the scale factor within a small angular rate range and a specific temperature range.

References

1. Aref MM, Ghabcheloo R, Mattila J (2014). A macro-micro controller for pallet picking by an articulated-frame-steering hydraulic mobile machine. In: 2014 IEEE International Conference on Robotics and Automation (ICRA). IEEE Press, New York, pp. 6816–6822. doi: 10.1109/ICRA.2014.6907865
2. Sola J (2017) Quaternion kinematics for the error-state Kalman filter. arXiv preprint arXiv:1711.02508.
3. Noureldin A, Karamat TB, Georgy J (2012) Fundamentals of inertial navigation, satellite-based positioning and their integration. Springer Science+Business Media.
4. Aref MM, Oftadeh R, Ghabcheloo R, Mattila J (2015) Fault tolerant control architecture design for mobile manipulation in scientific facilities. International Journal of Advanced Robotic Systems 12(1):4.
5. Shin E-H (2001) Accuracy improvement of low cost INS/GPS for land applications. University of Calgary.
6. Dissanayake G et al. (2001) The aiding of a low-cost strapdown inertial measurement unit using vehicle model constraints for land vehicle applications. IEEE transactions on robotics and automation 17.5: 731–747.
7. Wu Y. (2014) Versatile land navigation using inertial sensors and odometry: Self-calibration, in-motion alignment and positioning. In: 2014 DGON Inertial Sensors and Systems (ISS). New York, IEEE Press.
8. Wu Y, Zhang H, Wu M, Hu X, Hu D (2012) Observability of strapdown INS alignment: A global perspective. IEEE Transactions on Aerospace and Electronic Systems 48(1): 78–102.
9. Brossard M, Silvere B (2019). Learning wheel odometry and IMU errors for localization. In: International Conference on Robotics and Automation (ICRA), May 2019, Montreal, Canada.
10. Brossard M, Barrau A, Bonnabel S (2019) RINS-W: Robust inertial navigation system on wheels. arXiv preprint arXiv:1903.02210.
11. Brossard M, Barrau A, Bonnabel S (2019) AI-IMU dead-reckoning. arXiv preprint arXiv:1904.06064.
12. Liikanen H, Aref MM, Oftadeh R, Matilla J (2019) Path-following controller for 4WDs hydraulic heavy-duty field robots with nonlinear internal dynamics. In: 10th IFAC Symposium on Intelligent Autonomous vehicles (IAV), Gdansk, Poland, July 2019. Accepted for publication.
13. Analog Devices, ADIS16485 datasheet, rev. H. https://www.analog.com/media/en/technical-documentation/data-sheets/ADIS16485.pdf
14. Liu CZ, Wang X, Tang QJ (2014, November). Error analysis and compensation research of scale factor for MEMS gyroscope. In: International Symposium on Optoelectronic Technology and Application 2014: Image Processing and Pattern Recognition, vol 9301, p. 93010R. International Society for Optics and Photonics.